

Washington University in St. Louis

Washington University Open Scholarship

All Theses and Dissertations (ETDs)

January 2009

Solar Wind Helium, Neon, And Argon In Genesis Aluminum Collectors

Jennifer Mabry

Washington University in St. Louis

Follow this and additional works at: <https://openscholarship.wustl.edu/etd>

Recommended Citation

Mabry, Jennifer, "Solar Wind Helium, Neon, And Argon In Genesis Aluminum Collectors" (2009). *All Theses and Dissertations (ETDs)*. 217.

<https://openscholarship.wustl.edu/etd/217>

This Dissertation is brought to you for free and open access by Washington University Open Scholarship. It has been accepted for inclusion in All Theses and Dissertations (ETDs) by an authorized administrator of Washington University Open Scholarship. For more information, please contact digital@wumail.wustl.edu.

WASHINGTON UNIVERSITY IN ST. LOUIS

Department of Physics

Dissertation Examination Committee:

Charles Hohenberg, Chair

Alexander Meshik

Thomas Bernatowicz

Martin Israel

Frank Podosek

Douglas Wiens

SOLAR WIND HELIUM, NEON, AND ARGON IN GENESIS ALUMINUM
COLLECTORS

by

Jennifer Christine Mabry

A dissertation presented to the
Graduate School of Arts and Sciences
of Washington University in
partial fulfillment of the
requirements for the degree
of Doctor of Philosophy

December 2009

Saint Louis, Missouri

Abstract

The Sun contains over 99% of the mass of the solar system and so, to fully develop a model of how the solar system formed and evolved what the starting composition was and how it evolved, it is crucial to know the isotopic composition of the sun. The Genesis mission collected samples of solar wind (SW) for 853 days and returned them to Earth for analysis. Making these measurements on earth-based instruments is currently the only way to get sufficient precision to differentiate between different solar system components, and SW is the only source of solar material available for sampling. However, there are several processes that have the potential to significantly alter the composition between the time when SW ions are accelerated away from the sun, to the time the laboratory measurements are made. This work attempts to constrain these sources of fractionation and present the best estimate of the isotopic composition of SW helium, neon, and argon implanted into two different aluminum SW collectors on board the Genesis Mission, Al on sapphire and polished Al.

First, during the collection phase of the Genesis mission, diffusion can alter the initial implantation profiles of the SW ions in the collector targets and cause losses of shallowly implanted species. These losses preferentially affect the lighter isotopes, which in turn means the measured ratios of the remaining reservoir will be heavier, both isotopically and elementally. I have conducted a diffusion experiment on a similar time scale as the Genesis mission to determine the diffusion parameters of the two different aluminum collector materials and to quantify the changes in the measured ratios due to

diffusive losses for the light noble gases. The results of this experiment show that the polished Al collector is not sufficiently retentive of the light noble gases to be a reliable collector for the light gases, but that the composition of the light gases implanted in the Al on sapphire collector does not show a measurable effect due to thermal diffusion.

Isotopic fractionation can also occur even before implantation of the SW ions, if the processes which accelerate the SW away from the sun are mass-dependent. In an effort to quantify this effect, the Genesis mission collected separate samples of different types ('regimes') of SW: low-speed, high-speed, and coronal mass ejections, in addition to collecting bulk SW. Compositional differences between the different SW regimes (especially the low-speed and high-speed SW) are thought to provide a measure of this fractionation. By making high-precision isotopic measurements on collectors of the three SW regimes, we have put strict upper limits on the difference between the low-speed and high-speed SW regimes: $^{20}\text{Ne}/^{22}\text{Ne} < 0.24 \pm 0.37\%$ and $^{36}\text{Ar}/^{38}\text{Ar} < 0.11 \pm 0.26\%$. Both of these differences are less than 1σ statistical errors. Helium isotopes are much more susceptible to modification which prevents us from putting a strict upper limit as for Ne and Ar.

And finally we have made isotopic measurements of the light noble gases of the bulk SW (without selective collection of different SW regimes) from the aluminum collectors. Accounting for the sources of fractionation discussed above, I propose the following as the best current bulk SW isotopic values: $^{20}\text{Ne}/^{22}\text{Ne} = 13.75 \pm 0.02$, $^{21}\text{Ne}/^{22}\text{Ne} = 0.0329 \pm 0.0002$, and $^{36}\text{Ar}/^{38}\text{Ar} = 5.501 \pm 0.005$ (all errors are 1σ).

Acknowledgements

I am indebted to the support of many people who helped me through my graduate career. First, I would like to thank my advisor Dr. Charles Hohenberg for giving me the chance to play in the fantastic lab that he built and for never hesitating to share his expertise. And to Dr. Alexander Meshik for sharing all his knowledge and boundless enthusiasm experiment. And I'd like to thank Dr. Olga Pravdivtseva for all her help and support and ready supply of green apples.

Thanks to the Genesis Sample Curation Team at JSC for all their amazing work saving the samples after the unfortunate "hard landing," without which none of this work would have been possible.

Thanks very much to Maitrayee Bose for all of her help especially in the final days.

Thanks to all the 4th floor denizens for being good friends and colleagues and for putting up with my little dog.

Thanks to Tony Biondo and Todd Hardt and all the shop guys.

And thanks especially to my whole family for all their love and encouragement.

Contents

Abstract.....	ii
Acknowledgements.....	iv
Contents.....	v
List of Figures.....	vii
List of Tables.....	xi
Glossary and Abbreviations.....	xiii
Chapter 1 Introduction and Background.....	1
§ 1.1 Introduction.....	1
§ 1.2 Solar Wind.....	5
§ 1.2.1 Basics of the solar wind.....	5
§ 1.2.2 History of SW noble gas measurements.....	10
§ 1.3 The Genesis Mission.....	13
§ 1.4 Genesis Aluminum Samples.....	16
§ 1.4.1 Aluminum on Sapphire.....	17
§ 1.4.2 Polished Aluminum Collector.....	18
Chapter 2 Diffusion Experiment.....	21
§ 2.1 Implantation and Diffusion Theory.....	22
§ 2.1.1 Implantation.....	22
§ 2.1.2 Diffusion.....	24
§ 2.2 Motivation.....	28
§ 2.3 Methods: Diffusion Experiment.....	33
§ 2.3.1 Real-Time Diffusion Bake.....	33
§ 2.3.2 Noble Gas Measurements.....	39
§ 2.4 Data and Analysis.....	56
§ 2.4.1 Release Profiles.....	56
§ 2.4.2 Elemental ratios and amounts.....	63
§ 2.4.3 Isotopic Ratios.....	68

§ 2.4.4 Diffusion properties of Genesis Al collectors	72
Chapter 3 : Solar Wind Regimes	83
§ 3.1 Collection of Bulk and Solar Wind Regimes.....	83
§ 3.1.1 Solar Wind Collection.....	83
§ 3.1.2 Collector Material.....	87
§ 3.2 Methods: Regime Measurements.....	88
§ 3.2.1 Gas Extraction	88
§ 3.2.2 Mass Spectrometry	90
§ 3.2.3 Blanks.....	91
§ 3.2.4 Calibrations and Standards.....	92
§ 3.2.5 Interferences	93
§ 3.3 Data.....	94
§ 3.4 Data Analysis	97
§ 3.4.1 Isotopic Regime Fractionation	97
§ 3.4.2 Elemental Regime Fractionation	101
§ 3.4.3 Precise Bulk SW Isotopic Ratios.....	102
Chapter 4 Summary of results	108
References.....	110
Appendix A: Data Tables	119
Appendix B: Step-wise heating diffusion coefficients	141
Appendix C: Mathematica Files for Diffusion Calculations	147
Appendix D: LabVIEW Laser Rastering Program.....	148

List of Figures

Figure 1.1: A coronal hole seen with the SOHO, EIT instrument on January 8, 2002 (image courtesy of NASA).	7
Figure 1.2: This image was compiled from data taken by Ulysses during two separate polar orbits of the Sun, at nearly opposite times in the solar cycle showing the distribution of SW speeds at different solar latitudes. On the left (near solar minimum) the H-SW completely dominates the higher latitudes with mixing of L- and H-SW near the equator and on the right (near solar maximum) there is a mixing of the L- and H-SW throughout. Image courtesy of Southwest Research Institute and the Ulysses/SWOOPS team.	8
Figure 1.3: Three views of a spectacular coronal mass ejection on January 4 2002. From left to right: Extreme-UV Imaging Telescope (EIT), Large Angle and Spectrometric Coronagraph (LASCO) C2, and LASCO C3. Image courtesy of SOHO/ESA/NASA.	10
Figure 1.4: Apollo 11 Astronaut Edwin E. Aldrin deploying the SWC experiment in Mare Tranquillitatis on July 21, 1969. Photograph by Commander Neil A. Armstrong (NASA Photo S11-40-5872).	11
Figure 1.5: The trajectory of the Genesis spacecraft . The spacecraft orbited around the L1 point for about 2 ½ years before returning to earth (Burnett et al. 2003).	14
Figure 1.6: This AloS piece (~13 mm ²) is a recovered fragment of the original hexagonal collector (~65 mm ²) which was part of the Genesis collector arrays.	17
Figure 1.7: PAC recovered after the ‘hard landing’	18
Figure 1.8: Subdivision of the PAC.	20
Figure 2.1: Depth profiles of ³ He and ⁴ He into 3000-Å Al-film as calculated by TRIM.	23
Figure 2.2: The expected relative change in ³ He/ ⁴ He with depth (99.99% confidence fit to calculated points).	24
Figure 2.3: ²⁰ Ne temperature release profiles from PAC and AloS (Meshik et al. 2006).	30

Figure 2.4: $^3\text{He}/^4\text{He}$ (a) and $^{20}\text{Ne}/^{22}\text{Ne}$ (b) step-wise release profiles from PAC for two different gas release techniques: step-wise heating (orange) and stepped UV-laser (purple) (Mabry et al. 2008). Ratios are normalized to the average value of the all steps in order to compare the profile shape with the calculated TRIM profile. The accuracy of the comparison depends on complete recovery of all implanted gas from the sample. 31

Figure 2.5: Images of AloS and PAC pieces used in diffusion experiment. AloS images were taken at Johnson Space Center. PAC images were taken at Washington University..... 34

Figure 2.6: Vacuum manifold where the AloS and PAC samples were baked. Each finger contained pieces of each target and an oven was slid over the finger and then thermally insulated..... 38

Figure 2.7: Noble gas extraction and cleaning system. 44

Figure 2.8: Neon 3-isotope plot showing bulk isotopic ratios from the five unbaked samples, along with the direction to the terrestrial atmospheric value. There is no apparent mixing between the SW values and the terrestrial atmosphere..... 47

Figure 2.9: Pressure versus the nominal sensitivity (S_n) normalized to the sensitivity measured at 10^{-5} torr (S_0). It is nonlinear at pressures greater than $\sim 10^{-7}$ torr (Hohenberg 1980). 53

Figure 2.10: The $^3\text{H}/^4\text{He}$ ratio versus amount of ^4He for P8b which was melted in one temperature step, and then repeatedly re-measured after removing some of the gas. The blue triangles are uncorrected measurements which vary widely because of high pressure effects. The purple circles are the data corrected using Equation 2.7. 55

Figure 2.11: Release profile showing the percentage of ^{20}Ne released versus the step-wise heating temperature. This plot compares the release profiles ^{20}Ne from AloS and PAC measured using artificially implanted samples (Meshik et al. 2000) and those measured for this work (A70, PSE). 57

Figure 2.12: Temperature release profiles for ^4He (a), ^{20}Ne (b), and ^{36}Ar (c) for AloS and PAC. The x-axis temperature refers to the step-wise heating temperature and the y-axis shows the cumulative release of the gas in %. The temperature referred to in the legend is the long-term bake temperature of that sample. 59

Figure 2.13: Step-wise release plots, temperatures on the lines refer to step-wise temperature of the largest release step. 61

Figure 2.14: $^4\text{He}/^{20}\text{Ne}$ (a) and $^{20}\text{Ne}/^{36}\text{Ar}$ (b) elemental ratios, all are normalized to the unbaked reference sample A70. Sample A63 was also unbaked but badly scratched compared to A70. Linear fits with 95% confidence levels are shown for all except for the PAC $^4\text{He}/^{20}\text{Ne}$ ratio which does not appear to be linear. Errors are 2σ statistical. ... 64

Figure 2.15: ^4He (a), ^{20}Ne (b), and ^{36}Ar (c) amounts normalized to A70. Linear fits with 95% confidence levels are shown for all except for the PAC $^3\text{He}/^4\text{He}$ ratio which does not appear to be linear. Errors are 2σ statistical. 67

Figure 2.16: Isotopic ratios $^3\text{He}/^4\text{He}$ (a) $^{20}\text{Ne}/^{22}\text{Ne}$ (b) and $^{36}\text{Ar}/^{38}\text{Ar}$ (c). All are normalized to unbaked AloS A70. Linear fits with 95% confidence levels are shown for all. Errors are 1σ statistical. 71

Figure 2.17: Approximate diffusion coefficients were calculated by assuming a uniform distribution of gas leading to the following Arrhenius plots for ^4He of unbaked samples of each material, a) AloS and b) PAC. The lines were fit to the points corresponding to the major release of SW ^4He from the samples. Light grey points do not belong to the major gas release and were not taken into account in calculation of the activation energy. a) Most of the SW ^4He released from AloS in just three temperature steps which are shown in blue. b) The release of SW ^4He from PAC was spread out over more temperature steps than the AloS. The majority of the gas was released in the steps corresponding to the red points, and there was a second peak in the gas release from PAC shown with the green points. 74

Figure 2.18: Natural log of the TRIM calculated implantation depth profile of ^4He (black points) with a 5th order polynomial fit (pink line). 77

Figure 2.19: Arrhenius plot for ^3He and ^4He in AloS based on the fractional loss of gas during the long-term bake..... 79

Figure 2.20: The calculated fractional loss of ^4He from AloS for different temperatures versus the number of divisions of the total SW exposure time ('time bins'), see text for explanation. The points are fit by an exponential curve that gives the fractional loss for infinite time bins. 81

Figure 3.1: a) One of the Genesis regime collector arrays. b) The whole collector assembly with the stacked regime collector arrays, additional regime bulk array on the inside of the canister lid, and additional collectors..... 85

Figure 3.2: Number of hours of collection time vs the SW speed (Reisenfeld et al. 2005). 86

Figure 3.3: Sample cell with sapphire viewport. In each chamber there is one piece of AloS (bulk, L, H, or CME), supported by Ta-foil ribs. 89

Figure 3.4: AloS after IR-laser ablation. Each rectangular area represents a separate analysis run of either neon or argon..... 90

Figure 3.5: Mass scan of the peaks at masses 35 to 40 during SW Ar measurements. 92

Figure 3.6: Isotopic ratios $^{20}\text{Ne}/^{22}\text{Ne}$ (a), $^{21}\text{Ne}/^{20}\text{Ne}$ (b), and $^{36}\text{Ar}/^{38}\text{Ar}$ (c) for the bulk SW and each of the three SW regimes. Colored points represent individual measurements and black points are the weighted averages (see explanation in § 3.3). All errors are 1σ statistical. 99

Figure 3.7: $^{20}\text{Ne}/^{36}\text{Ar}$ of the bulk, H, L, and CME SW regimes. The L-SW is about 25% lower than H- SW. This difference is attributed to fractionation in the SW based on the first ionization potential of different elements. 102

Figure 3.8: Neon 3 isotope plot comparing Genesis measurements from multiple labs and collector materials (Grimberg et al. 2006; Meshik et al. 2007; Heber et al. 2009) along with the direction to the terrestrial atmosphere. The points are separated into 3 distinct groups, but not along a SW-terrestrial atmosphere mixing line. All errors are 1σ statistical. 105

Figure 3.9: Comparison of solar argon measurements: Apollo foils, 5.3 ± 0.3 (Cerutti 1974); Apollo foils revised, 5.4 ± 0.15 (Geiss et al. 2004); lunar regolith, 5.48 ± 0.05 (Benkert et al. 1993), 5.58 ± 0.03 (Becker et al. 1998), and 5.80 ± 0.06 (Palma et al. 2002); SOHO, 5.50 ± 0.6 (Weygand et al. 2001) and terrestrial air, 5.319 ± 0.008 (Ozima & Podosek 2001). In this work we are reporting a precise value of 5.501 ± 0.005 107

List of Tables

Table 1.1: Physical and thermal properties of pure Al and the 6061-T6 Al alloy (Aluminum Association 2000).....	19
Table 2.1: Diffusion equation solution in fractional loss form for a uniform distribution C_0 and planar geometry of thickness l (Jain 1958; McDougall and Harrison 1999).	27
Table 2.2: Approximate solutions for the diffusion coefficient of the i^{th} step-wise heating step (D_i), for a uniform distribution C_0 and planar geometry of thickness l (Fechtig and Kalbitzer 1966; McDougall and Harrison 1999).	28
Table 2.3: Helium and neon measured isotopic ratios from AloS and PAC.	32
Table 2.4: Flown Genesis SW-collectors used in diffusion experiment. The chosen areas are shown in bold.....	36
Table 2.5: Timeline of the long-term diffusion experiment.	39
Table 2.6: Procedure for preparation of He, Ne, and Ar for mass spectrometric analysis for step-wise heating experiments.....	44
Table 2.7: Elemental and helium isotopic ratios for the light nobles gases in the terrestrial atmosphere (Mamyrin et al. 1970; Verniani 1966) and the previously measured SW values from the SWC experiment (Cerutti 1974; Geiss et al. 1972)	48
Table 2.8: Summary of neon and argon interference corrections for the time period June 2008 to November 2008 when Genesis diffusion measurements were being done. 51	
Table 2.9: Helium backscatter correction factors for an aluminum target, calculated using TRIM (Ziegler 2004).....	65
Table 2.10: Elemental fluxes (in atoms) and elemental ratios. He is corrected for backscattering. Errors (in parentheses) are 2σ statistical.....	66
Table 2.11: Bulk isotopic ratios of He, Ne, and Ar in AloS and PAC after prolonged baking. $^3\text{He}/^4\text{He}$ are corrected for backscattering. Errors are 1σ statistical.	69

Table 2.12: Average activation energy (E_a) and frequency factor (D_0) from a linear fit to an Arrhenius plot using the steps corresponding to the major gas release from the sample. Errors were calculated by standard deviation..... 75

Table 2.13: Fractional loss of ^4He from AloS samples (relative to A70)..... 77

Table 2.14: Calculated loss estimates of helium from AloS for the time of the Genesis mission at various temperatures. 82

Table 3.1: Solar wind collection time for each of the SW regime collectors (Reisenfeld et al. 2005)..... 87

Table 3.2: Neon isotopic regime results (Meshik et al. 2007). Backscatter corrections are applied to the averages. ^{20}Ne fluxes are determined with $\pm 9\%$ (1σ)..... 95

Table 3.3: Argon isotopic regime results (Meshik et al. 2007). Note: ^{36}Ar fluxes are determined with $\pm 9\%$ (1σ). This includes statistical error of $\pm 2\%$ and an overestimation of the rastered area due to scratches. 96

Table 3.4: Regime elemental ratios, numbers in parenthesis represent 9% error (Meshik et al. 2007)..... 97

Glossary and Abbreviations

AloS	Aluminum on Sapphire, Genesis SW collector designed for noble gases.
ACE	Advanced Composition Explorer, launched in 1997 and still operating.
BMG	Bulk metallic glass, a Genesis SW collector.
CME	Coronal mass ejection, explosive ejection of material from the solar corona.
Coronal hole	Low density region of the corona where the fast solar originates.
Coulomb drag	Process where heavier species are accelerated by collisions with ionized hydrogen.
DOS	Diamond-like carbon on silicon, a Genesis SW collector.
H-SW	High-speed/ fast solar wind which originates in coronal holes and typically has speeds >500 km/s. Sometime referred to as coronal hole solar wind.
FIP	First ionization potential.
Genesis	NASA mission which returned samples of solar wind for earth-based analysis.
L1	Lagrange point, spacecraft can orbit around the earth-sun L1 point to observe the sun outside of the earth's magnetosphere.
L-SW	Low-speed/ slow solar wind with speeds <500 km/s. Sometimes referred to as interstream solar wind.
PAC	Polished aluminum collector, Genesis SW collector also used as a heat shield for the battery compartment.
Regimes	Term used to designate solar wind originating from different sources and have different properties. Three solar wind

regimes have been identified: slow, fast, and coronal mass ejection.

SEP	Solar energetic particle, in this work used to refer to an isotopically heavy solar wind component misidentified in lunar samples.
SOHO	Solar and Heliospheric Observer, launched in 1995 and still operating.
SRC	Sample return capsule, the canister containing the solar wind collectors for the Genesis mission which was returned to earth.
SW	Solar wind, plasma stream carrying solar material away from the sun.
SWC	Solar Wind Composition experiments, solar wind sample return experiment where foils were exposed to the solar wind during the Apollo mission.

Chapter 1 Introduction and Background

§ 1.1 Introduction

The solar system began to form around 4.6 billion years ago from the rotating disk of gas and dust known as the solar nebula (Boss 2003). The vast majority of this matter was incorporated into the sun which contains 99.86% (Woolfson 2000) of the mass of the solar system. To fully develop a model of how all of the other bodies in the solar system formed and have evolved from the balance of this material, it is crucial to know initial composition of the starting material, now represented in the present composition of the sun. Especially important are the “trace” elements which are less abundant than H and He such as oxygen, nitrogen, and the noble gases, which have multiple isotopes that can provide clues about various early solar system processes (Woolfson 2000). Most solar system formation models assume that the composition of the solar nebula was fairly homogenous and, given the fraction of the solar nebula incorporated into the sun, the present solar composition is assumed to be unchanged, with the obvious exceptions for the products of nuclear reactions. Thus solar composition can be used as the starting composition for all other solar system bodies (Ozima et al. 1998; Bochsler 2000; Wiens et al. 2004). Any deviations from this initial composition, such as in the atmospheres of the terrestrial planets (Pepin 1991, 2006), must be explained by processes occurring during the formation and evolution of the various solar system bodies.

Elemental abundances and some isotopic ratios can be determined from spectroscopic measurements of the photosphere (Hall 1972, 1975; Hall and Engvold

1975), however the precision is limited and the noble gases do not have any useful lines in the photospheric spectra (Anders and Grevesse 1989; Lodders 2003; von Steiger et al. 2001). Therefore other means must be found to obtain the elemental abundances as well as the isotopic composition of the noble gases in the sun.

Presently, the solar wind (SW) is the only available source from which to sample actual solar material. This allows for more precise analysis of the trace elements than spectroscopic measurements. In-situ measurements of SW can be made by instruments aboard spacecrafts such as the Solar and Heliospheric Observatory (SOHO) (Delaboudinière et al. 1995; Domingo et al. 1995; Hovestadt et al. 1995) and the Advanced Composition Explorer (ACE) (Gloeckler et al. 1998; Mason et al. 1998; McComas et al. 1998; Smith et al. 1998). However, with current technology, real time measurements by on-board instruments do not possess the sub-percent precision necessary to differentiate between various planetary components. One way to reach the required precision is to increase sampling time and return the ‘integrated’ SW samples to the earth to measure in the laboratory instead of measuring them in space.

During the Apollo era, numerous samples of SW were returned to earth for analysis in foils which were exposed to the SW for the Solar Wind Composition (SWC) experiments (Geiss et al. 1969, 2004; Signer et al. 1965) and in the form of lunar regolith (Pepin et al. 1970, 1999; Bernatowicz et al. 1979; Benkert et al. 1993; Palma et al. 2002). Light SW noble gases were analyzed in the foils delivered SWC experiment, however, low gas abundance and contamination from lunar dust compromised the results. In contrast, lunar regolith has a much higher abundance of SW, as it has been exposed to

the SW for millions of years, but it has been subject to additional processes, such as galactic cosmic-ray interactions, diffusive losses, and surface erosion, all of which alter the original composition of the implanted SW.

The premise of the Genesis mission was to obtain pure samples of SW which were unaffected by the alteration processes the lunar regolith suffered, but with long enough SW exposure times to avoid the low-abundance issues of the SWC foils. The mission returned samples of SW collected over 2 years at the L1 point for earth-based laboratory measurements, in order to obtain accurate, high precision isotopic measurements of trace elements in the SW (Burnett et al. 2003).

Using measured values of the SW as a proxy for the present solar composition, and hence the initial solar nebula composition, only works as long as there is not any significant fractionation (or that it can be quantified) of the composition of this material from the time it is in the outer convective zone. There are several processes that can alter the laboratory measured composition from the true solar composition, as it is ionized, accelerated away from the sun, and eventually collected and analyzed, and it is necessary to quantify the scale of these effects.

First, isotopic fractionation can occur if the processes accelerating the SW away from the sun are mass-dependent. One such process, inefficient Coulomb drag (Geiss et al 1970; Bodmer and Bochsler 1998), accelerates heavier species by Coulomb collisions with escaping protons. Although the Coulomb drag effect has been modeled to some degree, the levels of fractionation depend upon many factors that cannot be easily

modeled in reality. In an effort to delineate and quantify the Coulomb drag effect, the Genesis Mission collected samples of SW from different flow regimes: low-speed (L), high-speed (H), and coronal mass ejections (CME). Compositional differences between the different SW regimes (especially L- and H-SW) are thought to provide a measure of this fractionation.

Second, there are implantation effects. Since solar wind ions are bound to the solar magnetic field lines spiraling outward from the sun, the SW is a constant velocity stream. And implantation of SW ions at a constant velocity results in mass fractionation with depth (Grimberg et al 2006) since the heavier isotopes have higher energy, and thus a longer range. The effect of this is a varying isotopic composition with depth and, if all of the gas is not recovered during the measurement, the cumulative measured isotopic ratios will differ from their source values. Surface erosion due to SW sputtering of highly radiation-damaged, SW saturated lunar regolith material modifies the measured value, making measured ratios heavier than the SW source. This effect will probably be negligible for Genesis, but effects due to the loss of surface material due to abrasion (perhaps in the “hard” landing) must be evaluated.

And third, diffusion favors the lighter, more mobile, isotopes (and elements) and can clearly modify the measured composition compared with that originally implanted. Incomplete degassing of lunar regolith and Genesis samples will thus make the measured ratios lighter than the total reservoir contained in the material, and prior diffusive losses will make the retained noble gases heavier than those implanted. Diffusion is, therefore,

a process that must be carefully considered. Near-surface regions are more affected by diffusive losses, regions already favoring the lighter isotopes by constant-velocity implantation, so the effects of diffusive losses can be enhanced by implantation effects. The main purpose of this work is to quantify these effects in order to obtain the most accurate and precise isotopic measurements possible of the SW light noble gases using samples of SW collected and returned to earth by the Genesis mission.

§ 1.2 Solar Wind

§ 1.2.1 Basics of the solar wind

The modern concept of SW began in the mid 19th century when an amateur astronomer, Richard C. Carrington, witnessed a solar flare and connected it to geomagnetic disturbances on earth. But it was not until many decades later, in the 1950s, synthesizing the work of previous solar scientists, that Eugene Parker (1958, 1960) proposed the first modern scientific theory of the solar wind as a supersonic flow of particles out of the solar atmosphere. Finally, in January 1959, the first ever direct observations and measurements of strength of the solar wind were made by the Soviet satellite Luna 1 using on-board hemispherical ion traps. This discovery, made by Konstantin Gringauz was verified by Luna 2 and Luna 3. Three years later it was confirmed by M. Neugebauer and C. W. Snyder (1962) using the Mariner 2 spacecraft.

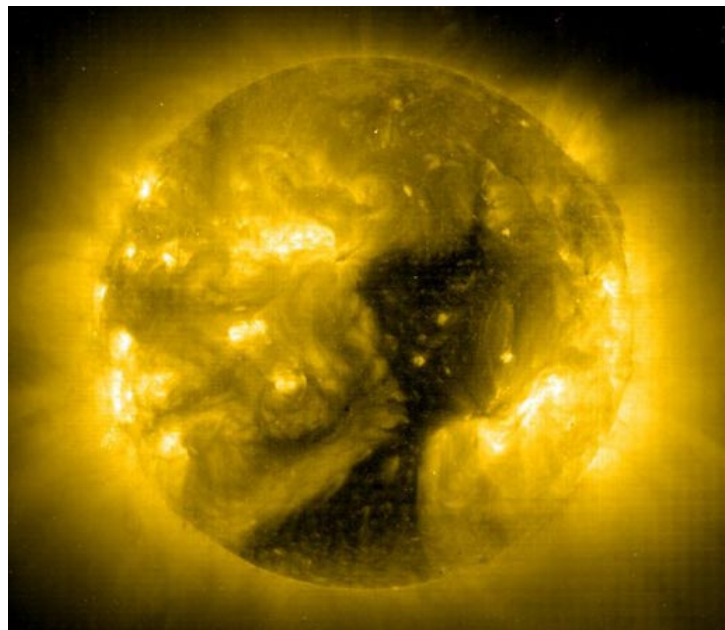
In basic terms, the solar wind is a plasma of mostly protons and electrons streaming out from the sun's corona. Roughly 10^9 kg/s flow out from the sun as SW, a minute amount compared to the mass of the sun, representing only about $10^{-4} M_{\odot}$ over the

present age of the sun. In fact, this is less even than the amount of mass loss due to blackbody radiation, and has only a very slight impact on the total energy and momentum flux of the sun, although it does contribute significantly to the angular momentum loss of the sun (Axford 1985). The rough elemental composition of the SW is 95% hydrogen, 4% helium, and 1% other elements, the most abundant of which are: oxygen, carbon, iron, magnesium, silicon, neon, and nitrogen (Meyer-Vernet 2007).

The processes at work accelerating the SW are still not fully understood. It is known that the SW originates in the corona, the outer atmosphere of the sun just above the chromosphere. Neutral atoms in the photosphere are then ionized in the chromosphere by UV-radiation from the corona above it (Geiss & Bochsler 1985; von Steiger & Geiss 1989; Marsch et al. 1995). With increasing altitude, the chromosphere and corona decrease in density, but dramatically increase in temperature. The temperature of the corona is around 10^6 K, three orders of magnitude hotter than the photosphere. The exact mechanisms for providing the energy for such a dramatic temperature increase is still a mystery, but probably comes from some combination of either small reconnections of magnetic flux tubes which may produce nanoflares capable of briefly heating up the local plasma to 10^6 K (Cargill and Klimchuk 2004; Parker 1987) or Alfvén waves which are magneto-hydrodynamic waves that travel outward through the plasma along magnetic field lines (Moore et al. 1991; Tomczyk and McIntosh 2009). At this temperature, protons and electrons in the corona have enough thermal energy to escape the sun's gravity, but additional acceleration mechanisms are needed to understand the incorporation of heavier ions into the SW.

Adding additional complexity, three different types of SW have been identified: L-SW, H-SW, and CME. Following the terminology accepted by the Genesis Mission Science team I will refer to these different types of solar wind as ‘SW regimes’ throughout the rest of this paper. Each SW regime originates from different regions of the corona (McComas et al. 1998; Neugebauer 1991) and each may have different acceleration mechanisms.

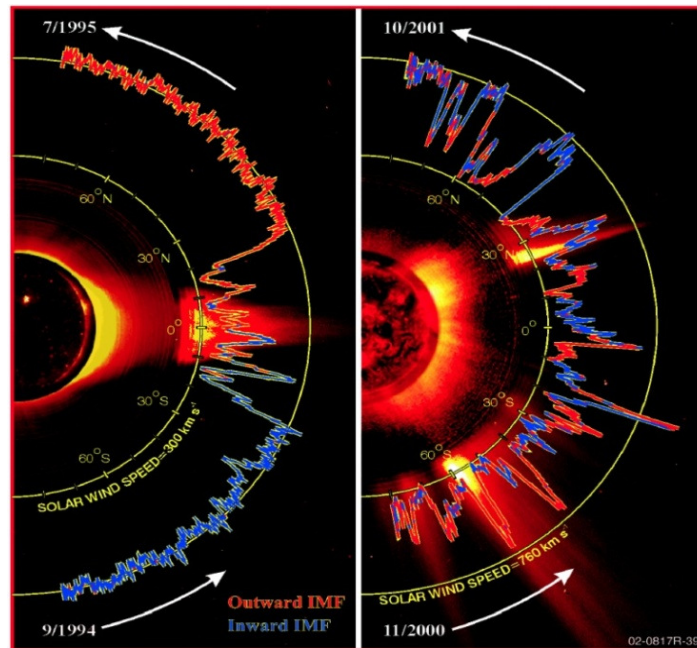
Figure 1.1 A coronal hole seen with the SOHO, EIT instrument on January 8, 2002 (image courtesy of NASA).



The corona has a complex structure, mostly due to the fluctuating magnetic fields of the sun. There are less dense regions that appear darker (Figure 1.1), known as coronal holes, and brighter more complexly structured regions. The distribution of these regions varies with the solar cycle (Figure 1.2), with large coronal holes dominating the higher latitudes and an equatorial streamer belt during minimums of the solar cycle and with

smaller more homogeneously distributed coronal holes and streamers during the maximum of the solar cycle (McComas 1998).

Figure 1.2: This image was compiled from data taken by Ulysses during two separate polar orbits of the Sun, at nearly opposite times in the solar cycle showing the distribution of SW speeds at different solar latitudes. On the left (near solar minimum) the H-SW completely dominates the higher latitudes with mixing of L- and H-SW near the equator and on the right (near solar maximum) there is a mixing of the L- and H-SW throughout. Image courtesy of Southwest Research Institute and the Ulysses/SWOOPS team.

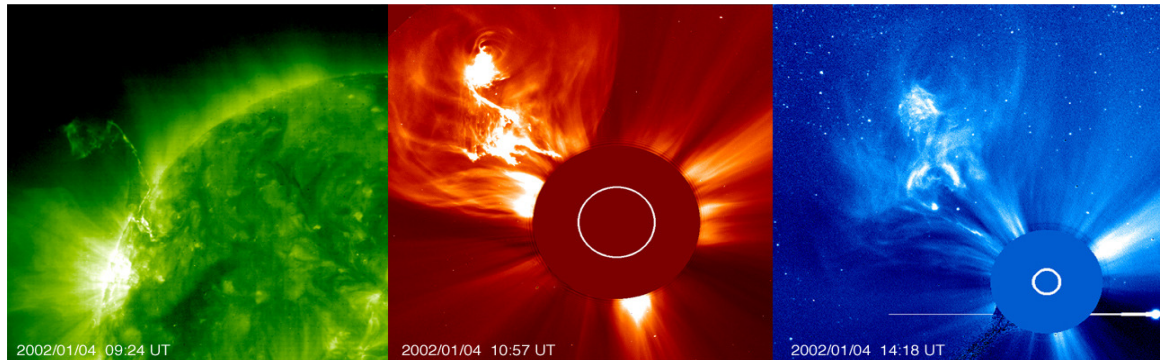


The H-SW (500 - 800 km/s) originates in coronal holes, and flows out along open magnetic field lines (Neugebauer et al. 2003). The source of the L-SW (300 km/s – 500 km/s) is associated with coronal streamers (Neugebauer et al. 2003; Zurbuchen et al. 2002), which have closed magnetic loops and are often associated with more active regions (Fisk et al. 1998; von Steiger 1998). There are two possible mechanisms for

accelerating the heavier ions in the L- and H-SW: Coulomb drag (Geiss et al. 1970) or wave-particle interactions (Cranmer et al. 1999). Coulomb drag has received the most attention and evidence points to this mechanism as the most likely for the L-SW (Bodmer and Bochsler 1998; Aellig et al. 2001), however wave-particle interactions have not been ruled out for the H-SW. Coulomb drag is a mass and charge-state dependent process which accelerates particles by Coulomb collisions with protons. The efficiency of this process depends on the proton flux; high proton fluxes more efficiently accelerate heavier species than low proton fluxes. The L-SW often has a lower proton flux which can lead to depletions in heavier isotopes (of the same charge-state) relative to the H-SW. This is most obviously seen in a lower He/H ratio in the L-SW than the H-SW (Borrini et al. 1981; Bodmer & Bochsler 1998).

There is one additional SW component, this one due to coronal mass ejections. These are explosive events thought to result from the large-scale restructuring of magnetic field structures (McComas et al. 1998; Hudson et al. 2006). These events eject tons of extra mass (around 10^{12} kg per event) out into space. The SW accelerated by these events has highly variable speeds and compositions, and it seem to be marked by the existence of bidirectional suprathermal ions and electrons (Neugebauer et al. 2003). CMEs occur more frequently during the maximum of the solar cycle, but can occur at any time (Neugebauer et al. 2003).

Figure 1.3: Three views of a spectacular coronal mass ejection on January 4 2002. From left to right: Extreme-UV Imaging Telescope (EIT), Large Angle and Spectrometric Coronagraph (LASCO) C2, and LASCO C3. Image courtesy of SOHO/ESA/NASA.

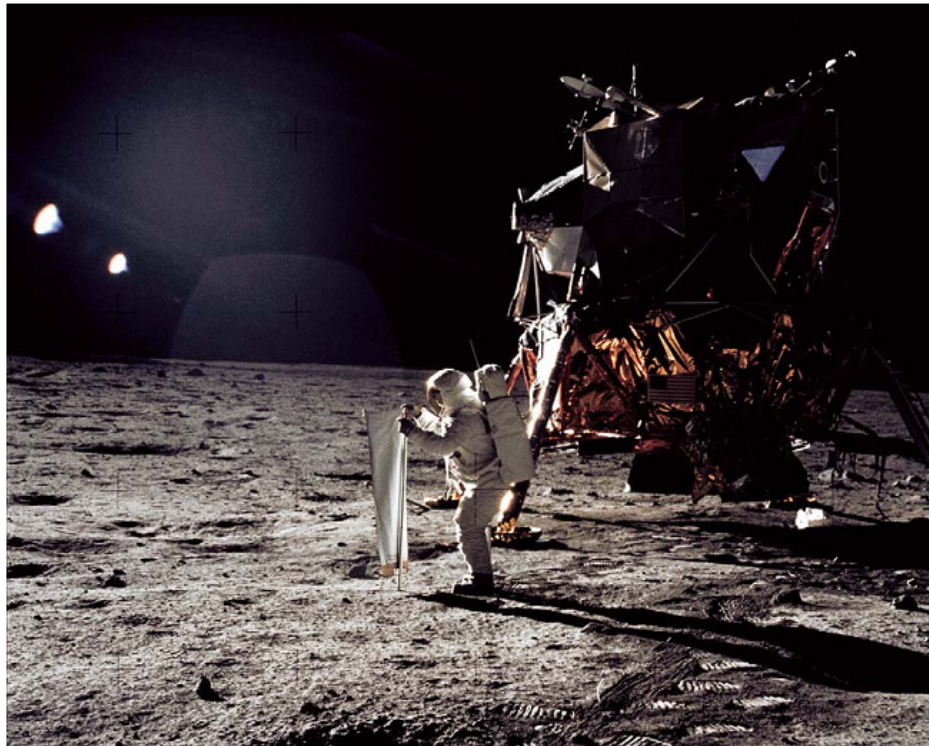


§ 1.2.2 History of SW noble gas measurements

There have been previous lab-based analysis of the SW. The Apollo Solar Wind Composition (SWC) experiments, carried by Apollo Missions 11, 12, 14, 15 and 16, exposed aluminum and platinum foils to the SW for up to two days while astronauts were on the moon (Figure 1.4). From these foils, light noble gas elemental and isotopic measurements were made, but the SW flux of heavier elements was too low, and the material not pure enough to measure heavier elements in the SW. Solar wind was collected from five different Apollo landing sites, and the foils were exposed for time periods ranging from 77 minutes in July 1969 (Apollo 11) to 45 hours in April 1972 (Apollo 16). The foils were fixed to a telescopic pole which was planted in the lunar soil, then, after SW exposure, they were removed from the pole, rolled up, and placed in a Teflon bag for storage during return to earth (Geiss et al. 1969; Signer et al. 1965). However, contamination with lunar dust (exposed for ~50 million years and subject to

many fractionation effects) rendered the SWC foils inaccurate for Ar, unusable for the heavier noble gases, and too impure for other elements.

Figure 1.4: Apollo 11 Astronaut Edwin E. Aldrin deploying the SWC experiment in Mare Tranquillitatis on July 21, 1969. Photograph by Commander Neil A. Armstrong (NASA Photo S11-40-5872).



Geiss et al (2004) summarized the results from the SWC experiments in anticipation of the Genesis mission. SW speeds measured at the exposure times of the SWC experiments indicate that only the slow SW was likely present at the time of collection of all five foils. Although some good SW light noble gas measurements were made using the Apollo SWC foils, the short exposure times (and therefore low concentration of SW-gas collected), and the presence of soil contamination, meant it was difficult to get the

required precision for planetary science purposes, and it could not address the different solar regimes.

Lunar regolith (soil) was also brought back from the moon during the Apollo missions, another source with which to derive SW isotopic and elemental compositions as they have been exposed to it for millions of years. This long SW exposure time eliminates the problem of limited abundance with the SWC foils, but there are many complicating factors that degrade the SW compositions derived from lunar regolithic material. Corrections must be made for isotopes produced by galactic (and solar) cosmic ray nuclear reactions that make extracting a precise SW composition difficult. The solar wind was implanted in the outermost few microns while the galactic cosmic-ray effects extend meters from the surface, peaking at about 20 g/cm^2 , an effect clearly apparent as specific significant variations with depth in lunar rocks. Lunar regolith was exposed for longer times at the very surface than rocks, enhancing the solar component, but these suffer from serious diffusive losses and surface erosion effects.

Early mass spectrometric measurements of trapped noble gases in samples of lunar regolith (Hohenberg et al. 1970; Pepin et al. 1970) demonstrated the depth dependent variation in isotopic composition of helium, neon, and argon and speculated that it was related to the deeper implantation depth of the heavier isotopes produced by constant-velocity SW (Hohenberg et al. 1970). However, later measurements (Benkert et al. 1993; Palma et al. 2002) led others to begin attributing the heavier isotopic composition to a

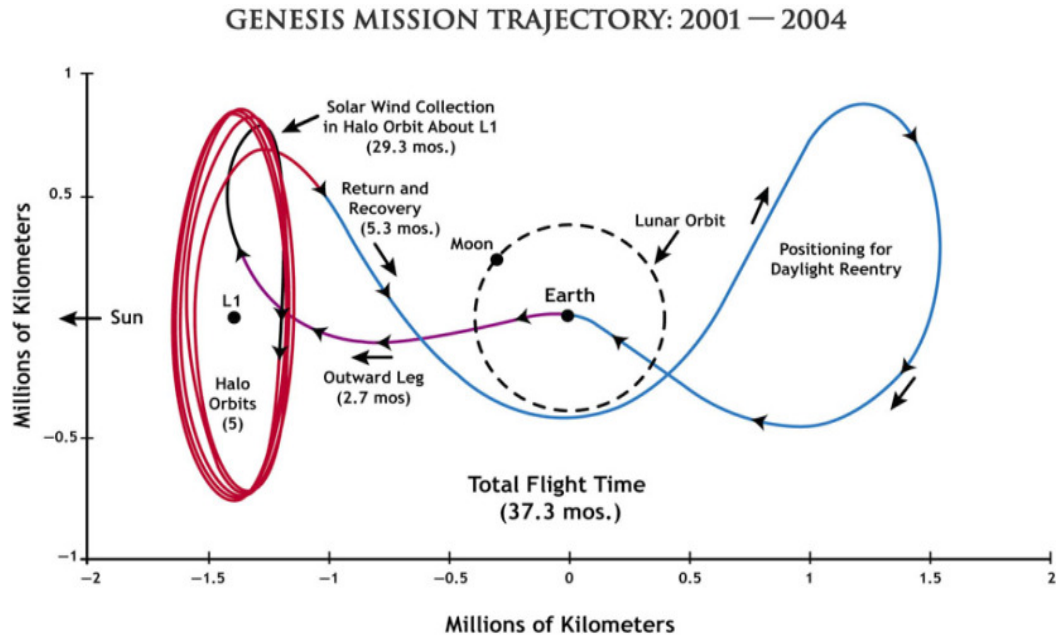
new solar wind component called “SEP” for “solar energetic particle”, thought to be the “high energy tail” of the SW.

With the new Genesis results, this “component” is confirmed to be actually an artifact (as originally thought) produced by a combination of constant-velocity SW implantation and diffusive losses from the regolith, enhanced by SW saturation effects, surface sputtering itself enhanced by amorphization due to surface loading (some regolith samples have He concentrations of 1 g/cm^3 , with H implanted at 20 times that). This old suggestion was recently revisited by Grimberg et al (2006). The confusion introduced by different processes at work in the lunar regolith made it difficult to pin down the real SW composition, and the “explanation” due to the introduction of multiple components reminds us of the complications introduced by the Pre-Copernican models of planetary motion. Clarity was brought to the SW for the first time by the Genesis Mission.

§ 1.3 The Genesis Mission

The Genesis Mission is the fifth in NASA’s budget class Discovery Mission series. It was conceived primarily as a planetary science mission to determine the precise composition of the SW (and by extension the sun). The Genesis spacecraft was launched on August 8th 2001, flew to the L1 Earth-Sun Lagrange point, and orbited around it for 868 days collecting SW (Figure 1.5). Genesis SW-collectors made from carefully chosen ultra-pure materials such as Si, Al, and Au, passively captured SW ions by exposing the collectors to the SW streaming out from the atmosphere of the sun, allowing the ions to be implanted in the collector materials which were returned to earth for analysis.

Figure 1.5: The trajectory of the Genesis spacecraft . The spacecraft orbited around the L1 point for about 2 ½ years before returning to earth (Burnett et al. 2003).



The major science objectives of the Genesis mission were stated by Burnett et al (2003):

- “(1) to obtain solar isotopic abundances to the level of precision required for the interpretation of planetary science data,
- (2) to significantly improve knowledge of solar elemental abundances,
- (3) to measure the composition of the different solar wind regimes,
- (4) and to provide a reservoir of solar matter to serve the needs of planetary science in the 21st century.”

More specifically, the highest priority goals were to measure oxygen and nitrogen isotopes as well as noble gas isotopes and elements (Burnett et al. 2003). The analysis

requirements of the mission were to measure elemental abundances with a precision of 10% and isotopic ratios with a precision of 1% or better at the 2σ level.

In addition to precise measurements of the bulk composition of the SW, the Genesis mission collected separate samples of the three different types of SW (L, H, and CME). Geiss (1970), Bochsler (2000), and Bodmer and Bochsler (2000) suggested that compositional differences between the different SW regimes, especially between H- and L-SW, can provide a measure of the fractionation between solar and SW compositions. Therefore, in addition to the bulk collector arrays which were continuously exposed to the SW, there were three separate arrays which were selectively exposed to the SW only when on-board monitors determined that specific SW regime was present (Burnett et al. 2003; Barraclough et al. 2003).

After the end of SW collection in April 2004, the Genesis spacecraft headed back to Earth, and the low potential well of the L1 point meant that very little impulse was needed for the return trip. On 8 September 2004, the spacecraft reentered the Earth's atmosphere and then the sample return capsule (SRC) detached and dropped down to Earth. Unfortunately, the capsule parachute failed to deploy, and the SRC slammed into the desert ground at the Utah Test and Training Range at nearly 200 miles per hour, shattering the collectors, exposing them to the possibility of severe terrestrial contamination by the local Utah soil (Stansbery et al. 2005).

More than 10,000 fragments of the array collectors were painstakingly picked out of the Utah soil (Allton et al. 2006), carefully documented, separated and packaged in a

Class 10,000 clean room at the Utah Test and Training Range for transportation to the NASA Johnson Space Center (JSC) curation facility (Stansbery et al. 2005). The sample curation team then went to work identifying and cataloguing the fragments. The problem of identifying fragments from the different regime arrays was solved through some clever forethought: the thickness of the collectors was different for each array: 700 μm for bulk arrays, 650 μm for the CME array, 600 μm for the H-SW array, and 550 μm for the L-SW array (Allton et al. 2006).

§ 1.4 Genesis Aluminum Samples

Prior to the launch of the Genesis Mission, a great deal of time was spent researching and designing a variety of specialty materials and coatings to use for the collectors in order to achieve a wide range of analytical goals. The criteria used in selecting materials were: purity, analyzability, surface and interface cleanliness, physical durability, solar-thermal properties, and elemental diffusion in sample (Jurewicz et al. 2003). The majority of the collectors were made of thin films evaporated onto different substrates, hexagonally shaped collectors which were 10.2 cm across and fitted together into a total of five collector arrays (Allton et al. 2005). Additionally, there were a few special collectors that were not part of the main collector arrays, one of which I will discuss more below: polished aluminum.

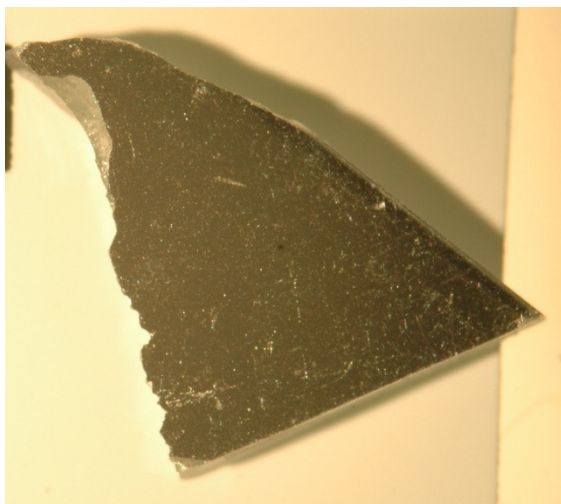
For the SW measurements made at Washington University I used two different aluminum collectors: aluminum on sapphire (AloS) and the polished aluminum collector

(PAC), so I will discuss these two in more detail below. See Jurewicz et al (2003) for an excellent description of all of the Genesis collectors.

§ 1.4.1 Aluminum on Sapphire

The AloS collector (Figure 1.6) is made of 3000 Å of very high purity aluminum vapor deposited onto a sapphire substrate, and was designed especially for laser extraction of noble gases. There were 26.5 hexagonal AloS collectors, constituting about 10% of the total collector array surface (Allton et al. 2005). The sapphire substrate is a commercially prepared single-crystal Al₂O₃ made by the ceramics and semiconductor company Kyocera. The 3000-Å aluminum film was deposited using strict cleanliness procedures in the JPL Microdevices Laboratory (Jurewicz et al. 2003). Preflight tests by Meshik et al. (2000) at Washington University indicated that the material was pure enough for neon and argon analysis.

Figure 1.6: This AloS piece (~13 mm²) is a recovered fragment of the original hexagonal collector (~65 mm²) which was part of the Genesis collector arrays.



§ 1.4.2 Polished Aluminum Collector

The other material we are using for this study, PAC, is made from a highly polished aluminum alloy (Figure 1.7). The primary purpose of this material was to act as a radiator to reduce the temperature of the interior of the SRC and keep it from overheating. Although the careful selection criteria and rigorous pre-flight testing that AloS was subjected to were not applied to this material (Jurewicz et al. 2003), it was always considered a possible ‘collector opportunity’, and because of the crash, it seemed worthwhile to explore the usefulness of this material since the PAC was less damaged (only bent, whereas the AloS and other collectors were shattered), and some of the largest pieces (~45 cm²) recovered after the crash were pieces of PAC (Allton et al. 2005).

Figure 1.7: PAC recovered after the ‘hard landing’.



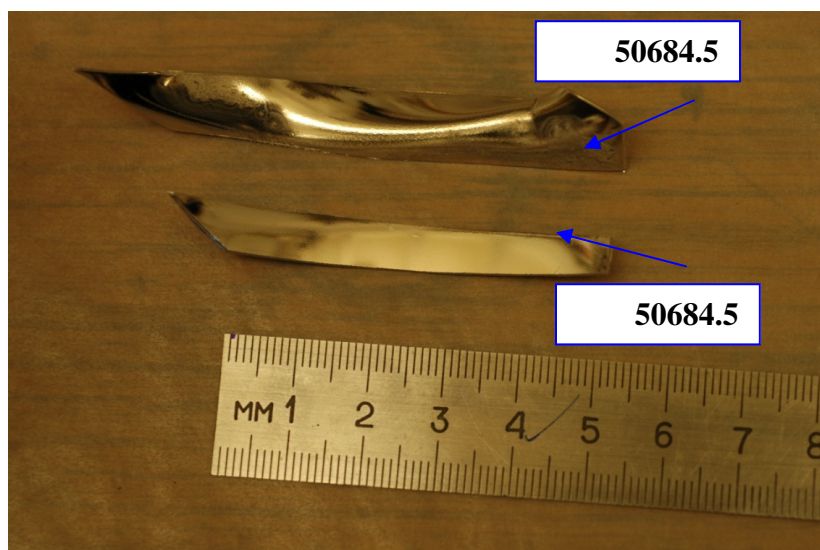
The PAC was made from a standard commercial aluminum alloy #6061-T6, milled to 0.025-inches-thick, and then hand polished at JSC (Allton et al. 2005). The major trace components of the 6061 alloy are Mg, Si, and Fe (Aluminum Association 2000). These change the physical and thermal properties relative to pure Al, which are compared in Table 1.1. Of particular importance for this work, the 6061 alloy has a lower melting temperature than pure Al.

Table 1.1: Physical and thermal properties of pure Al and the 6061-T6 Al alloy (Aluminum Association 2000).

Property	Pure Al	6061-T6
density (g/cc)	2.6989	2.70
specific heat capacity (J/g·°C)	0.9	0.896
thermal conductivity (W/mK)	210	167
melting point (°C)	660.37	582 - 651.7

Unlike the AloS pieces, it was necessary for us to subdivide the PAC into smaller pieces. We used piece 50684.5 (see Figure 1.8) which was delivered to St Louis in January of 2005 (Meshik et al. 2006). It is a badly curved piece with some visible physical damage on one end. Using tin snips, we cut off a relatively flat piece: 50684.5.C (Figure 1.7b). This piece was then further subdivided into 17 smaller pieces.

Figure 1.8: Subdivision of the PAC.



Chapter 2 Diffusion Experiment

The goals of the Genesis mission demand very precise analysis, especially for isotopic compositions, thus even minor effects can cause significant perturbations with resulting uncertainties in the final result. Therefore, our goal was to determine and investigate all potential sources of isotopic fractionation, such as diffusive losses, that are often ignored under less stringent requirements. The possibility for even very small losses due to diffusion to measurably alter the isotopic ratios is magnified because, in the solar wind constant velocity stream, different isotopes have different implantation depths. Near the surface, the isotopic composition is “lighter” (lighter isotopes are enriched) and it gets progressively “heavier” with depth due to the greater momentum of the heavier isotopes. Therefore, losses due to diffusion will cause preferential loss of the isotopically lighter component near the surface since, not only are lighter isotopes more mobile, they are also preferentially enriched near the surface due to implantation effects. Step-wise heating experiments done on a few artificially implanted and some flown samples by Meshik et al (2000, 2006) suggested that this possibility was worth investigating further. These studies also indicated that PAC was significantly less retentive (more susceptible to diffusive losses) than AlO₂.

This work is a more extensive diffusion experiment that has been conducted on a time scale similar to the time scale of the Genesis mission. The goals of this work were 1) to determine if the PAC is a suitable collector for light noble gases or else to confirm early indications that it does not retain light gases well enough to preclude reliable

measurements and 2) to check the possibility of diffusive losses of the light gases from AloS under the conditions and duration of the Genesis mission. To validate the accuracy of the SW measurements discussed in Chapter 3, we must eliminate diffusive losses as a possible source of systematic errors that may bias the final results.

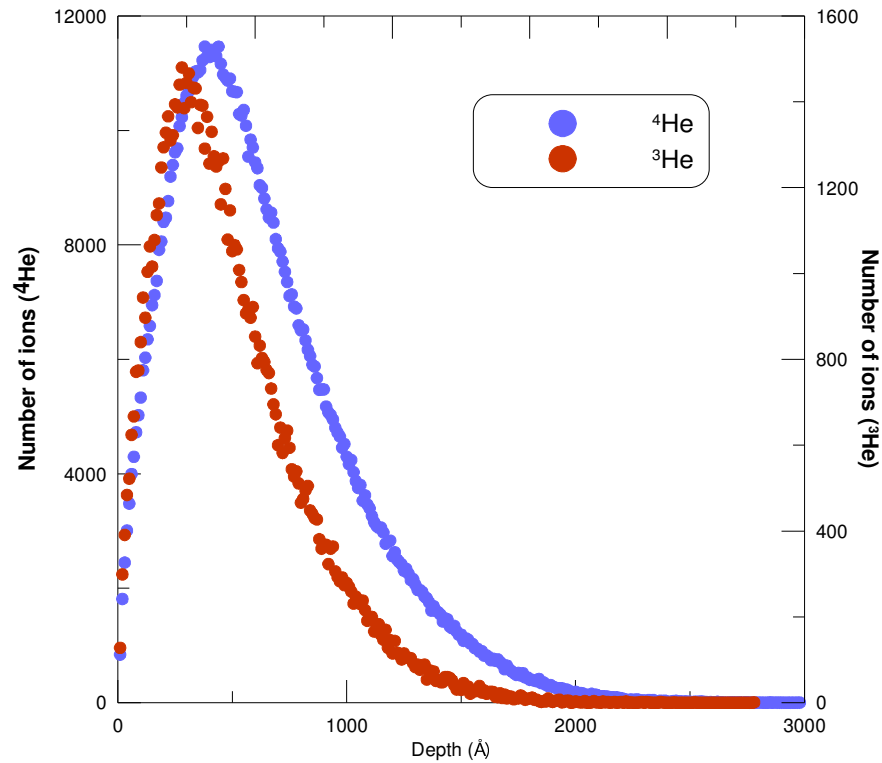
§ 2.1 Implantation and Diffusion Theory

§ 2.1.1 Implantation

Most of the Genesis SW-collectors were passive collectors, they were simply placed in the path of the SW flow and the SW ions were implanted in the collector materials by their own momentum (excluding a small fraction of backscattered ions). The SW ions have energies on the order of 1keV/amu (Axford 1985), and velocities ranging from 200 km/s to 800 km/s (Meyer-Vernet 2007). These energies are in the range where most of the SW ions are implanted in the top 1000 Å of the solid collectors (Jurewicz et al. 2003).

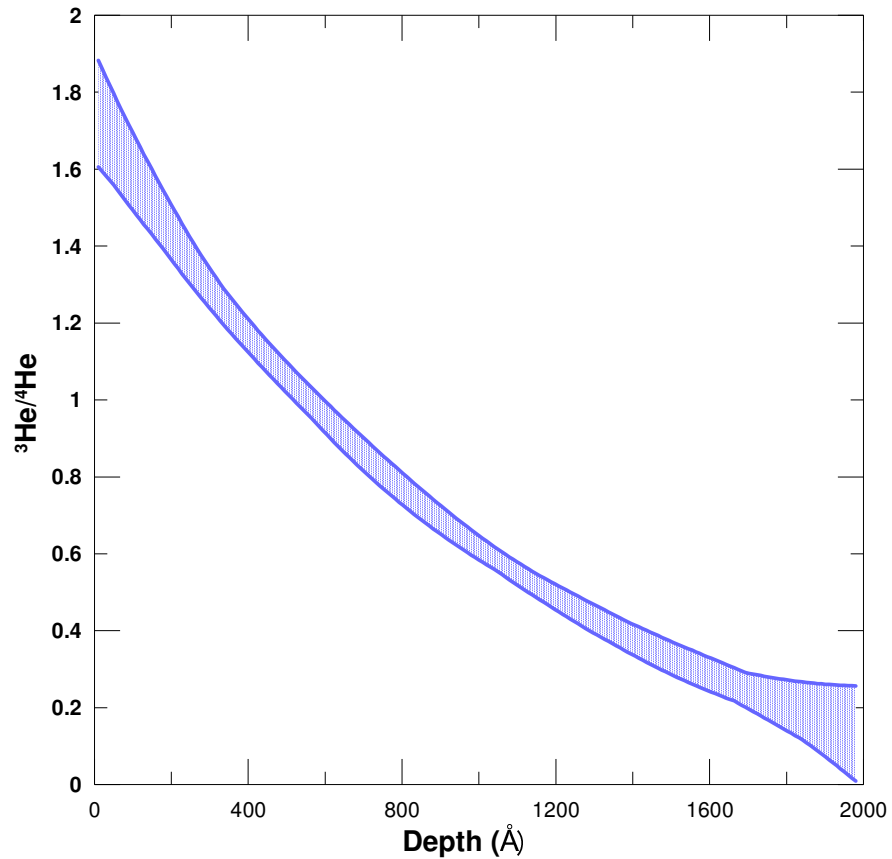
Without any way of directly imaging the depth distribution of implanted SW ions, we use a commonly used program called the Transport of Ions in Matter (TRIM) developed by Ziegler (2004). This program simulates the implantation depths of energetic ions into solid materials, using Monte-Carlo calculations of ion-atom collisions. The input parameters include the atomic weights of the projectile and target and the projectile energy and incident angle. The program then outputs a calculated depth profile (Figure 2.1) and estimates the fraction of backscattered ions.

Figure 2.1: Depth profiles of ^3He and ^4He into 3000-Å Al-film as calculated by TRIM.



The profiles I have used in this work were calculated by Chad Olinger at Los Alamos National Lab, using the energy distribution taken from the monitors on-board the Genesis spacecraft. The implantation profiles have the shape of Pearson functions (Hofker 1975; Tasch et al. 1989; Ashworth et al. 1990) and are shown for ^3He and ^4He in Figure 2.1. Because all of the ions have the same velocity, the heavier ions have more energy and therefore are implanted deeper, leading to a change in the isotopic ratio with depth which can be seen in Figure 2.2.

Figure 2.2: The expected relative change in $^3\text{He}/^4\text{He}$ with depth (99.99% confidence fit to calculated points).



§ 2.1.2 Diffusion

Molecular diffusion is the net transport of molecules from a region of higher concentration to one of lower concentration. Thermally driven diffusion occurs within a solid when molecules have enough thermal energy to jump from one lattice position to another. These jumps will occur in random directions, but will have the net effect of moving molecules from regions of higher concentration to regions of lower concentration. Although some molecules from lower concentration regions will end up

in the regions of higher concentration, there will be proportionally more particles available to move away from the regions of higher concentration and towards regions of lower concentration (McDougall and Harrison 1999).

At thermal equilibrium all molecules will have the same average kinetic energy, but since the velocity is inversely proportional to the square root of the mass, lighter ones will have the higher average velocities. Therefore, the lighter species present themselves at the lattice barriers more often, have more of a chance to penetrate the barriers and thus, diffusion favors transport of the lighter species.

The specifics of diffusion are quantified in Fick's Laws. The laws of diffusion can be applied to many different situations, and in fact, the equations used to describe the diffusion of molecules were adapted from those describing heat conductivity (McDougall and Harrison 1999). There are many excellent derivations of the differential equations which govern the diffusive process (and especially of gases in solids) such as: (Carslaw & Jaeger 1959; Crank 1979; Jost 1960).

Fick's first law says that the mass flux through an area is proportional to the concentration gradient:

$$J = -D \frac{\partial C}{\partial x} \quad (2.1)$$

Where J is the mass flux, C is the concentration, and D is the diffusion coefficient. Fick's second law can be derived using the first law and the conservation of mass of a volume (and assuming that D does not depend on position):

$$\frac{\partial C}{\partial t} = D \frac{\partial^2 C}{\partial x^2} \quad (2.2)$$

This partial differential equation now must be solved for a plane sheet (the geometry of the Genesis collectors) of thickness l , by separation of variables and assuming zero concentration at the boundaries (McDougall and Harrison 1999):

$$C(x, t) = \sum_{n=0}^{\infty} \left(\frac{2}{l}\right) e^{-\left(\frac{n\pi x}{l}\right)^2 Dt} \sin\left(\frac{n\pi x}{l}\right) \int_0^l C(x', 0) \sin\left(\frac{n\pi x'}{l}\right) dx' \quad (2.3)$$

There is one more step needed to make this equation really useful. Since we do not actually measure the concentration profile in the lab, so we cannot use Equation 2.3 as it is to determine the diffusion coefficient. We can, however, compare the differing amounts of gas lost at different temperatures, the fractional loss (f) and we can convert Equation 2.3 using the definition of fractional loss:

$$f \equiv 1 - \frac{M_t}{M_0} \quad (2.4)$$

Where M_t is the amount of diffusant remaining after a heating step and M_0 is the amount before the heating step, and:

$$M_t = \int C(x, t) dV \quad (2.5)$$

So we use Equations 2.3, 2.4, and 2.5 to get a usable form for planar geometry:

$$f = 1 - \frac{\sum_{n=0}^{\infty} \left(\frac{4}{(2n+1)\pi} \right) e^{-\left(\frac{(2n+1)\pi x}{l} \right)^2 Dt} \int_0^l C(x,0) \sin \left(\frac{(2n+1)\pi x}{l} \right) dx}{\int_0^l C(x,0) dx} \quad (2.6)$$

Equation 2.6 is the exact solution for the planar geometry for any initial concentration profile $C(x,0)$, but this equation can be simplified with certain assumptions. One such simplification is to assume a uniform concentration profile: $C(x,0) = C_0$. Approximate forms of Equation 2.6 are shown for this assumption in Table 2.1 (Jain 1958; McDougall and Harrison 1999).

Table 2.1: Diffusion equation solution in fractional loss form for a uniform distribution C_0 and planar geometry of thickness l (Jain 1958; McDougall and Harrison 1999).

$$f = 1 - \sum_{n=1}^{\infty} \frac{8}{(2n+1)^2 \pi^2} e^{-\left(\frac{(2n+1)\pi x}{l} \right)^2 Dt} \quad \text{exact solution for } C(x,0) = C_0$$

$$f \cong \sqrt{\frac{16Dt}{\pi l^2}} \quad 0 < f \leq 0.60$$

$$f \cong 1 - \frac{8}{\pi^2} e^{-\pi^2 Dt/l^2} \quad 0.45 \leq f \leq 1$$

Equation 2.6 and the equations in Table 2.1 can be used directly to calculate the diffusion coefficient for bulk gas extraction, however for step-wise heating extractions a slight modification must be made to account for the effect of one heating step on the subsequent step (Fechtig and Kalbitzer 1966). These equations are shown in Table 2.2.

Table 2.2: Approximate solutions for the diffusion coefficient of the i^{th} step-wise heating step (D_i), for a uniform distribution C_0 and planar geometry of thickness l (Fechtig and Kalbitzer 1966; McDougall and Harrison 1999).

$$D_i/l^2 \cong \frac{\pi}{16t_i} (f_i^2 - f_{i-1}^2) \quad 0 < f \leq 0.60$$

$$D_i/l^2 \cong \frac{-1}{\pi^2 t_i} \ln \left(\frac{1 - f_i}{1 - f_{i-1}} \right) \quad 0.45 \leq f \leq 1$$

Different temperatures will yield different diffusion coefficients, that obey the Arrhenius law: $D = D_0 e^{-E_a/RT}$, where E_a is the activation energy, R is the gas constant, T is the absolute temperature, and D_0 is the frequency factor. The activation energy is the energy necessary for the implanted ion to jump from one position to another (Fechtig and Kalbitzer 1966). If one can experimentally determine D at a few temperatures, the Arrhenius equation can be used to determine these parameters E_a and D_0 , and can therefore calculate D for other temperatures.

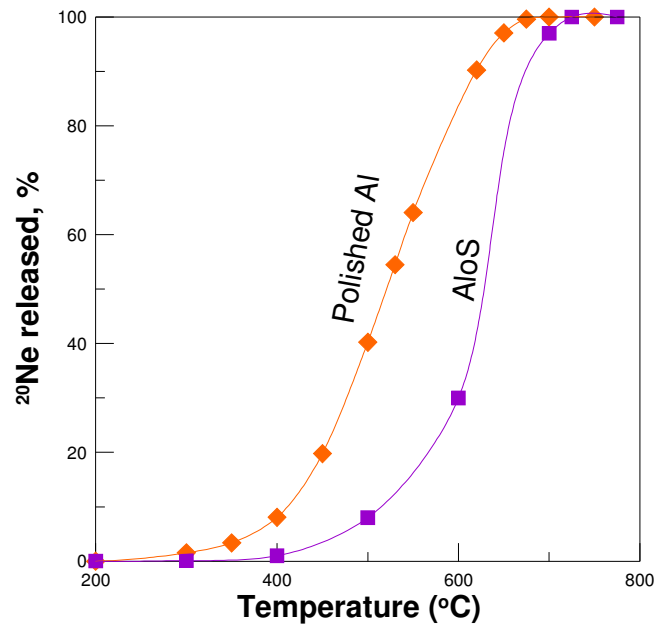
§ 2.2 Motivation

Earlier studies by Meshik et al (2000, 2006) suggested that diffusive losses can have a significant impact on the measured isotopic compositions of the light noble gases. This provided the motivation to do a more in-depth diffusion experiment and characterize the diffusive properties of the light noble gases (helium, neon and argon) in two different Genesis aluminum collectors: AloS and PAC. These collector materials are described in more detail in § 1.4. If significant mobility by diffusion did occur, it could change the apparent isotopic and elemental compositions of gases in the affected SW collectors. If

gases were lost out of the surface layer of the sample material, then because mass-dependent implantation-depth favors light species near the surface, and because diffusion also favors the light isotopes, proportionally more of the lighter masses would be lost, thereby altering the measured isotopic (and elemental) ratios. This could clearly compromise the Genesis goal of measuring isotopic ratios to sub-percent precision (Burnett et al. 2003).

The first motivation for doing actual diffusion experiments on these samples comes from analysis of Ne released from step-wise heated AloS and PAC collectors which were artificially implanted with ^{20}Ne and H at solar wind energies at Los Alamos National Laboratory with doses of 10^{12} and 3×10^{16} atoms/cm², respectively, to model the expected fluences for the Genesis mission (Meshik et al. 2000). In this study, gases were released from the sample incrementally by step-wise heating (see § 2.3.2.1 for detailed explanation of the step-wise heating technique), and the temperature release profiles show that the ^{20}Ne is released at lower temperatures from the PAC than from AloS, as seen in Figure 2.3. The earlier release of gases from PAC means there exists a greater mobility of Ne in this material and that it has the potential to lose light gases due to diffusion at lower temperatures than the AloS. Figure 2.3 shows that at 400 °C, the PAC has lost about 8% of its ^{20}Ne , while at the same temperature AloS has lost only around 1%. This effect will be even greater for helium.

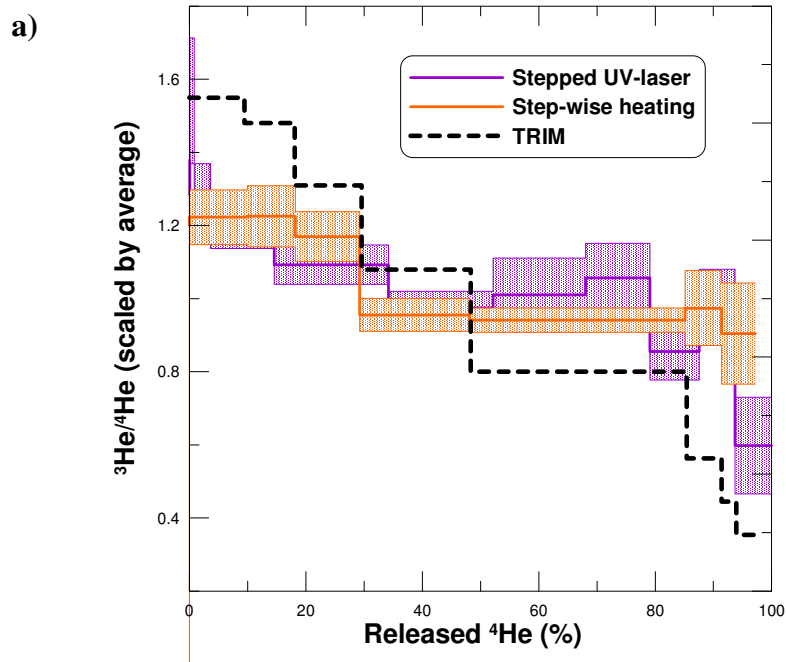
Figure 2.3: ^{20}Ne temperature release profiles from PAC and Al₂O₃ (Meshik et al. 2006).

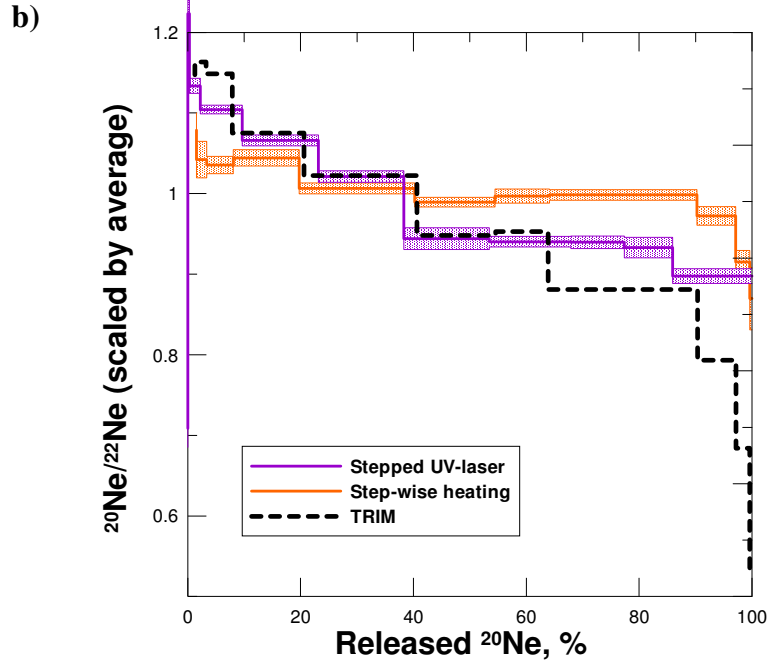


The second motivation comes from analysis of flown PAC samples from Genesis, using two different gas extraction techniques: step-wise heating and stepped UV-laser rastering. The latter method involves ablation of an area on the sample with a UV-laser beam with incrementally increased power density, with each subsequent raster retrieving gases from deeper and deeper layers within the sample. For these measurements it was possible to look at the release profiles of specific isotopic ratios. The $^3\text{He}/^4\text{He}$ and $^{20}\text{Ne}/^{22}\text{Ne}$ release profiles are shown in Figure 2.4 along with the expected implantation profile as calculated using TRIM, shown with the same release steps as the step-wise heating. The $^3\text{He}/^4\text{He}$ release profiles (Figure 2.4a) by both techniques largely overlap, however the ratio does not decrease with the steepness expected by TRIM for the implantation profile. The measured $^3\text{He}/^4\text{He}$ are lower in the earlier steps and higher in the later steps than predicted by TRIM. This suggests a post-implantation modification

of the profile, with broadening of the original profile being an indication of diffusional redistribution of implanted SW. The $^{20}\text{Ne}/^{22}\text{Ne}$ profile (Figure 2.4b) matches TRIM better, especially in the earlier steps, although it is somewhat lower in the very beginning and significantly higher in the later steps. In this case the step-wise heating profile is flatter than either the stepped UV-laser or TRIM profiles.

Figure 2.4: $^3\text{He}/^4\text{He}$ (a) and $^{20}\text{Ne}/^{22}\text{Ne}$ (b) step-wise release profiles from PAC for two different gas release techniques: step-wise heating (orange) and stepped UV-laser (purple) (Mabry et al. 2008). Ratios are normalized to the average value of the all steps in order to compare the profile shape with the calculated TRIM profile. The accuracy of the comparison depends on complete recovery of all implanted gas from the sample.





In addition the measured $^3\text{He}/^4\text{He}$ and $^{20}\text{Ne}/^{22}\text{Ne}$ ratios from the PAC were lower than AloS (Table 2.3). Since the PAC seems to be more susceptible to diffusive losses than AloS, this is probably evidence that diffusive losses may have, in fact, significantly alter the measured isotopic composition of the implanted gases.

Table 2.3: Helium and neon measured isotopic ratios from AloS and PAC.

Material	$^3\text{He}/^4\text{He} (\times 10^{-4})$	$^{20}\text{Ne}/^{22}\text{Ne}$
AloS	4.33 ± 0.03	13.97 ± 0.05
PAC	4.18 ± 0.02	13.57 ± 0.06

The long-term diffusion experiment was designed and carried out to confirm if there are indeed diffusive losses from the PAC and to determine whether there are diffusive losses from the AloS as well. Although it appears that losses from the AloS would be less than PAC, they could still be significant enough to alter measured isotopic composition, and thus they must be evaluated.

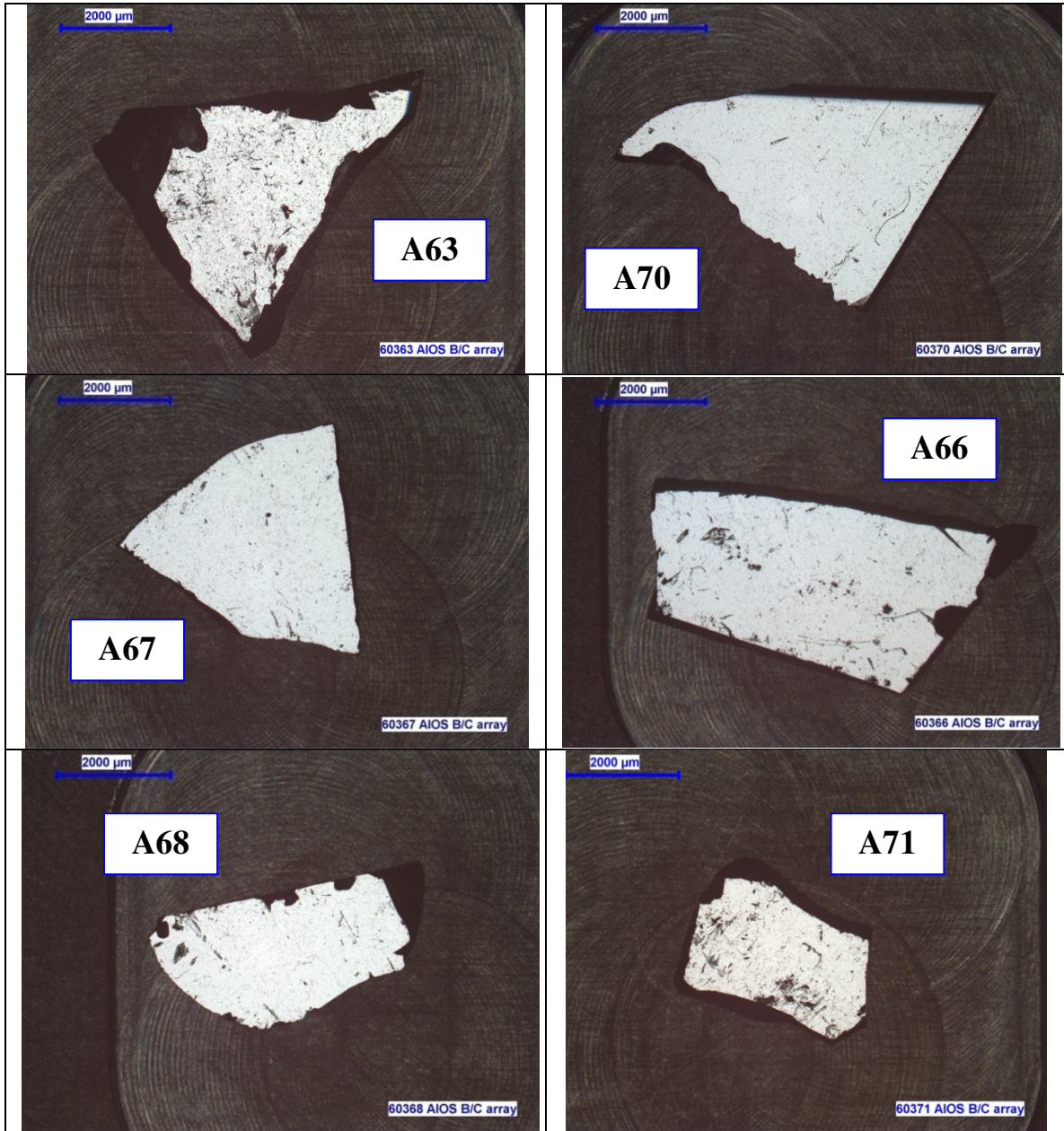
§ 2.3 Methods: Diffusion Experiment

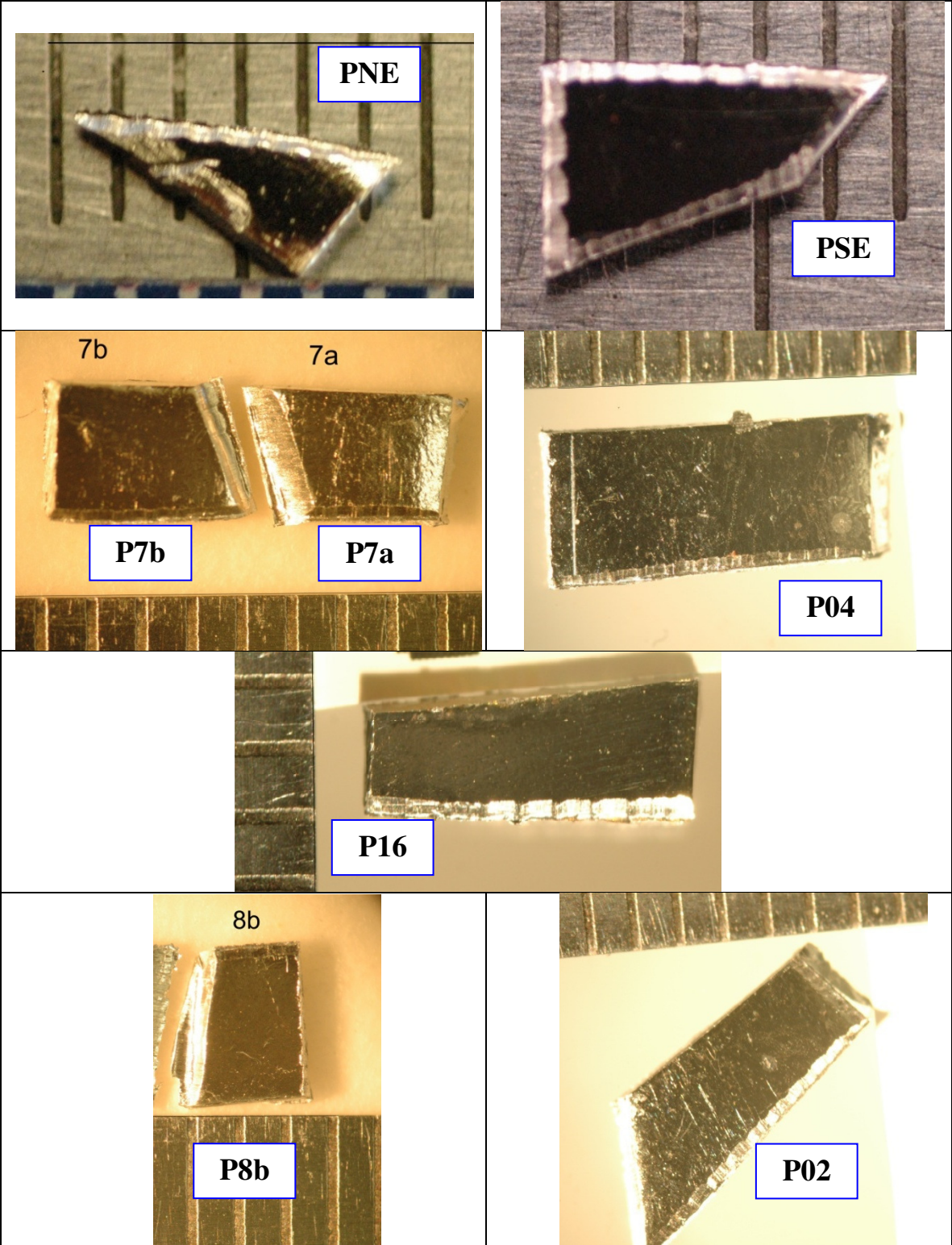
§ 2.3.1 Real-Time Diffusion Bake

Individual pieces of the two different Genesis noble gas collectors, PAC and AloS, were heated in vacuum at six different temperatures between 160 °C and 360 °C for 322 days (with several reference samples kept at room temperature). These temperatures were thought to represent the range of the most likely temperatures reached by the targets during the collection phase of the mission, and represent critical temperatures suggested by the step-wise heating experiments. Although the thermal properties of the AloS surface material was controlled and modeled, there was less attention paid to the PAC, so it is not known with certainty what temperatures either of the actual targets reached during the mission, as will be discussed further in § 2.4.4.

The AloS pieces chosen for this experiment were fragments from the bulk collector that had areas on the order of 10 mm². The areas of the AloS pieces were measured by the Genesis curation team at JSC using high-resolution images of the pieces and the imaging program Canvas X. The upper limit listed in Table 2.4 is the area found from tracing the outline of the Al film. The lower limit area is found by subtracting all dark patches from the upper limit area. This was done in an attempt to account for scratches in the film acquired during the crash. However, this method cannot distinguish between surface particles and shadows, and true scratches, so it may slightly over-correct the areas. I have used the lower limit areas in this work, as they should be closest to the true value.

Figure 2.5: Images of AlO₃ and PAC pieces used in diffusion experiment. AlO₃ images were taken at Johnson Space Center. PAC images were taken at Washington University.





Two of the PAC pieces used in this experiment came from an earlier subdivision (Meshik et al. 2006). The other six are pieces of 50684.5.c (Figure 1.8). The least damaged samples were chosen for this experiment. The areas of the PAC pieces were measured by me with high-resolution images using the program Paint.net. In addition to scratches, some of the PAC samples were slightly curved, and the cutting procedure leaves the edges angled instead of having a straight edge. I measured the entire visible area in the image for the upper limit area and measured just the darker inner area for the lower limit. In this case I have used the average area.

Table 2.4: Flown Genesis SW-collectors used in diffusion experiment. The chosen areas are shown in bold.

Material	Sample Number (Label)	Bake Temperature (°C)	Area – lower limit (mm²)	Area – upper limit (mm²)	Area – Avg (mm²)
AloS	60370 (A70)	unbaked	12.22	13.25	12.73
AloS	60363 (A63)	unbaked	8.55	9.98	9.26
AloS	60367 (A67)	240	10.33	10.99	10.66
AloS	60366 (A66)	280	13.43	15.32	14.37
AloS	60368 (A68)	320	7.27	7.84	7.56
AloS	60371 (A71)	360	4.77	5.83	5.30
PAC	(PNE)	unbaked	2.8	6.1	4.5
PAC	(PSE)	unbaked	6.5	10	8.3
PAC	50864.5.c7.b (P7b)	240	7.6	11.1	9.4
PAC	50864.5.c7.a (P7a)	240	6.8	10.4	8.6
PAC	50864.5.c4 (P04)	320	22.1	27	24.6
PAC	50864.5.c16 (P16)	unbaked	8.6	10.7	9.7
PAC	50864.5.c8b (P8b)	240	5.9	8.9	7.4
PAC	50864.5.c2 (P02)	360	13.2	17.6	15.4

We made six identical stainless steel fingers and put into each one Al₂O₃ and two PAC fragments (see Figure 2.5 for images) of areas on the order of 10 mm² (see Table 2.4 for details) and kept all pieces under vacuum (Figure 2.7). Each sample was wrapped individually in aluminum foil to promote thermal uniformity and contact and to avoid further scratching by direct contact with stainless steel and sapphires edges. Then we wound 36-AWG nichrome heaters around a copper body which fitted snugly around the length of the stainless steel finger. Each finger was separately insulated with silicon tape, fiberglass, and finally by multilayer Al-foil thermal shields. All of this was done to keep the volume inside the finger evenly heated and uniform in temperature. The ovens were controlled with TC-408 programmable PID temperature controllers, which can maintain the temperature to within 0.2%. Chromel-alumel thermocouples were located in the middles of the heaters. The temperature controllers were also connected to a latching relay which shuts off all of the heaters if any one of the controllers measures a temperature 5 °C above or below the set temperature, or in case of power interruption or surges.

Figure 2.6: Vacuum manifold where the AlO₃ and PAC samples were baked. Each finger contained pieces of each target and an oven was slid over the finger and then thermally insulated.



The total duration of the diffusion experiment bake was 346 days, however there were six occasions on which the heaters were shut off, lessening the actual total bake time. On two occasions, one of the heaters failed, but the relay protection worked as designed, shutting off all of the heaters so that all the pieces were baked for the same amount of time (to within ~10 minutes). In January 2008 (after the heater failures) we installed a temperature monitor which logged the temperature at set intervals. These data could be downloaded to a computer. Thus, we were able to see exactly at what time the heaters switched off because of failures and subtract the correct amount of time from the total. The four other incidents were as a result of power surges or failures due to electrical storms. A summary of the total bake time is given in Table 2.5.

Table 2.5: Timeline of the long-term diffusion experiment.

Date	Event
30 July 2007	Heaters switched on
December 2007	Heater failure: unknown total time, between 9 and 17 days
10 Jan 2008	Heater failure: ~1 day
30 Jan 2008	Power surge/failure: heaters switched off 5 days
12 May 2008	Power surge/failure: heaters off 26.5 hours
27 May 2008	Power surge/failure: heaters off 4.5 days
24 June 2008	Glitches: heaters switched on and off several times over 3 days, heaters off for a total of 45 hours
11 July 2008	End of experiment
Total Time Between 7640 and 7832 hours → Avg = 7736 hours (322 days)	

§ 2.3.2 Noble Gas Measurements

The best way to measure the light SW noble gases is with a multi-collector system which has an extended dynamic range, employing a Faraday cup in addition to secondary electron multipliers. In collaboration with GV Instruments (now Thermo-Fisher), we developed a mass spectrometer specifically to measure the light SW noble gases. Unfortunately, they were unable to deliver the finished product, and after several years of working with them, and the multitude of companies involved with the numerous mergers, we decided to go ahead with measurements using our existing mass spectrometers, which were originally designed primarily to measure the heavy noble gases (Ar, Kr, and Xe).

Our first analysis of He and Ne ran into problems because of the large amount of H in the SW. This led to interferences at mass-3 (HD^+ and H_3^+) and mass-21 ($^{20}\text{NeH}^+$), due to

hydrogen-driven ion chemistry, as well as pressure dependent sensitivities characteristic of the GS-61 ion source. Eventually, special calibrations were designed to quantify and correct for these effects, which seemed to work well for the Ne measurements (discussed in Chapter 3), but He measurements still showed too much scatter to be reliable and therefore will not be discussed. Before measuring the light gases for the diffusion experiment, an additional getter was installed to remove most of the solar wind H. While this eliminated the need for the large hydride corrections at mass 21, there still was a large amount of He causing significant pressure effects that must be corrected for.

In contrast to He and Ne, the corrections required for the Ar data were minor. Ar was first frozen on activated charcoal at liquid nitrogen temperature, separating it from the more abundant He and Ne, and therefore eliminating pressure effects. The surface area of the sample was chosen to release enough Ar for good counting statistics, but not sufficient to cause pressure effects, an ideal balance. Replacing the entire extraction line prior to Genesis measurements was essential. During the preparation of this line, all vacuum components were internally electropolished which dramatically reduced the microscopic surface area and Ar background (blank). Only de-ionized water was used for rinsing and cleaning, reducing the Cl contamination which causes interferences on Ar isotopes.

§ 2.3.2.1 Gas Extraction

First the samples (still wrapped in foil) are loaded into the mass spectrometer extraction system in a glass sample tree (Figure 2.7). Directly below the ‘stem’ of the

sample tree is an oven. A gate valve was installed between the sample tree and the oven to isolate the glass from the rest of the extraction system during extractions as helium leaks in through the glass raising the helium background.

The technique used for extracting the gas from the samples was high-resolution step-wise heating. With this technique the sample is incrementally heated up through a series of temperatures, with the gas analyzed from each temperature step separately, as opposed to simply melting the sample and releasing all of the gas at one time. As the sample heats up, the gases begin to diffuse out, with near surface gases being released in the early lower temperature steps, and gases from deeper within the sample being released in later higher temperature steps. Therefore, although we cannot directly measure the depth distribution of gases in the sample, with this technique we can see the relative distribution. The highest temperature step was above the melting point of the sample material in order to be sure of complete extraction of all gases from within the sample.

For these Al samples, step-wise heating steps were 45 minutes each starting at 200 °C and going up to 850 °C (well above the melting temperature of Al at 660°C), in temperature increments ranging from 25 °C to 100 °C. The smallest temperature steps were chosen around the peak release of He. The oven temperature was controlled with a microprocessor based PID temperature controller (Athena Legacy Series 16). After each temperature step the gas which was released is moved through the system for processing and analysis.

§ 2.3.2.2 Mass Spectrometry

Two mass spectrometers were used for the analysis: He and Ne together in one mass spectrometer ('MS-South'), and cryogenically separated Ar for analysis in a second mass spectrometer ('MS-North'). MS-North and MS-South were built in-house by Charles Hohenberg (1980) in the 1970's using a 90° magnetic sector configuration and Baur-Signer ion source. They are both high-sensitivity, low resolution ($M/\Delta M < 300$) machines. Ions are counted using a single electron multiplier with discrete dynodes. To measure different masses, the magnetic field is changed using a Bruker B-H15 field controller. The typical electron emission is 150 μA at 100 eV electron energy, however, for the analysis of the SW light noble gases it was necessary to reduce these values to 100 μA at 48 eV to minimize interferences from H and ^{40}Ar .

The gas released from the sample was cleaned by exposure to two types of titanium-based getters which employ chemical sorption of reactive gases and compounds (such as CO, CO₂, H₂, and H₂O). The gas extracted from the sample was first exposed sequentially to two 'bulk' (SAES ST-707 alloy Non-Evaporative Getter pump) getters at 275 °C for 5 minutes each. These getters consist of a proprietary compound with the following nominal composition: 70% Zirconium, 24.6% Vanadium, and 5.4% Iron, sintered into high-surface-area pellets. They must be periodically activated at 450 °C for ~10 minutes to activate the Ti surface. Then, for additional fine stage cleaning, the bulk-cleaned gas is exposed to a Ti 'flash' getter (a W filament wrapped with Ti wire) which has a smaller capacity than the bulk getters. When 'flushed' (daily), the filament is

heated up by running 19 A through the Ti-coated 0.5-mm W-wire for 15 s until the Ti sublimates and condenses onto the large surface of the getter housing. This freshly deposited Ti mirror binds chemically active species (and later flashes bury them by covering with newly deposited Ti), leaving only the noble gases for analysis.

At this point, the gas was exposed to a stainless steel finger filled with activated charcoal cooled with liquid nitrogen to $-196\text{ }^{\circ}\text{C}$ for 45 minutes in order to separate the Ar (and Kr and Xe) from He and Ne. In Genesis samples the quantities of Kr and Xe are too small to be analyzed with these small areas. After 45 minutes when all heavy noble gases were trapped by the cold charcoal, the clean He and Ne gas was admitted into MS-South for analysis. Argon is now separated from the much more abundant H, He and Ne, a point that will be addressed later and one that provides much more certainty to the measured Ar data. The Ar was subsequently thawed off the charcoal, and let into MS-North for analysis. Table 2.6 summarizes the full procedure used for He, Ne, and Ar isotopes.

Figure 2.7: Noble gas extraction and cleaning system.

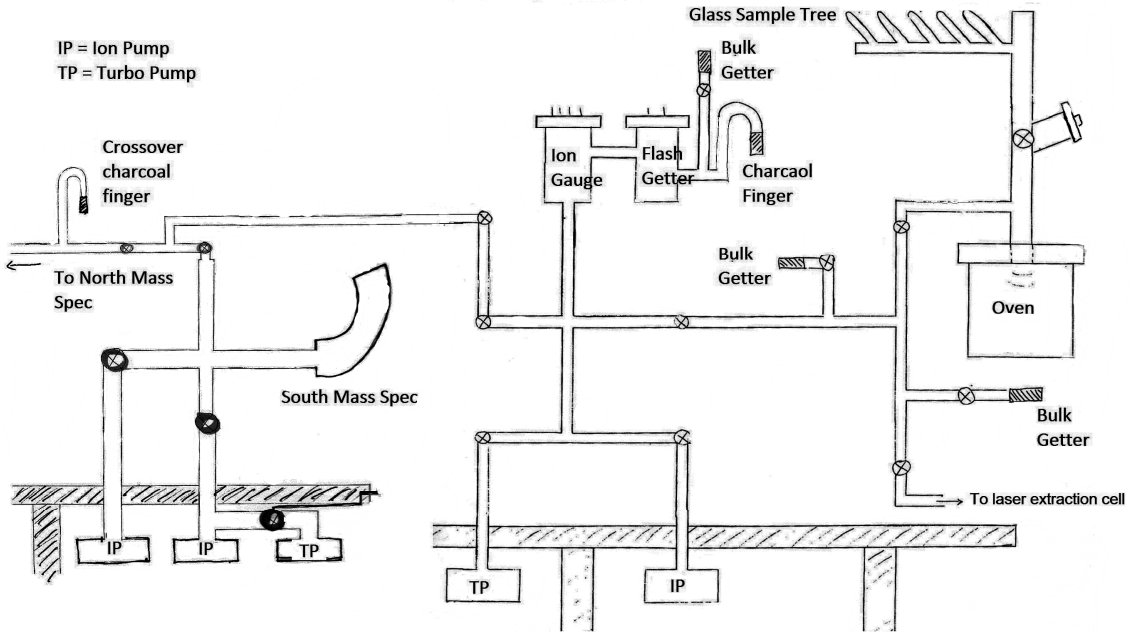


Table 2.6: Procedure for preparation of He, Ne, and Ar for mass spectrometric analysis for step-wise heating experiments.

<u>Before starting:</u>
1. Bulk getters heated to 275 °C
2. Oven temperature set to 50 -150 °C below current temperature-step (5-10 min, while getters heat up, pumps open)
3. Close pumps and set oven to current step temp, wait 35 min
4. Expose gas to first bulk getter for 5 min
5. Expose gas to second bulk getter and flash getter for 5 min
6. Put liquid nitrogen on sample system and crossover charcoals for and let argon freeze for 45 min
7. Let clean He and Ne gas into MS-South for 3 min
8. Begin He and Ne measurements
9. Remove liquid nitrogen from sample system charcoal thaw of argon for 25 min
10. After He/Ne measurements are done, heat up crossover charcoal for 15 min
11. Let Ar into MS-North for 3 min
12. Begin Ar measurement

If not completely removed by getters in the extraction line, the large amount of H in SW samples causes a lot of interferences especially on mass-21 (^{20}NeH neon hydride interference) and mass-3 ($\text{HD}+\text{H}_3$ interference). Therefore, we installed an SAES NP-10 getter in MS-South, to keep the hydrogen partial pressure low.

During He and Ne measurements, a charcoal finger connected to MS-South was kept cooled with liquid nitrogen in order to trap the ^{40}Ar ubiquitously leaking into the mass spectrometer and therefore reduce the steady-state amount of $^{40}\text{Ar}^{++}$ which interferes on mass-20. With the cold charcoal finger the amount of ^{40}Ar was usually less than 2.5×10^{-12} ccSTP, making the interference correction for ^{20}Ne insignificant.

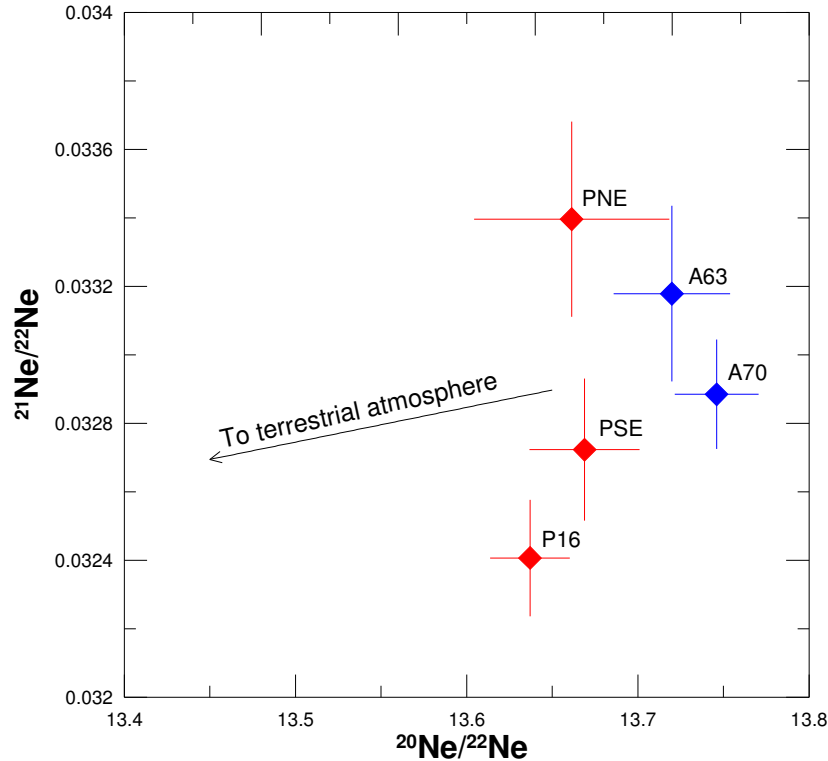
For each set of Ne+He measurements masses 2, 3, 4, 18, 19, 20, 21, 21.5, 22, 40, and 44 are measured in sequence. During each run, the magnetic field controller jumped from mass to mass and each measurement was integrated for 3 to 15 s (depending on relative amount). A total of 25 to 30 sweeps are done for each set. Before the start of measurements, the peak centering routine was run. Additionally, masses 2, 3, and 4 were centered before each sweep during measurements. Mass 21.5 was measured to check the baseline ('zero' thus monitoring any stray scattered ions, usually indicating the presence of some large unexpected, and probably insufficiently cleaned, species, most often inadequately removed hydrogen), masses 2, 18, 19, 40, and 44 were measured to correct for interferences on masses 3, 20, 21, and 22. Generally there were no indications of significant scattered ions at mass 21.5.

After He and Ne were admitted into MS-South, the sample system was pumped out for 3-5 minutes, and then the sample system charcoal finger was warmed for 25 minutes to release the adsorbed argon gas. For the Ar analysis, masses 40, 39, 38, 37, 36.5, 36, and 35 were measured. Following a similar procedure as for He and Ne, with 36.5 as the zero. Masses 39, 37, and 35 were measured to provide information for interference corrections, the most important were due to HCl^+ , which was monitored by Cl at masses 35 and 37.

§ 2.3.2.1 Blanks and Standards

To determine and take into account instrumental background level (blank), I did a full procedure step-wise heating blank using a piece of foil of the type and approximate size as that used to wrap the samples. The empty piece of foil was dropped into the oven and then treated as a regular sample. These data are shown in Appendix A. After evaluating the data, I determined that no formal blank subtraction was necessary. First, Ne 3-isotope plots, such as the one shown in Figure 2.8, do not give any indication of mixing of SW with terrestrial atmosphere. Also, after subtracting blank, the changes to the bulk (total of all steps) isotopic ratios were all less than 1σ statistical errors ($< 0.2\%$). However, for a few of the smallest samples, there were blank contributions to the total amounts of ^{20}Ne of up to 5%. This contribution came entirely from the very highest temperature steps (after most of the SW had been released), and so these steps were not included in the final bulk data (shown crossed out in the data tables in Appendix A).

Figure 2.8: Neon 3-isotope plot showing bulk isotopic ratios from the five unbaked samples, along with the direction to the terrestrial atmospheric value. There is no apparent mixing between the SW values and the terrestrial atmosphere.



Since these measurements took about 6 months to complete, running frequent air standards was especially important as sensitivity and instrumental mass discrimination can vary significantly over such a long period of time. One or more standards were run between each sample (a full step-wise heating run of a sample typically lasted about a week). Because terrestrial atmospheric and solar relative abundances (Table 2.7) are dramatically different, it is difficult to use an atmospheric standard to calibrate all values. In the terrestrial atmosphere, Ar is more abundant than Ne, which is more abundant than He. But in the SW, it is the opposite, with He the most abundant, and Ar the least abundant. The $^3\text{He}/^4\text{He}$ ratios (Table 2.7) also differ by several orders of magnitude,

making them difficult to calibrate as well. Therefore, it was necessary to use three separate standards for these measurements: our regular air standard purified from chemically active gases ('am-air'), a ^3He - ^4He mixture prepared by Chemgas ('chemgas-helium'), and an additional air standard ('jcm-air').

Table 2.7: Elemental and helium isotopic ratios for the light nobles gases in the terrestrial atmosphere (Mamyrin et al. 1970; Verniani 1966) and the previously measured SW values from the SWC experiment (Cerutti 1974; Geiss et al. 1972)

Source	$^4\text{He}/^{20}\text{Ne}$	$^{20}\text{Ne}/^{36}\text{Ar}$	$^3\text{He}/^4\text{He}$
Terrestrial Atm.	0.319	0.524	1.4×10^{-6}
SW	550	48.5	4.25×10^{-4}

Instrumental mass discrimination for neon and argon isotopes was monitored using frequently run standards of am-air. For neon isotopes the correction was typically ~2% per amu, while for argon isotopes the correction was typically ~0.5% per amu. Uncertainties in these corrections are typically on the order of a few per mil.

Our regular air standard (am-air), has automated pneumatically controlled valves and used for calibrating neon and argon isotopes and neon/argon. However, the $^3\text{He}/^4\text{He}$ ratio in terrestrial air (Table 2.7) is several orders of magnitude smaller than in the SW, and our low resolution mass spectrometers are not capable of measuring atmospheric ^3He and therefore atmospheric He is not suitable to calibrate the instrumental discrimination. To solve this problem, we obtained a commercially prepared mixture from Chemgas with a $^3\text{He}/^4\text{He}$ of $6.5 \times 10^{-4} \pm 1.0\%$ and made a separate helium calibration standard. The ^3He to ^4He instrumental mass discrimination correction factor was found using chemgas-helium to be 9.4%, favoring ^3He . This correction factor did not change appreciably over the time

that the new helium standards were run, however, we did not get that helium standard until about half way through sample measurements so it is possible that there could have been some variation in the correction factor before we had the standard.

While attempting to calibrate the He/Ne sensitivity ratio, we discovered that am-air was apparently made in an atmosphere of excess helium, which likely came from leaking liquid He lines from another laboratory in the building, making am-air useless for this calibration. After discovering this, we made another air standard (jcm-air) with air from outside (far away from any helium source) to use instead.

Since the mass resolution of these machines is insufficient to resolve isobaric interferences, the size of each of these interferences has to be determined separately and then corrected for. Helium interferences come mainly from HD and H₃ at mass 3. After the installation of SAES NP-10 getter in MS-South, the amount of hydrogen during analysis was reduced by 3 to 4 orders of magnitude, making this interference less than 1% for the smaller samples, less than 0.5% for the larger samples. No interference corrections are needed at mass 4.

There are multiple interferences on the neon isotopes that must be considered, however all were quite small during these measurements. The interference corrections and percentages are shown in Table 2.8. The interferences on mass 20 come primarily from four sources: ⁴⁰Ar⁺⁺, hydrogen fluoride, 'heavy water' D₂O⁺, and H₂¹⁸O⁺. To determine the size of the interference corrections from all sources at mass 20, we first determine the ⁴⁰Ar⁺⁺ correction, calibrated by letting a large amount of argon and

measuring mass-20, all of which is $^{40}\text{Ar}^{++}$, then correcting for $^{40}\text{Ar}^{++}$ from the measured ^{40}Ar in the sample. For D_2O and H_2^{18}O corrections, we use the standard ratios: $\text{D}/\text{H} = 1.5 \times 10^{-4}$ and $^{18}\text{O}/^{16}\text{O} = 0.002$. And finally for the HF correction we monitor F at mass 19 and correct mass 20 accordingly, using several blanks in which we have subtracted the other three interferences and attributed what is left to HF. The HF correction is always quite small.

The interferences at mass 22 come mainly from CO_2^{++} . This correction is determined by measuring mass-22 when there is no neon (blank), and therefore everything at mass 22 is from CO_2^{++} . By measuring mass 44, and correcting 22 accordingly, the CO_2^{++} correction is readily made and given in Table 2.8.

The main interferences for argon come from HCl: H^{35}Cl^+ for mass-36 and H^{37}Cl^+ for mass-38. These corrections are determined, similar to the neon corrections, by looking at argon background, when there is no appreciable Ar, and seeing how many counts there are at masses 36 and 38 relative to the observed counts of Cl at masses 35 and 37. The ratio of the mass-36 and mass-38 counts to the counts rates at mass-35 or mass-37 then provides the necessary Cl interference corrections. A relatively constant amount of chlorine is always present in the mass spectrometer, some of which comes from the extraction system, and this is true during the runs, so Cl corrections are straight forward. For the Genesis measurements efforts were made to reduce Cl corrections by installing a new cleaner extraction line. During the preparation of all vacuum components for this line, the use of tap water was carefully avoided in rinsing after internal electropolishing

and final cleaning was done with pure solvents and de-ionized water. This dramatically reduced the amount of Cl contamination making HCl interferences negligible.

Table 2.8: Summary of neon and argon interference corrections for the time period June 2008 to November 2008 when Genesis diffusion measurements were being done.

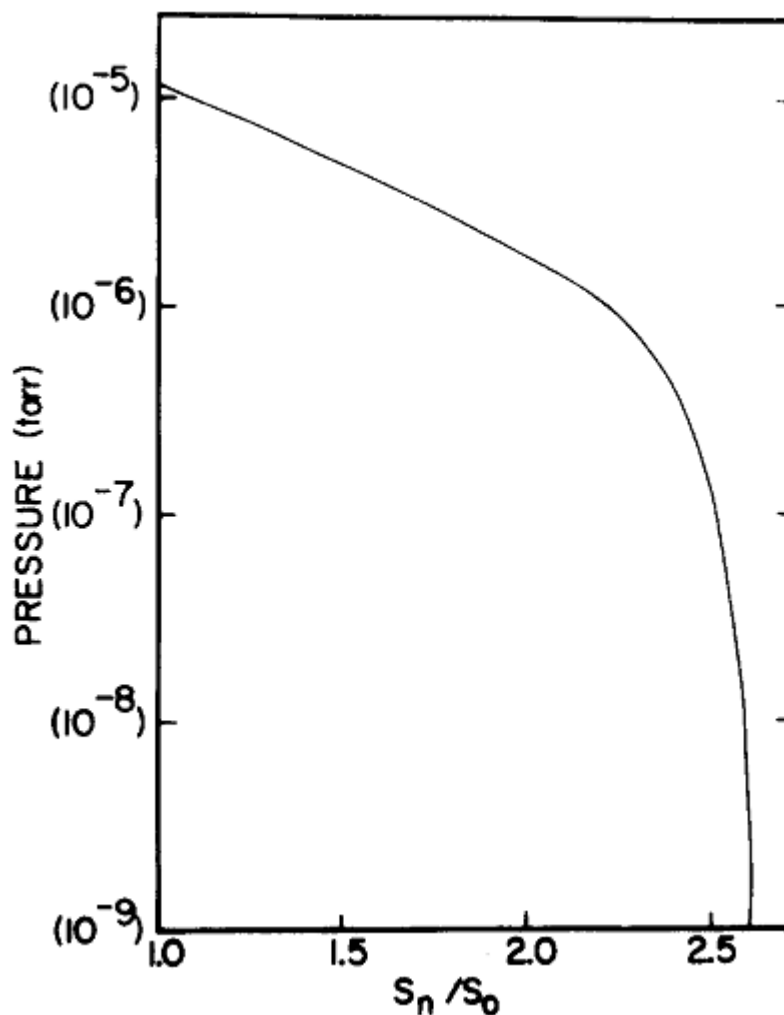
Interference	Correction Factor	Typical, %
$^{40}\text{Ar}^{++}/^{40}\text{Ar}^+$	0.0172	0.01
$\text{D}_2\text{O}/\text{H}_2\text{O}^{18}/\text{H}_2\text{O}^+$	2.15E-3	0.025
HF^+/F^+	1.45E-2	0.3
$\text{CO}_2^{++}/\text{CO}_2^+$	1.35E-3	0.2
H^{35}Cl^+	1.18E-3	0.5
H^{37}Cl^+	2.171E-3	0.2

§ 2.3.2.2 Data reduction

The raw collected data are stored in Unix computers and treated by various FORTRAN processing programs: ‘preanna’, ‘anna’, and ‘ofu’ (written over two decades by C. M. Hohenberg, R. J. Drozd (1974), G. B. Hudson (1981) and T. D. Swindle (1986) and slightly modified by R. H. Nichols (1992) and K. Kehm (2000)). First, the interference corrections are calculated and subtracted off on a sweep-by sweep basis (preanna), then the instrumental mass discrimination correction and dead-time corrections are applied (anna), and finally a file is created (ofu) that keeps track of all correlated errors. Simple error propagation cannot be applied when isotopic ratios are involved and components are subtracted (blanks, corrections, etc). Correlated errors were introduced since the ratios are not truly independent, and correct error propagation involves computations with an error tensor, a N x N array, where N is the number of isotopes.

Atmospheric argon is first subtracted by assuming that all of the ^{40}Ar is atmospheric, solar $^{40}\text{Ar}/^{36}\text{Ar}$ is estimated to be $\sim 3 \times 10^{-4}$ or less (Anders and Grevesse 1989; Begemann et al. 1976), while for the atmosphere it is 296.5, justifying this assumption. The standard ratios for atmospheric argon are generally taken to be $^{36}\text{Ar}/^{40}\text{Ar} = 0.003378 \pm 0.000006$, and $^{38}\text{Ar}/^{40}\text{Ar} = 0.000635 \pm 0.000001$ (Ozima and Podosek 2001), although new values were recently published: $^{36}\text{Ar}/^{40}\text{Ar} = 0.003350 \pm 0.000004$, and $^{38}\text{Ar}/^{40}\text{Ar} = 0.0006314 \pm 0.000001$ (Lee et al. 2006). We used “the classical” generally accepted values, but that matters little here. In these measurements the typical $^{40}\text{Ar}/^{36}\text{Ar}$ ranged between atmospheric in the earliest temperature steps, down to $^{40}\text{Ar}/^{36}\text{Ar} = 5$ in the largest fractions of SW. Clearly, contributions from atmospheric Ar were totally negligible in the fractions containing SW. After the subtraction of atmospheric Ar, the average isotopic ratios are determined by adding up the total amounts of ^{36}Ar and ^{38}Ar (separately) and dividing, with the error found by compounding individual statistical errors (Meshik et al. 2007).

Figure 2.9: Pressure versus the nominal sensitivity (S_n) normalized to the sensitivity measured at 10^{-5} torr (S_0). It is nonlinear at pressures greater than $\sim 10^{-7}$ torr (Hohenberg 1980).

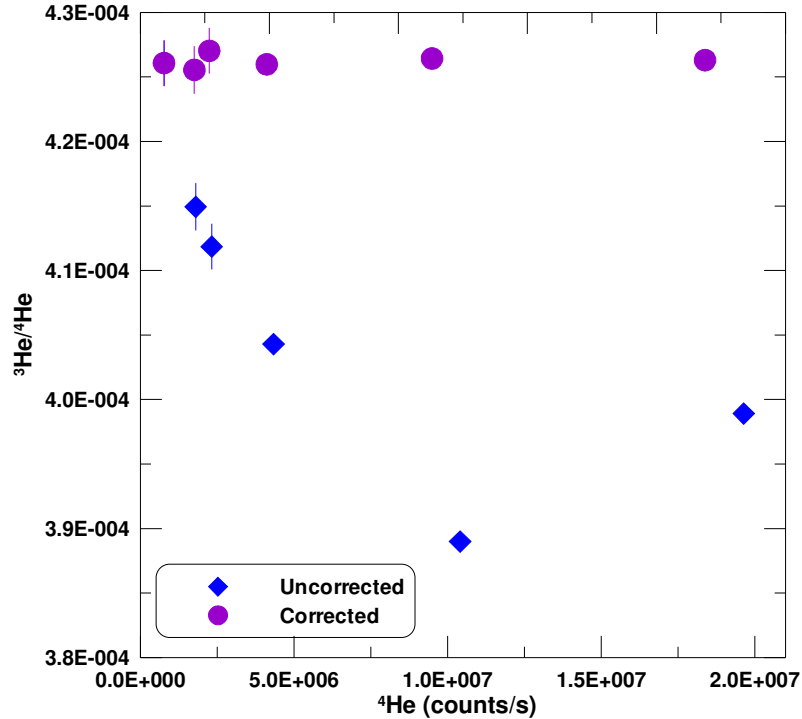


The helium data undergoes one additional step of processing. With only a single ion-counting multiplier detector, it is difficult to measure ion beams differing by 4 orders of magnitude, so in order to get reasonable precision for ^3He , it is necessary to have a very large amount of ^4He . When the count rates exceed 10^6 count/s (usually $\sim 10^{-7}$ torr if the species counted dominates), the sensitivity starts to change strongly with pressure

(Figure 2.9). Classical factors that contribute to undercounting at high count rates are generally due to the mechanics of counting itself, dead time effects and potentially counting artifacts due to ringing. When two ions hit the detector in time less than the pulse width, only one ion is counted, thus lowering the effective count rate. What dominates the loss of sensitivity in the GS-61 ion source shown in Figure 2.10, however, is not due to the mechanics of counting itself but space charge effects. This ion source was designed for extreme sensitivity and transmission. Essentially every ion that accelerates can be counted (nearly 100% source transmission) and a good peak shape is established by a low $\Delta V/V$, providing low velocity dispersion. This makes our two “conventional” mass spectrometers well-suited for measuring the low heavy abundance noble gases, as that was what it was designed to do. The low $\Delta V/V$ is achieved by having a very low extraction gradient for the voltage in the ionization region. The huge amounts of SW H, He and Ne extracted from these samples create a large density of ions in the source region since they are slow to extract given the small ΔV and large space-charge effects occur in the ionization region distorting the extraction field. This has two unwanted effects: it further reduces the extraction efficiency and thus the sensitivity, as shown in Figure 2.9, and it increases the time spent in the ionization region, increasing the probability for double ionization (increasing, for instance, the $\text{Ar}^{++}/\text{Ar}^+$ ratio). Although the reduction in sensitivity can be calibrated, the modification of the ion optics, which changes mass discrimination and the doubly-charged to singly charged ratio and thus changing most of the corrections we must make. This degrades the precision we can

obtain for the light noble gases He and Ne, but not for Ar since we have removed the abundant species that cause pressure effects.

Figure 2.10: The $^3\text{H}/^4\text{He}$ ratio versus amount of ^4He for P8b which was melted in one temperature step, and then repeatedly re-measured after removing some of the gas. The blue triangles are uncorrected measurements which vary widely because of high pressure effects. The purple circles are the data corrected using Equation 2.7.



It is difficult to separate out all of these different pressure effects and determine a correction for each one individually, so I instead determined a general effective high pressure correction. To figure out this correction, I melted three different PAC pieces (P16, P8b, and P04) in one step. Then after measuring the entire fraction ($\sim 10^7$ counts/s or $\sim 1.5 \times 10^{-6}$ torr of ^4He , well into the high pressure range), I repeatedly split the gas in half and re-measured what was left until it was well below the high pressure range ($\sim 10^5$ counts/s or 1.2×10^{-8} torr of ^4He). The high pressure fractions have widely varying

$^3\text{He}/^4\text{He}$ relative to the low pressure fractions, which can be seen for PAC sample P8b in Figure 2.10. I empirically determined a high-pressure correction which matched the high pressure ratios to the low pressure ratios. All He count rates were given an effective 2 ns deadtime correction, and then the isotopic ratios were corrected for high-pressure effects according to this formula:

$$\left(\frac{^3\text{He}}{^4\text{He}}\right)_{corrected} = 1.84 \times 10^{-5} \cdot \ln\left(\frac{^4\text{He}_{measured}}{^4\text{He}_0}\right) + \left(\frac{^3\text{He}}{^4\text{He}}\right)_{measured} \quad (2.7)$$

$^4\text{He}_0$ varies with the measured ^4He count rate according to:

$$^4\text{He}_0 = \begin{cases} 10^6 & \text{for } ^4\text{He}_{measured} < 3 \times 10^6 \\ 1.3 \times 10^6 & \text{for } 3 \times 10^6 < ^4\text{He}_{measured} < 10^7 \\ 3 \times 10^6 & \text{for } ^4\text{He}_{measured} > 10^7. \end{cases}$$

§ 2.4 Data and Analysis

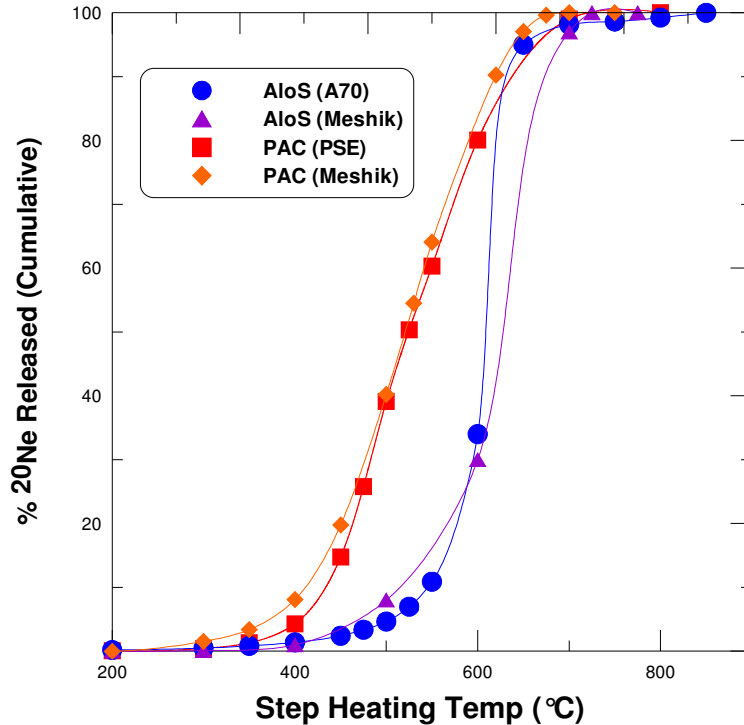
High-resolution step-wise heating analysis was performed on 6 AloS pieces and 5 PAC pieces; in addition, 3 PAC pieces were melted in one step and the gas was analyzed. See Table 2.4 for sample details and Appendix A for the full data sets for each sample.

§ 2.4.1 Release Profiles

First, Figure 2.11 compares temperature release profiles of ^{20}Ne from this work with the previously obtained profiles (Figure 2.3). We use this representation (cumulative release vs. extraction temperature) rather than a comparison of actual released amounts to compare samples of different sizes. The profiles agree very well even though they were measured on different mass spectrometers, several years apart, and using different

temperature steps. This confirms that the gas is released at a lower temperature from the PAC as compared to AloS. The subtle differences between release curves are probably due to slightly different thermal coupling of analyzed samples with the oven and/or small temperature bias between the heater and the sample housing (we actually control the heater temperature assuming perfect thermal shielding and black body geometry).

Figure 2.11: Release profile showing the percentage of ^{20}Ne released versus the step-wise heating temperature. This plot compares the release profiles ^{20}Ne from AloS and PAC measured using artificially implanted samples (Meshik et al. 2000) and those measured for this work (A70, PSE).



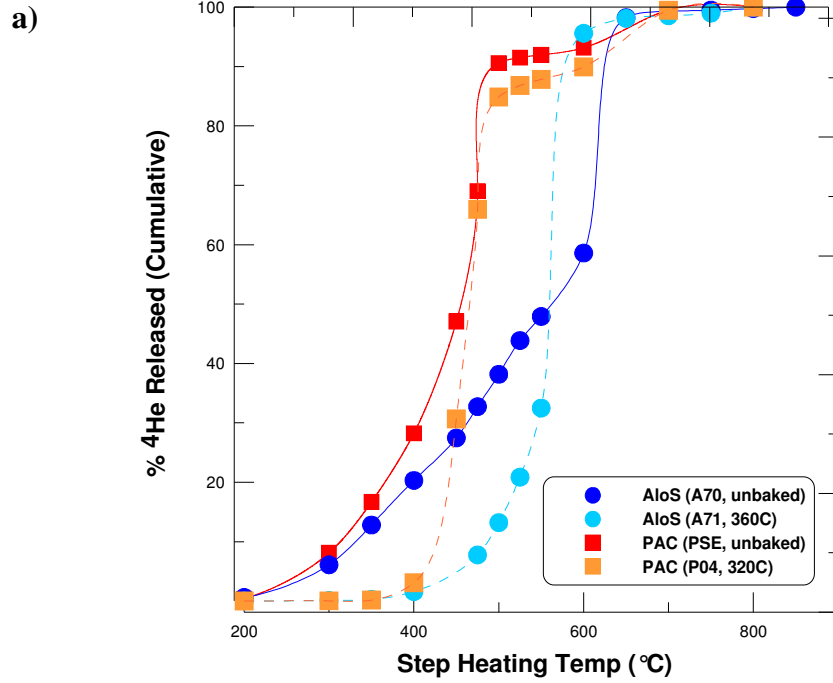
The temperature release profiles of ^4He , ^{20}Ne , and ^{36}Ar are shown in Figure 2.12. Each plot represents an unbaked reference sample of each material (AloS and PAC) and a sample that was baked at a high temperature for each material. There are several common features in the profiles of all three gases. First, the gases release at lower (step-wise

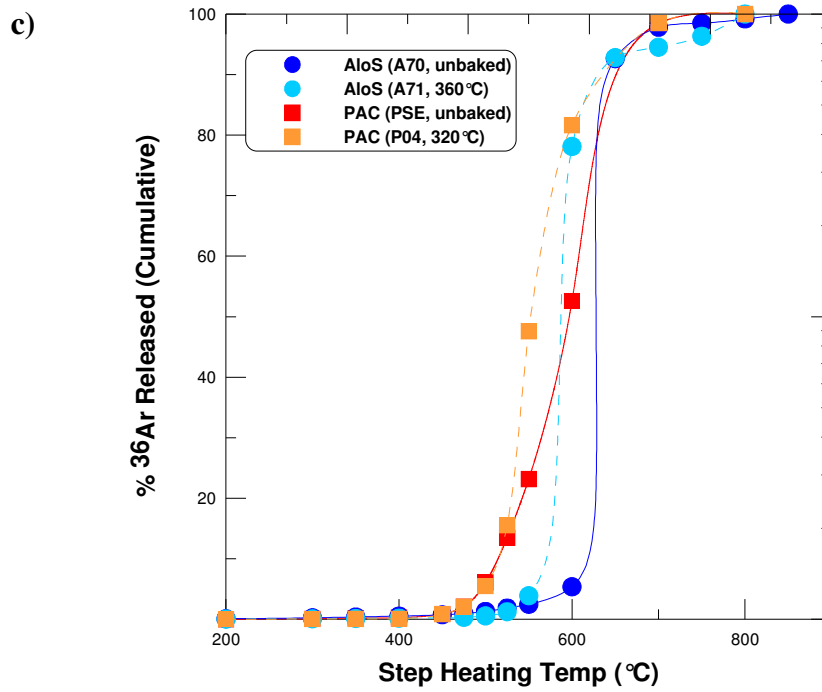
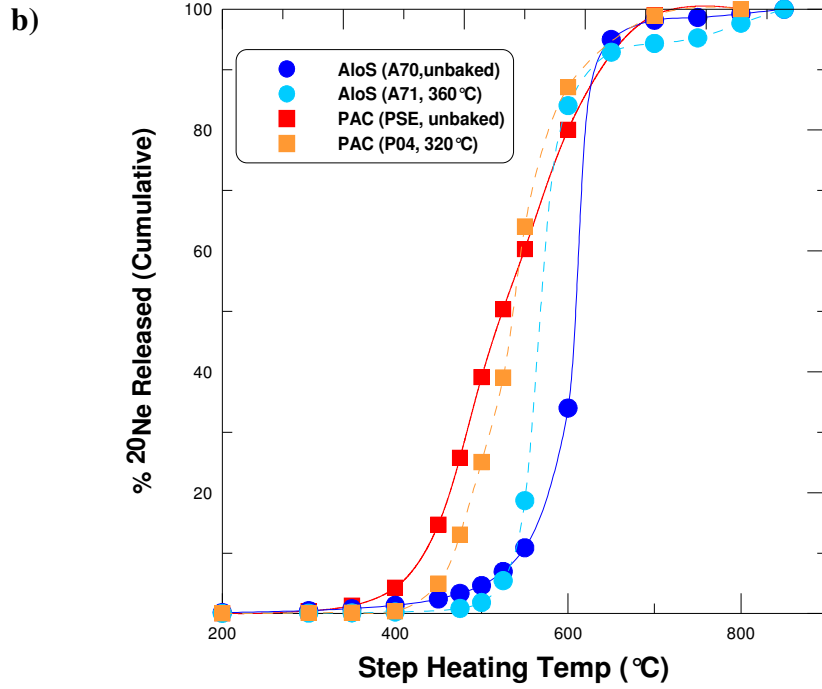
heating) temperatures from the PAC than from the AloS in all cases for similar bake temperature.

And second, it is clear that baking has an effect. In all cases the baked samples release SW-gases at higher temperatures than the unbaked sample of the same material. This effect is particularly strong for helium with 20% of ^4He released from the baked sample versus 1.5% for the unbaked sample, and a split of 28% to 3% for PAC. Although, the effect is less noticeable for ^{20}Ne and ^{36}Ar , it works in the same direction. This is because the near-surface region of the baked samples has already been depleted in gases from diffusive losses during the long-term bake and therefore higher temperatures are needed before comparable amounts of gas are released relative to the unbaked samples.

The reason why gases are released at lower temperatures from PAC compared to AloS most likely has to do with their different crystal structures. The Al-film of the AloS is more amorphous compared to the PAC, AloS evidently traps gases better, since there may be fewer direct escape paths along grain boundaries. The T6-6061 Al alloy that the PAC is made from also has a somewhat lower melting point than the pure Al (see Table 1.1) so possibly the crystalline structure begins changing at lower temperatures allowing gases to escape more easily. But the main point is that PAC has thermal properties that are different from AloS.

Figure 2.12: Temperature release profiles for ^4He (a), ^{20}Ne (b), and ^{36}Ar (c) for AloS and PAC. The x-axis temperature refers to the step-wise heating temperature and the y-axis shows the cumulative release of the gas in %. The temperature referred to in the legend is the long-term bake temperature of that sample.



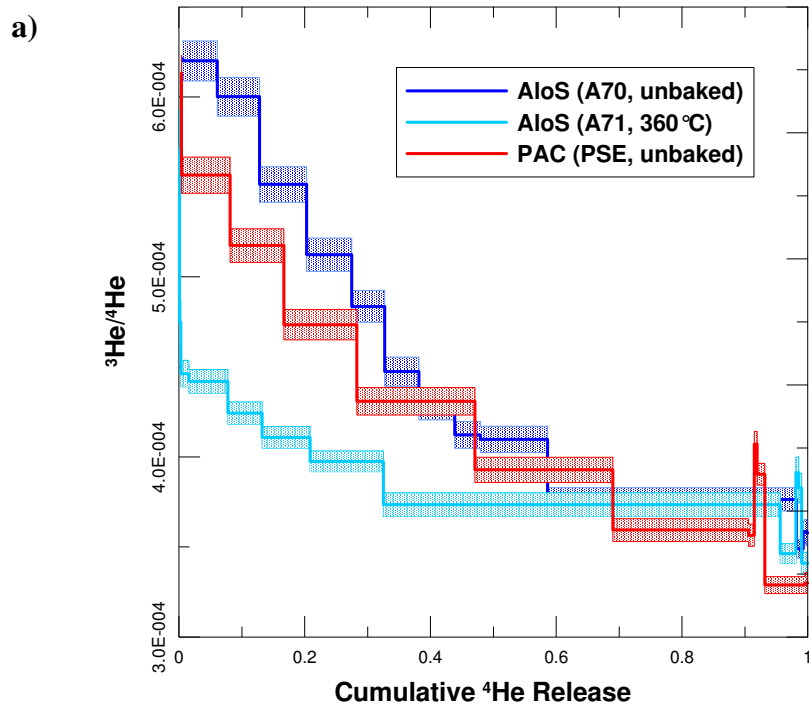


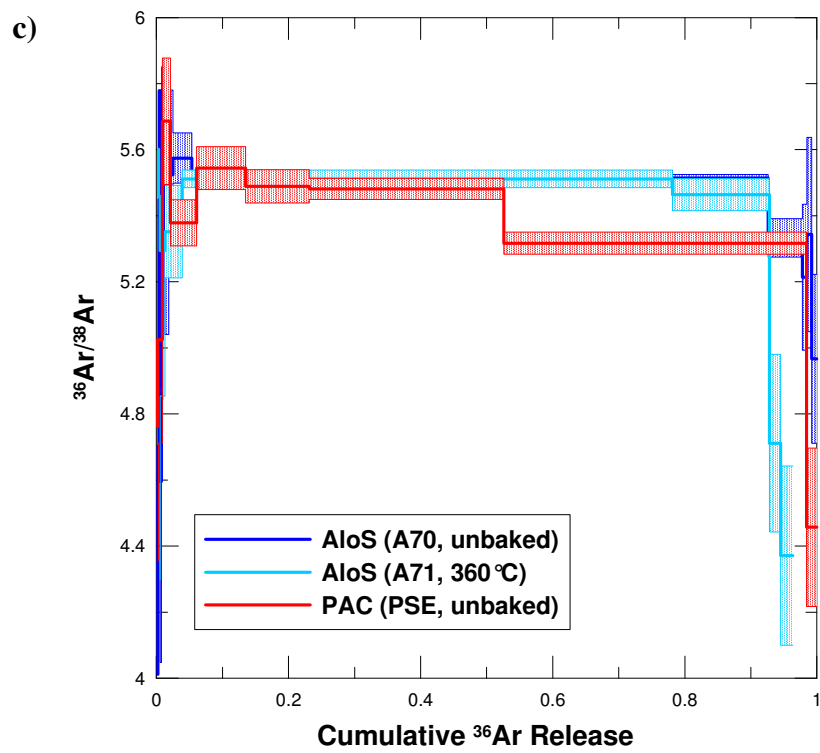
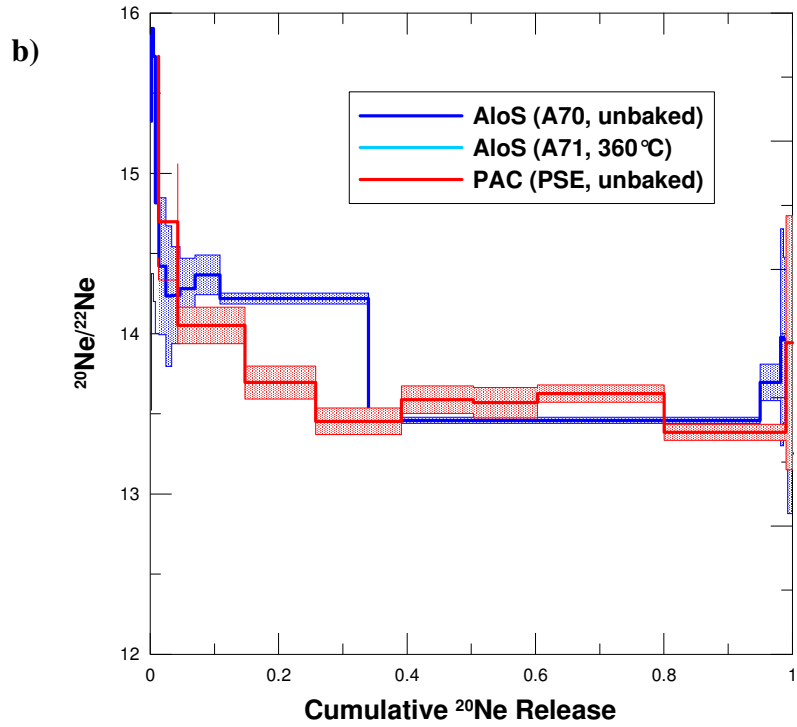
The isotopic ratio vs. extraction temperature shown in Figure 2.13 are not true depth profiles though they are depth-dependant. Now comparing the PAC and AloS in Figure

2.13, we notice that there is again a clear difference between the two materials. The profiles of the PAC pieces are consistently isotopically heavier than the A1oS, although they both show a fairly linear decrease in isotopic ratio as the He gas is released. The depth dependence is much less pronounced for Ne and even less for Ar. This is expected because the relative mass difference between isotopes decreases with increased mass and the lighter species are the more mobile.

The effect of baking is dramatic for He, slight for Ne, and not significant at all for Ar. Helium isotopic ratios are consistently heavier, especially in the early steps. This is also true for neon, but not as severely. The baked and unbaked A1oS Ar profiles are virtually identical.

Figure 2.13: Step-wise release plots, temperatures on the lines refer to step-wise temperature of the largest release step.



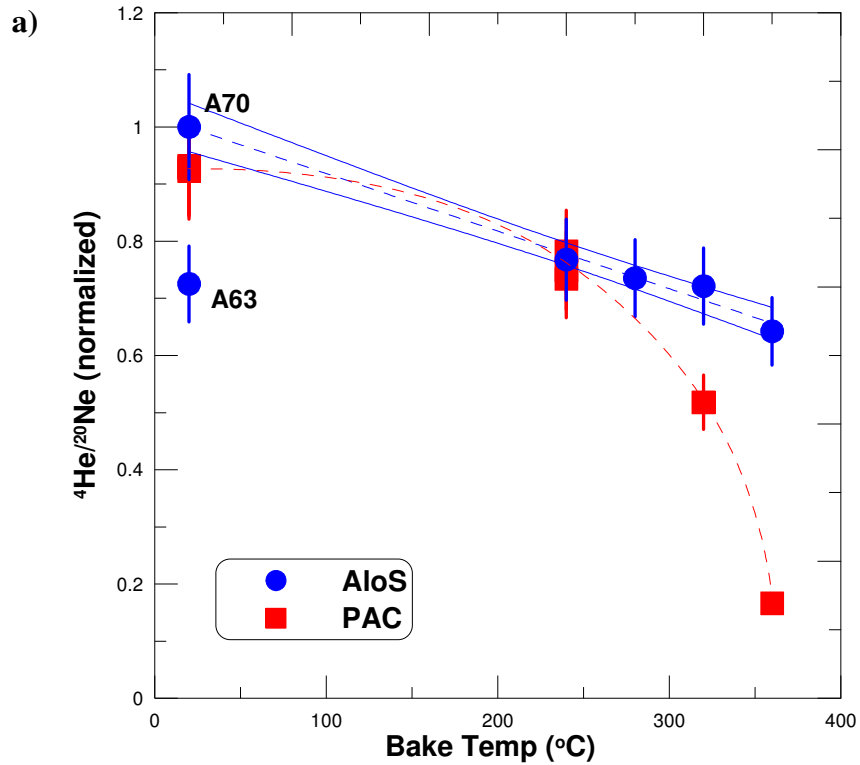


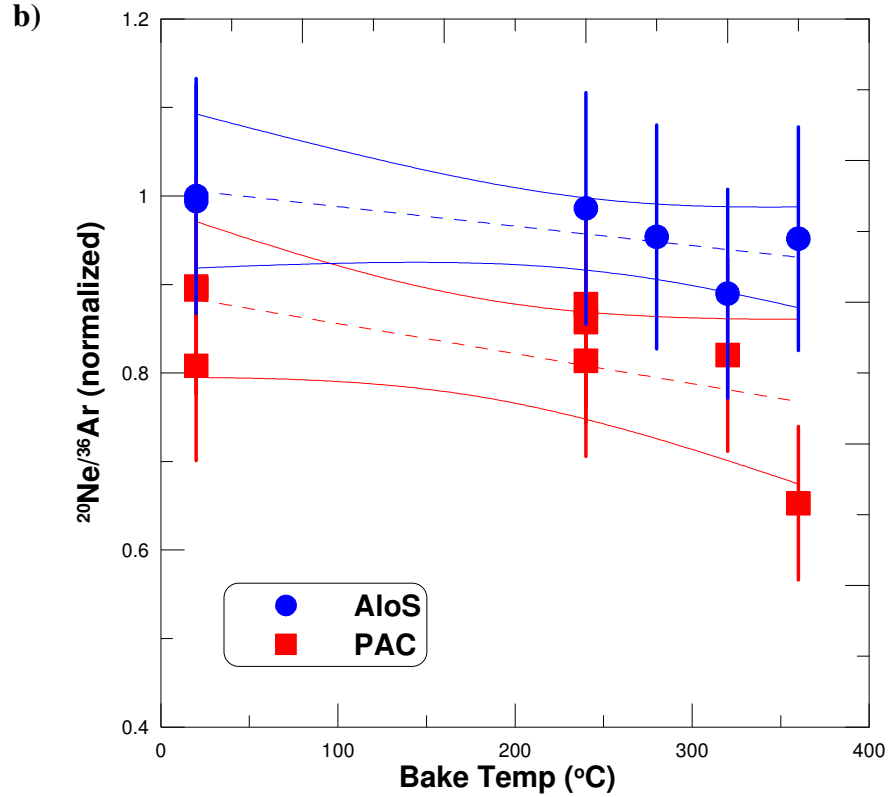
§ 2.4.2 Elemental ratios and amounts

The values discussed in this and the following sections refers to the bulk results for each sample, which is the sum of the data for all step-wise heating steps and the temperatures used refer to the long-term bake temperature in the course of our diffusion experiment, not the step-wise heating temperature.

The elemental ratios ${}^4\text{He}/{}^{20}\text{Ne}$ and ${}^{20}\text{Ne}/{}^{36}\text{Ar}$ ratios are show below in Figure 2.14 and the values are given in Table 2. 7. The ratios are all normalized to the ratio of unbaked AloS, A70. In Figure 2.12a, one can see that ${}^4\text{He}/{}^{20}\text{Ne}$ is getting heavier for higher temperatures for both collectors, suggesting that more He then Ne has been lost to diffusion. The ratio decreases by between 20 and 40% for AloS relative to the unbaked sample, and over 80% for the highest baked PAC sample. Figure 2.12b shows ${}^{20}\text{Ne}/{}^{36}\text{Ar}$ for which there is no measurable change for AloS. The lower temperature baked PAC are all heavier than the AloS, although they are all also within 1σ except for the highest baked sample, which does appear to show measurable loss of neon relative to argon.

Figure 2.14: ${}^4\text{He}/{}^{20}\text{Ne}$ (a) and ${}^{20}\text{Ne}/{}^{36}\text{Ar}$ (b) elemental ratios, all are normalized to the unbaked reference sample A70. Sample A63 was also unbaked but badly scratched compared to A70. Linear fits with 95% confidence levels are shown for all except for the PAC ${}^4\text{He}/{}^{20}\text{Ne}$ ratio which does not appear to be linear. Errors are 2σ statistical.





Incoming SW ions have some chance of scattering off the aluminum target instead of being implanted, with the lighter isotopes being more likely to scatter backwards than the heavier isotopes. For He, a backscattering correction is required. The correction factors found using TRIM (Ziegler 2004) software are shown in Table 2.9. For a light target like Al, the Ne and Ar backscatter corrections are negligible.

Table 2.9: Helium backscatter correction factors for an aluminum target, calculated using TRIM (Ziegler 2004).

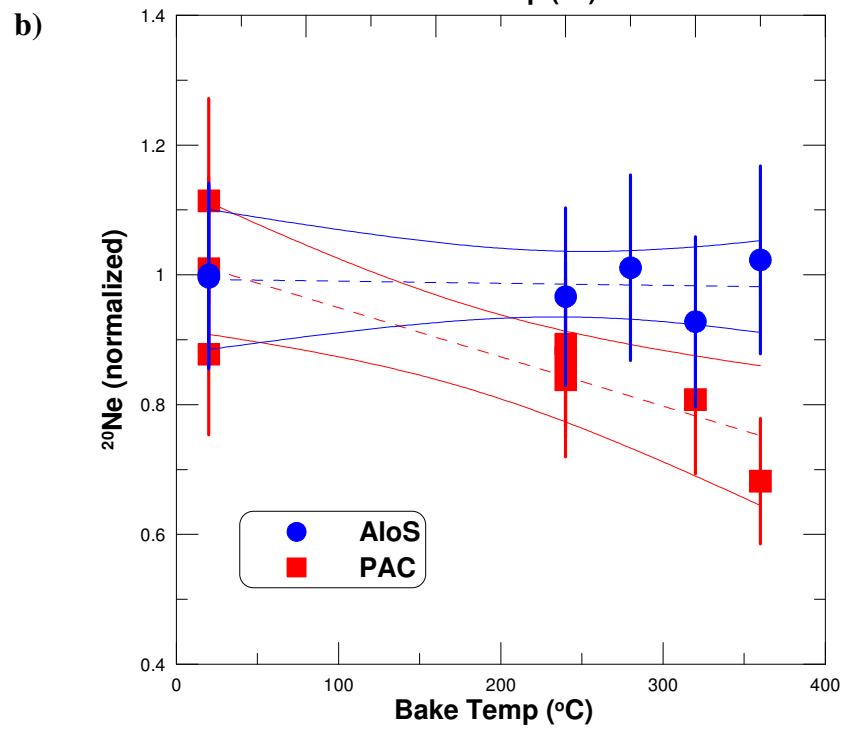
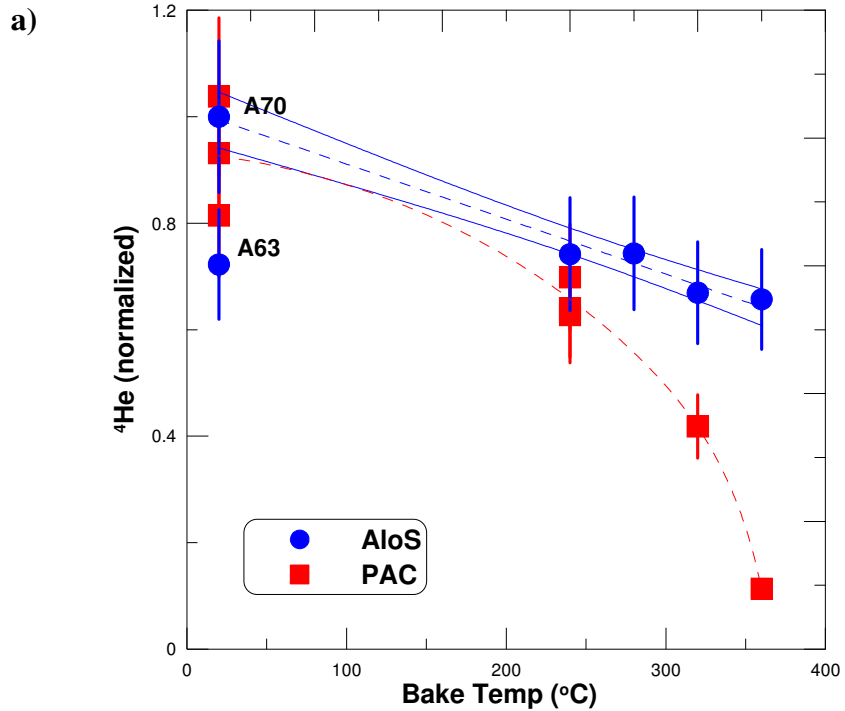
SW Regime	³ He correction	⁴ He correction	³ He/ ⁴ He correction
Bulk	0.930	0.943	0.98640
CME	0.925	0.938	0.98615
Fast (H)	0.947	0.958	0.98775
Slow (L)	0.914	0.927	0.98594

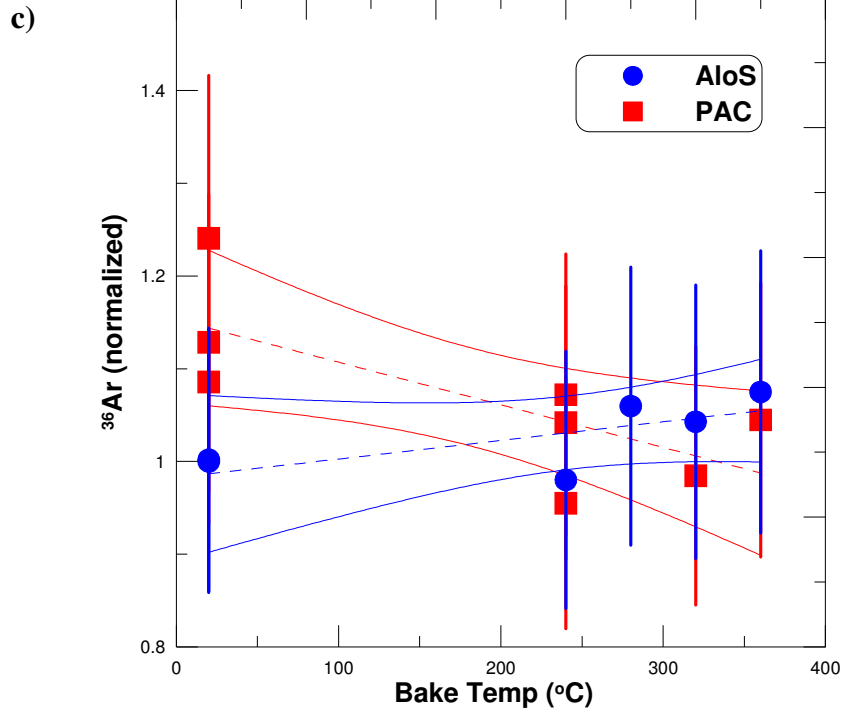
Table 2.10: Elemental fluxes (in atoms) and elemental ratios. He is corrected for backscattering. Errors (in parentheses) are 2σ statistical.

Sample	Bake Temp	^4He ($\times 10^{10}/\text{m}^2\cdot\text{s}$)	^{20}Ne ($\times 10^8/\text{m}^2\cdot\text{s}$)	^{36}Ar ($\times 10^6/\text{m}^2\cdot\text{s}$)	$^4\text{He}/^{20}\text{Ne}$	$^{20}\text{Ne}/^{36}\text{Ar}$
A70	unbaked	10.4 (1.0)	1.7 (0.2)	2.7 (0.3)	596 (39)	64 (6)
A63	unbaked	7.5 (0.8)	1.7 (0.2)	2.7 (0.3)	433 (28)	64 (6)
A67	240	7.7 (0.8)	1.7 (0.2)	2.6 (0.3)	458 (30)	63 (6)
A66	280	7.7 (0.8)	1.8 (0.2)	2.9 (0.3)	439 (28)	61 (6)
A68	320	7.0 (0.8)	1.6 (0.2)	2.8 (0.3)	430 (28)	57 (5)
A71	360	6.9 (0.7)	1.8 (0.2)	2.9 (0.3)	383 (25)	61 (6)
PNE	unbaked	10.8 (1.0)	1.9 (0.2)	3.3 (0.3)	556 (36)	58 (5)
PSE	unbaked	9.7 (1.0)	1.8 (0.2)	3.0 (0.3)	550 (36)	58 (5)
P7b	240	7.3 (0.7)	1.6 (0.2)	2.8 (0.3)	467 (30)	55 (5)
P7a	240	6.5 (0.7)	1.5 (0.2)	2.6 (0.3)	447 (29)	56 (5)
P04	320	4.4 (0.4)	1.4 (0.2)	2.7 (0.3)	309 (20)	53 (5)
P16	unbaked	8.5 (0.8)	1.5 (0.2)	2.9 (0.3)	554 (35)	52 (5)
P8b	240	6.7 (0.7)	1.5 (0.2)	2.9 (0.3)	438 (29)	52 (5)
P02	360	1.2 (0.1)	1.2 (0.2)	2.8 (0.3)	99 (7)	42 (4)

Figure 2.15 shows the relative amounts of SW fluences, which are normalized to those in unbaked AloS A70. These values are dependent on the area of the sample (see Table 2.4) which we only can determine to about 10% for these small areas. But here again we see a similar pattern, there clearly are losses of ^4He (Figure 2.15a) from both collectors, up to 35% losses from AloS at the highest temperature to almost 90% from the PAC relative to unbaked samples. The ^{20}Ne (Figure 2.15b) from the AloS does not show any statistically significant losses, but the PAC does have a slight downward trend with the highest temperature showing losses beyond 2σ . And for ^{36}Ar (Figure 2.15c) there are no detectable losses for either collector material.

Figure 2.15: ^4He (a), ^{20}Ne (b), and ^{36}Ar (c) amounts normalized to A70. Linear fits with 95% confidence levels are shown for all except for the PAC $^3\text{He}/^4\text{He}$ ratio which does not appear to be linear. Errors are 2σ statistical.





§ 2.4.3 Isotopic Ratios

For the purposes of the Genesis mission, determining if there are changes to the isotopic ratios among different SW regimes is clearly a priority, so changes due to the material must be evaluated. It is not unexpected that samples heated to a high enough temperature will lose some gas from diffusion, but it is not immediately clear if such losses are important for these collectors, and whether such losses can alter isotopic ratios.

Table 2.11: Bulk isotopic ratios of He, Ne, and Ar in AloS and PAC after prolonged baking. $^3\text{He}/^4\text{He}$ are corrected for backscattering. Errors are 1σ statistical.

Sample	Bake Temp (°C)	$^3\text{He}/^4\text{He}$ ($\times 10^{-4}$)	$^{20}\text{Ne}/^{22}\text{Ne}$	$^{21}\text{Ne}/^{20}\text{Ne}$ ($\times 10^{-3}$)	$^{36}\text{Ar}/^{38}\text{Ar}$
A70	unbaked	4.462 ± 0.048	13.746 ± 0.025	$2.392 \pm .011$	5.496 ± 0.012
A63	unbaked	4.075 ± 0.051	13.720 ± 0.034	$2.418 \pm .018$	5.503 ± 0.019
A67	240	4.084 ± 0.057	13.786 ± 0.028	$2.383 \pm .012$	5.509 ± 0.016
A66	280	4.007 ± 0.049	13.658 ± 0.019	$2.389 \pm .010$	5.503 ± 0.013
A68	320	3.948 ± 0.055	13.684 ± 0.030	$2.387 \pm .014$	5.519 ± 0.018
A71	360	3.860 ± 0.045	13.600 ± 0.036	$2.405 \pm .018$	5.493 ± 0.034
PNE	unbaked	4.189 ± 0.049	13.661 ± 0.057	$2.445 \pm .018$	5.39 ± 0.027
PSE	unbaked	4.216 ± 0.050	13.669 ± 0.032	$2.394 \pm .014$	5.403 ± 0.021
P7b	240	3.769 ± 0.047	13.578 ± 0.029	$2.395 \pm .014$	5.464 ± 0.021
P7a	240	3.760 ± 0.049	13.584 ± 0.033	$2.401 \pm .014$	5.504 ± 0.021
P04	320	3.765 ± 0.049	13.564 ± 0.016	$2.403 \pm .009$	5.405 ± 0.015
P16	unbaked	4.175 ± 0.059	13.637 ± 0.023	$2.376 \pm .012$	5.408 ± 0.018
P8b	240	3.907 ± 0.067	13.598 ± 0.025	$2.388 \pm .015$	5.437 ± 0.024
P02	360	3.480 ± 0.069	13.508 ± 0.022	$2.408 \pm .012$	5.381 ± 0.014

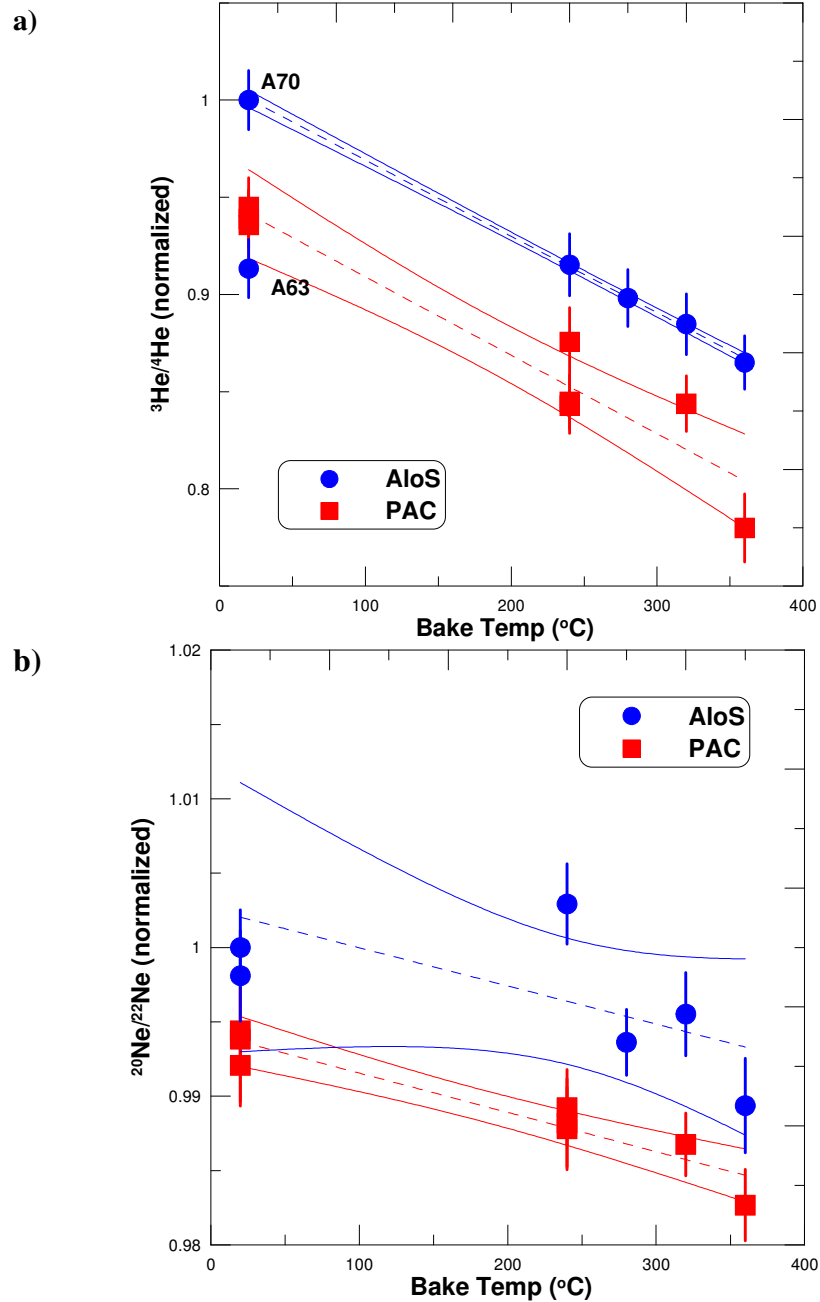
The bulk isotopic ratios for each sample are given in Table 2.11 and the normalized ratios are plotted in Figure 2.16. The $^3\text{He}/^4\text{He}$ (Figure 2.14a) is definitely affected by the diffusive losses due to baking. For AloS, the 240 °C sample is about 8% heavier than the unbaked sample and this difference is beyond 2σ ; the 360 °C sample got up to 13% isotopically heavier relative to the unbaked sample. The $^3\text{He}/^4\text{He}$ in PAC is isotopically heavier than AloS at every bake temperature, even in the unbaked samples and the ratio at the highest bake temperature is 16% lower than the unbaked PAC.

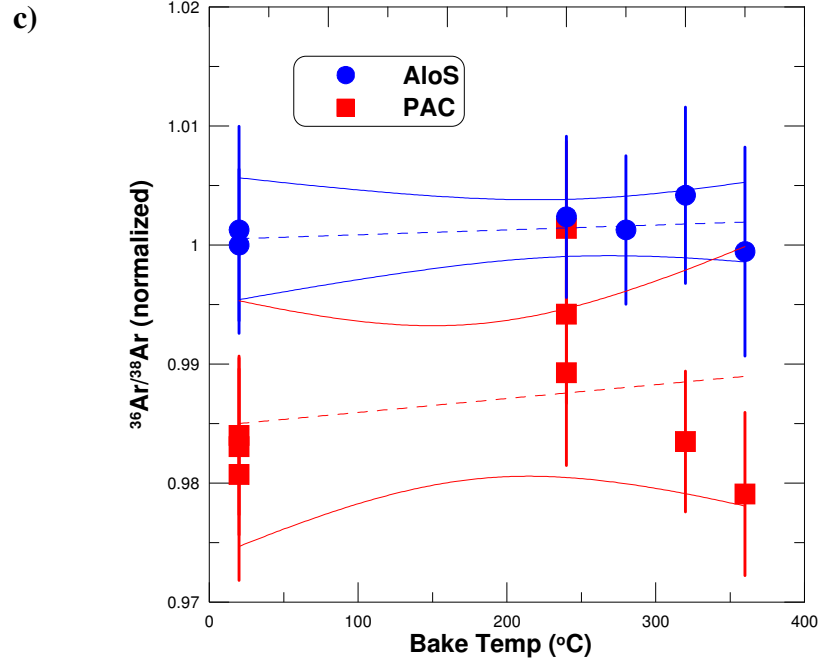
The two unbaked AloS pieces, A70 and A63, evidently differ in $^4\text{He}/^{20}\text{Ne}$ (Figure 2.14) and $^3\text{He}/^4\text{He}$ (Figure 2.16). Images of the two pieces (Figure 2.5) show that A63 is significantly more scratched than A70. Neither of these ratios depends on the areas, so the issue cannot be simply that the area was measured incorrectly. I speculate that the shallowest (sub-micron) scratches and abrasions on A63 caused a depth-dependent loss of material, with more being lost near the surface than deeper down. This would lead to higher losses of lighter gases (more shallowly implanted) and therefore heavier measured ratios.

All of the $^{20}\text{Ne}/^{22}\text{Ne}$ in AloS are within 1σ of each other except for the highest baked sample which is about 1% lower than the unbaked. Gases released from the PAC are again all slightly isotopically heavier ($\sim 0.5\%$) than AloS, and also decrease with increased bake temperature up to 1% relative to the unbaked PAC, suggesting that diffusive losses affect the AloS much less than the PAC.

The $^{36}\text{Ar}/^{38}\text{Ar}$ in AloS is the same for all samples regardless of bake temperature with differences much less than 1σ . Additionally, all of the PAC ratios agree with each other except for one the 240 °C samples, although it is unclear why gases from this piece (all measured at different times) would be isotopically lighter than the others. It is also not clear why the average $^{36}\text{Ar}/^{38}\text{Ar}$ in PAC is $\sim 1.5\%$ lower than the average AloS ratio, given that the average difference between AloS and PAC is only $\sim 0.5\%$ for $^{20}\text{Ne}/^{22}\text{Ne}$. The effect of a mass-dependent process such as diffusion should decrease as the relative difference between the masses gets smaller.

Figure 2.16: Isotopic ratios $^3\text{He}/^4\text{He}$ (a) $^{20}\text{Ne}/^{22}\text{Ne}$ (b) and $^{36}\text{Ar}/^{38}\text{Ar}$ (c). All are normalized to unbaked AloS A70. Linear fits with 95% confidence levels are shown for all. Errors are 1σ statistical.





§ 2.4.4 Diffusion properties of Genesis Al collectors

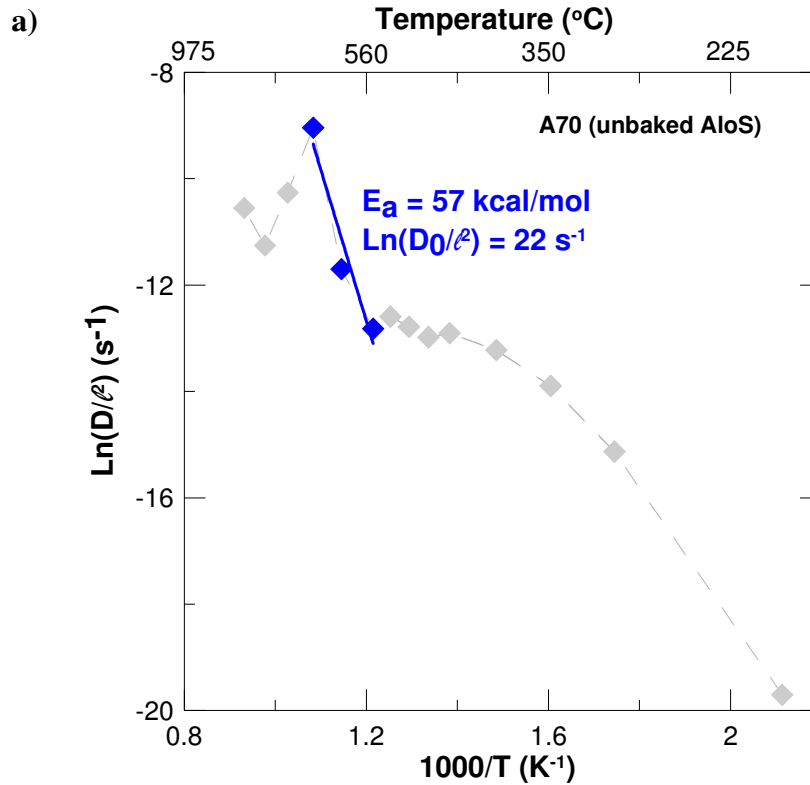
The goals of this experiment are to determine (1) if PAC is a suitable collector material for light noble gases and (2) if there could have been measurable diffusive losses from either collector during the Genesis mission and to quantitatively estimate these changes if they did occur. Addressing the first goal, we saw in the previous section that the isotopic and elemental composition of gases from the PAC are consistently heavier and that diffusive losses are substantially greater for PAC than AloS, suggesting that PAC is not suitable for measuring the light gases (but it should be an acceptable collector for heavier gases). One final check of the PAC is to compare the diffusion properties based on step-wise heating of both collectors in order to better characterize noble gas mobility in these two materials.

Calculating the diffusion coefficients from the step-wise heating data requires several assumptions and approximations. Using the equations from Table 2.2, we are assuming a uniform distribution of gas within in the sample, which is a very a gross approximation in the case of the Genesis samples. We further assume that the temperature of the sample was equal to the temperature of the oven for each step, which may not be true if the sample did not reach thermal equilibrium with the oven. Nevertheless, within these limitations, diffusion data for these two different collector materials can be compared and the calculated diffusion coefficients can be found in Appendix B. In Figure 2.17 is shown the resulting Arrhenius plots for 2 samples, A70 and PSE.

Although there are several unjustified assumptions and approximations involved in this calculation, that may cast doubt on their absolute accuracy, it is still possible to make some general comparisons. The Arrhenius plots are fairly linear at the steps corresponding to the major release of SW gas from the sample, and so it is possible to obtain values for the activation energy (E_a) and the frequency factor (D_0) from the equation of the line. The average values of E_a and D_0 for each element and collector material are shown in Table 2.12. Some of the PAC samples have a smaller second release of SW gases after the major release, as can be seen in Figure 2.17b, but the values given in Table 2.12 come from the larger gas release. Again, although these values may be subject to limitations inherit to the assumptions made, it is true for each gas that the activation energy is higher for AloS than for PAC, consistent with all previous observations indicating that the PAC is less retentive than AloS. Also, for both collectors,

the activation energy increases for heavier gases, which is consistent with a diffusive loss mechanism.

Figure 2.17: Approximate diffusion coefficients were calculated by assuming a uniform distribution of gas leading to the following Arrhenius plots for ^4He of unbaked samples of each material, a) A1oS and b) PAC. The lines were fit to the points corresponding to the major release of SW ^4He from the samples. Light grey points do not belong to the major gas release and were not taken into account in calculation of the activation energy. a) Most of the SW ^4He released from A1oS in just three temperature steps which are shown in blue. b) The release of SW ^4He from PAC was spread out over more temperature steps than the A1oS. The majority of the gas was released in the steps corresponding to the red points, and there was a second peak in the gas release from PAC shown with the green points.



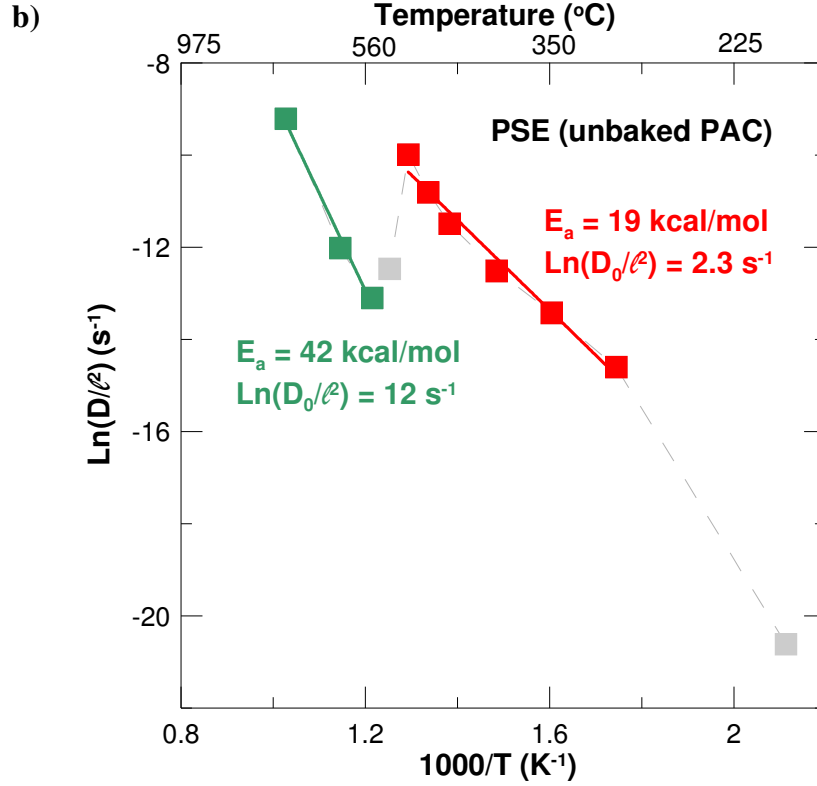


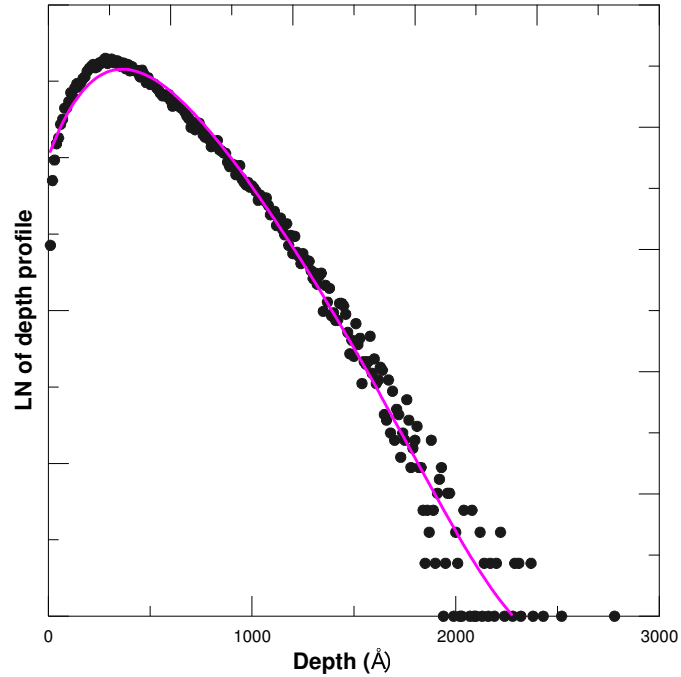
Table 2.12: Average activation energy (E_a) and frequency factor (D_0) from a linear fit to an Arrhenius plot using the steps corresponding to the major gas release from the sample. Errors were calculated by standard deviation.

Bake Temp (°C)	Sample	⁴ He		²⁰ Ne		³⁶ Ar	
		E_a (kcal/mol)	$\text{Ln}(D_0/\ell^2) (\text{s}^{-1})$	E_a (kcal/mol)	$\text{Ln}(D_0/\ell^2) (\text{s}^{-1})$	E_a (kcal/mol)	$\text{Ln}(D_0/\ell^2) (\text{s}^{-1})$
unbaked	A70	57	22	74	31	127	59
unbaked	A63	40	13	72	30	87	36
240	A67	46	15	50	17	121	53
280	A66	39	13	73	32	118	59
320	A68	43	14	76	32	106	48
360	A71	48	18	102	49	143	72
Average		45 ± 7	16 ± 3	75 ± 17	32 ± 10	117 ± 19	55 ± 12
unbaked	PSE	19	2	27	5	57	21
unbaked	PNE	17	1	33	8	55	21
240	P7a	38	15	44	16	73	33
240	P7b	47	21	45	16	83	38
320	P04	28	6	38	12	80	37
Average		30 ± 12	9 ± 9	37 ± 7	12 ± 5	70 ± 13	30 ± 9

To address the second goal of quantifying possible diffusive losses under the conditions of the Genesis mission, I will now look at the diffusion parameters for AloS of the long-term bake as opposed to the step-wise heating. By doing this we can avoid many of the approximations and assumptions needed for the step-wise heating calculations such as uniform gas distribution in the sample and extrapolating from the very different time scales of the laboratory step-wise heating (~45 minutes) and the Genesis mission (~2 years).

For these calculations, we need a better approximation of the initial concentration profile, $C(x, 0)$. This is found by fitting the TRIM profile described above in § 2.1.1, by taking the first natural log of the original profile and then fitting a fifth order polynomial (Figure 2.18). This gives $C(x, 0)$ as an equation of the form: $e^{A+Bx+Cx^2+Dx^3+Fx^4+Gx^5}$.

Figure 2.18: Natural log of the TRIM calculated implantation depth profile of ^4He (black points) with a 5th order polynomial fit (pink line).



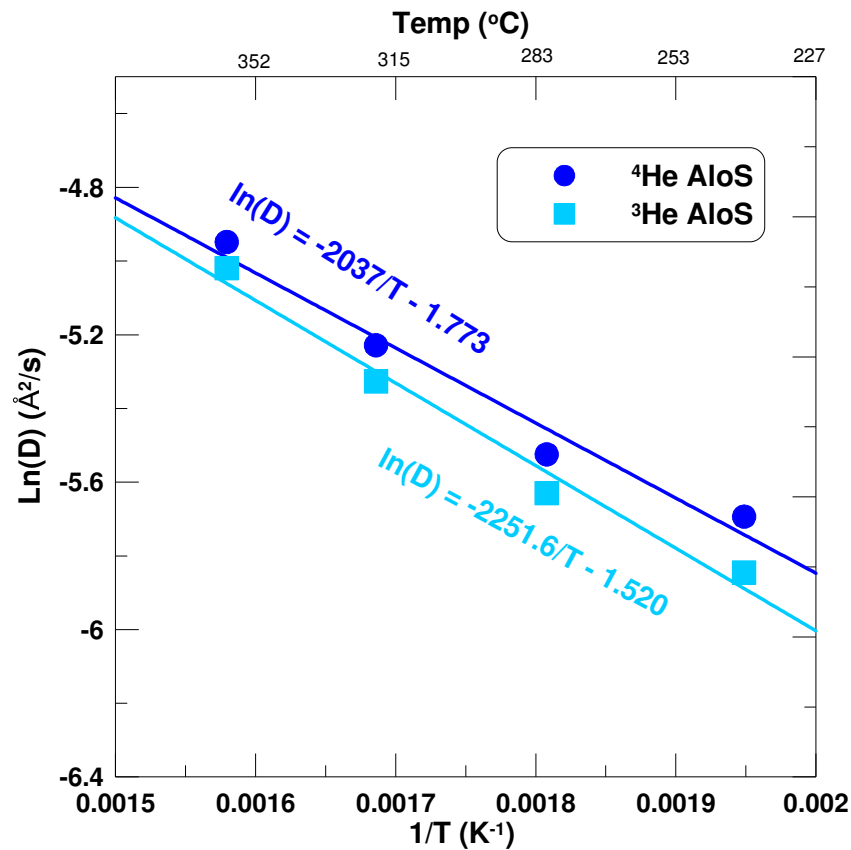
Then we need to calculate the diffusion coefficients of the gases in these materials and produce an Arrhenius plot. The fractional loss is calculated relative to the unbaked sample, these values are shown in Table 2.13. For AloS I have used just A70 for the unbaked reference sample since A63 seems to have unquantified losses due to scratches.

Table 2.13: Fractional loss of ^4He from AloS samples (relative to A70).

File	Temp (°C)	^4He fractional loss	^3He fractional loss
A67	240	0.2510	0.3144
A66	280	0.2764	0.3501
A68	320	0.3247	0.4027
A71	360	0.3745	0.4579

Next the diffusion coefficients can be calculated by using the fractional losses (f) and Equation 2.6. The diffusion coefficients obey the Arrhenius equation, $D = D_0 e^{\frac{-E_a}{RT}}$, where D is the diffusion coefficient, D_0 is the frequency factor, E_a is the activation energy, T is the absolute temperature, and R is the gas constant. Plotting D versus T^{-1} allows one to fit a straight line to the points, and the equation of this line can be used to calculate the diffusion coefficient for any temperature. The Arrhenius plot is shown for ^3He and ^4He in Figure 2.19. For ^3He $E_a = 4.5$ kcal/mol and $\text{Ln}(D_0/\ell^2) = -3.71 \text{ s}^{-1}$; for ^4He $E_a = 4.1$ kcal/mol and $\text{Ln}(D_0/\ell^2) = -3.97 \text{ s}^{-1}$. These activation energies are about an order of magnitude lower than those calculated from the step wise heating data (Table 2.12), and the frequency factors are substantially lower as well. This implies that a different mechanism is at work leading to long-term low level losses due to melting of the samples during step wise heating, and therefore that it is not valid in this case to use step wise heating data to ‘scale up’ to long-term losses. Additionally, it must be noted that the activation energy for ^3He is higher than for ^4He which is not expected since ^3He is lighter and therefore diffuses easier. These numbers arise mathematically (even though there are greater losses of ^3He as expected) because of the different implantation profiles of the two gases. This may mean that the modeled implantation profiles are not quite correct.

Figure 2.19: Arrhenius plot for ^3He and ^4He in AloS based on the fractional loss of gas during the long-term bake.



Using the equations of the lines shown in Figure 2.15, it is possible to calculate the diffusion coefficients for different temperatures. Unfortunately, we do not know exactly the temperature of the collectors during SW collection, as there were no temperature sensors for the collectors. The temperature of the collectors during their exposure to the SW has been estimated in two ways: 1) calculating the temperature based on the optical properties of the material and 2) by measuring the temperature of the collector during the thermal vacuum test of the engineering model (Jurewicz et al. 2003). For AloS, the calculated temperature is around 260 °C, but the engineering test temperature was half

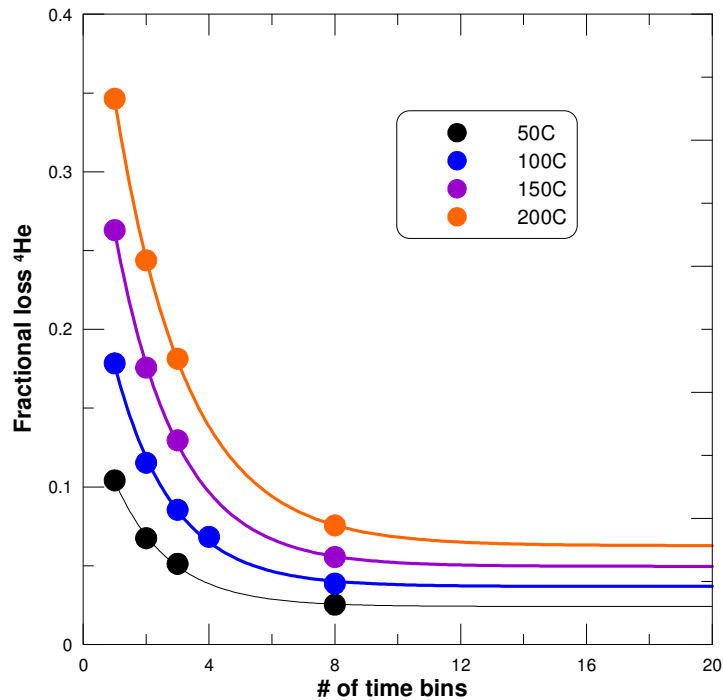
that value: 130 °C. So it seems a reasonable assumption that, during the flight of the Genesis mission, the AloS target was at a temperature between 50 °C and 300 °C. I would place more confidence in the experimental estimate and suggest that the most likely equilibrium temperature was between 100 °C and 150 °C. The situation for PAC is even less clear. The optical properties of the material would have been altered by the polishing, and it was not part of the thermal vacuum test. It very likely was not at the same temperature as the AloS, but the 50 °C and 300 °C range should still apply.

There is one final complication, in order to estimate the losses that occurred during the Genesis mission, one should account for the fact that throughout that entire time, gas is being implanted in the sample at the same time that it is diffusing out. Therefore, it is not correct to calculate the fractional loss by plugging in $D(T)$ and time into Equation 2.6. I used the procedure listed below to take into account simultaneous implantation and diffusion losses of SW ions. All of these calculations were done using Mathematica; the files used are reproduced in Appendix C.

1. Use the equation of the line determine in Figure 2.19 to calculate $D(T)$ for chosen T .
2. Divide total time of Genesis mission into ‘bins’ (from 1 to 8).
3. Using $t = \text{total time}/\#\text{bins}$ and $\ell = 3000 \text{ \AA}$ (thickness of the Al-film), calculate $D \cdot t / \ell^2$ and plug into Equation 2.6 to get the fractional loss.
4. For more than 1 bin, use this $D \cdot t / \ell^2$ to calculate how the implantation profile is altered.

5. Do a fit to the new profile the same way as the original; this is now the profile for the next time bin.
6. Repeat for all bins, then calculate the total fractional loss from the fractional loss for each time bin.
7. Plot (Figure 2.20) the total fractional losses for each vs. the number of time bins and extrapolate to an infinite number of bins. This is the expected fractional loss for the duration of the Genesis mission for that particular temperature.

Figure 2.20: The calculated fractional loss of ^4He from AloS for different temperatures versus the number of divisions of the total SW exposure time ('time bins'), see text for explanation. The points are fit by an exponential curve that gives the fractional loss for infinite time bins.



The results of these calculations are shown below in Table 2.14. The amount of He lost from AloS at 100 to 150 °C is around 4 – 5%, with less than a 1% change in the

isotopic ratio of the remaining gas. Both of these values are comparable to the level of precision which these values can be measured. Therefore, unless the equilibrium temperature was higher than expected ($> 300\text{ }^{\circ}\text{C}$), these losses will not significantly alter the measured values. The effect would be even smaller, and therefore negligible for Ne and Ar.

Table 2.14: Calculated loss estimates of helium from AloS for the time of the Genesis mission at various temperatures.

Temperature ($^{\circ}\text{C}$)	^4He loss (%)	$^3\text{He}/^4\text{He}$ (% decreased)
50	2.4	0.16
100	3.7	0.29
150	5.0	0.66
200	6.3	0.74
300	8.8	1.1

Chapter 3 : Solar Wind Regimes

§ 3.1 Collection of Bulk and Solar Wind Regimes

One of the main goals of the Genesis mission was to collect separate samples of the different types of solar wind (regimes) in addition to the bulk (average) solar wind. An introduction was given in § 1.2.1. This was accomplished by having 5 separate arrays of collectors. These measurements were done using one of the collectors (AloS) from these regime arrays. Helium and neon isotopes in the different regimes were measured by Alex Meshik and Yves Marrocchi in 2005 and 2006; argon isotopes were measured by Alex Meshik and myself in 2007. I will only be reporting neon and argon results here since there are still some unresolved issues with the helium measurements (large non-statistical variations of an unknown nature).

§ 3.1.1 Solar Wind Collection

The Genesis mission collected solar wind with 5 separate arrays of collectors, that were made up of a wide variety of materials suited to different purposes. Three of these arrays were deployed in such a manner as to selectively sample different types of solar wind: low speed SW (L-SW), high speed SW (H-SW), and coronal mass ejections (CME). The other two arrays were exposed to the solar wind throughout the duration of solar wind collection. On board electronics measured parameters such as electron and proton speeds, direction and temperatures and a set of thresholds were derived by carefully-written algorithm which were used to determine which of the SW regimes was present at any given time and to deploy the corresponding collector array.

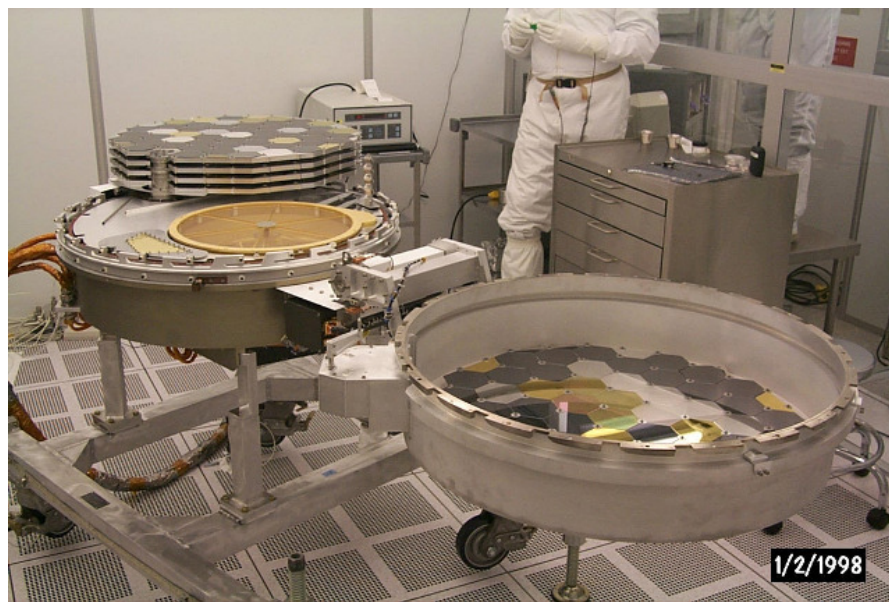
The collector arrays were a patchwork of different collector materials (Figure 3.1). Each array held 54 four-inch diameter hexagonal collectors and 6 half-hexagons (Jurewicz et al. 2003). Many of the collector materials used were developed by the semiconductor industry and were commercially available. However, to achieve the level of purity needed for specific measurements, some of the collector materials were developed specifically for Genesis. This was especially important for noble gas measurements because the semiconductor industry often fabricates their materials in a noble gas atmosphere. Four of the collector arrays were stacked, with the fifth one installed on the inside of the lid of the SRC. This configuration meant that the lid array and the top of the 4 stacked arrays collected SW continuously over the entire mission whenever the SRC was open, no matter which tray was deployed, and we designate these as bulk SW collectors. The remaining 3 arrays were able to swing out and be exposed to the SW when a specific SW regime was detected and therefore separately collect the different types of SW (Burnett et al. 2003).

Figure 3.1: a) One of the Genesis regime collector arrays. b) The whole collector assembly with the stacked regime collector arrays, additional regime bulk array on the inside of the canister lid, and additional collectors.

a)



b)



The deployment of the regime arrays were determined by the data collected by a pair of onboard monitors. The main parameter used to separate between L-SW and H- SW was the proton speed. Detecting a CME event was more complicated such as looking for bi-direction electron flow and large helium abundance variations. The algorithm was biased towards keeping the H-SW collector array the purest, with the L-SW having second priority after that. Therefore, the CME regime is probably the most mixed with other regimes (Neugebauer et al. 2003). The plot in Figure 3.2 shows the collection times of the different regimes versus SW speed. There is quite a bit of overlap between the fast and slow wind because there was a large amount of hysteresis built into the algorithm to keep the tray activity to a minimum. Nevertheless, any differences that are associated with SW speed should clearly be visible.

Figure 3.2: Number of hours of collection time vs the SW speed (Reisenfeld et al. 2005).

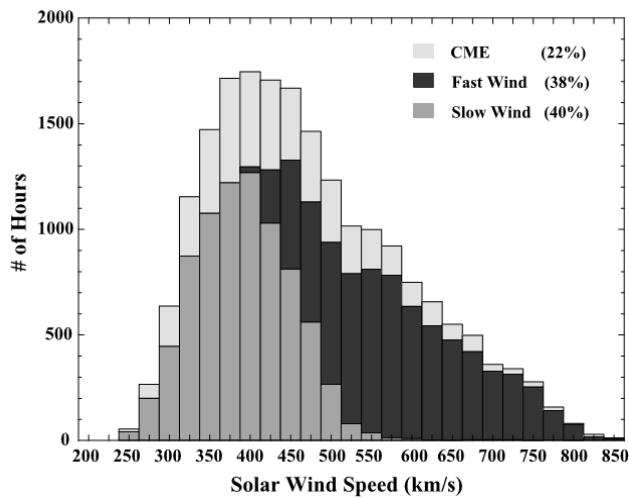


Table 3.1 shows the total exposure time for each array. Bulk SW was collected for a bit over two years. The L- and H-SW had very similar total collection times of a just under 1 year, and the CME had the least amount of collection time, as expected. It should

be noted that we are, in fact, able to distinguish between the different collector regimes even after the crash of the SRC shattered and mixed all of the collectors. The sapphire (and other) substrates of the collectors for each regime were made of a different thickness (bulk – 700 μm , H – 600 μm , L – 550 μm , CME – 650 μm (Allton et al. 2005). This turned out to be an important safety factor, considering the breakage that occurred with the hard landing. With painstaking cataloguing and measurement of the crash shards by the Genesis curation staff, it was possible to identify which collector array a particular shard came from.

Table 3.1: Solar wind collection time for each of the SW regime collectors (Reisenfeld et al. 2005).

SW Regime	Days exposed to the SW
Bulk	852.83
L	333.67
H	313.01
CME	193.25

§ 3.1.2 Collector Material

The collector material chosen for analyzing the light noble gases of the different SW regimes was AloS (see § 1.4.1 for a full description of this material). This collector was chosen for two primary reasons: 1) High expected noble gas retentivity and 2) Ease extracting the gas using laser ablation and 3) Low blank for the vapor-deposited aluminum film. However, for Kr and Xe, anomalous trapping occurs at the interface

between the substrate and the deposited Al film, but this will not be a factor since Kr and Xe will be measured in the PAC. After some of the early analyses, there was some question as to the validity of the first point, the diffusive losses, but the results of the diffusion experiment described in Chapter 2 shows that diffusion losses are minimal and should not have a significant impact on the isotopic ratios of retained Ne and Ar.

§ 3.2 Methods: Regime Measurements

§ 3.2.1 Gas Extraction

Light noble gases were extracted from the Genesis AloS samples by ablating areas on the order of 1 to 10 mm² with a Q-switched, pulsed IR-laser to evaporate the Al film containing the implanted SW gases from the sapphire substrate and thus liberate the gases. The samples were loaded in a laser extraction cell (Figure 3.3) with four separate deep wells, designed to keep most of the sputtered Al film from depositing on the sapphire viewport. Sputtered Al on the viewport blocks the laser beam causing problems for subsequent runs by reducing the transmitted pulses. The samples were placed on Ta-foil “ribs” to minimize the residual power density delivered to the bottom of the cell, which helps reduce the blank. Since sapphire (of both the viewport and the sample substrate) is transparent at 1064 nm, the Nd-YAG wavelength, it is not heated and only the Al is volatilized by the pulse, also greatly reducing the blank.

Figure 3.3: Sample cell with sapphire viewport. In each chamber there is one piece of Al₂O₃ (bulk, L, H, or CME), supported by Ta-foil ribs.



The sample cell was mounted on a computer-controlled stage: Newport Programmable 2-D Stage (PMC200-P), which was controlled with a flexible LabVIEW program (code shown in Appendix D) written to replace the obsolete DOS program. A predetermined rectangular area was entered into the stage controller program, and then the sample cell on the stage would move back and forth under the laser beam, volatilizing the aluminum film from the sapphire substrate. The time for the entire raster depended on the parameters of that sample, but were typically between 5 and 20 minutes.

The power output of the laser is controlled by a pair of air-spaced water-cooled Glan-Thomson polarizer cubes, the second of which can be rotated. The beam is then reflected by a 45-degree dichroic mirror onto the optical axis of a microscope, and finally variably focused below (~ 0.5 mm) the Al-film to achieve optimum spot size (~ 0.05 mm²)

and power density on the surface of the sample. Earlier versions of this laser system are described in detail in (Kehm 2000) and (Nichols 1992). Figure 3.4 shows an image of the AloS pieces after many individual raster analyses.

Figure 3.4: AloS after IR-laser ablation. Each rectangular area represents a separate analysis run of either neon or argon.



§ 3.2.2 Mass Spectrometry

For these measurements, neon and argon were measured at different times. The procedure for the argon measurements is essentially the same as described in § 2.3.2.2 above except for the extraction method describes in § 3.2.1.

The procedure for the neon measurements is similar to that described in § 2.3.2.2, however the majority of the neon measurements were done on MS-North as opposed to

MS-South. MS-North does not have a hydrogen getter and thus required a more careful cleaning of the gas prior to inlet into the mass spectrometer as well as requiring careful monitoring of the hydrogen levels in order to apply corrections for hydrides and high pressure effects (see Meshik et al. 2007).

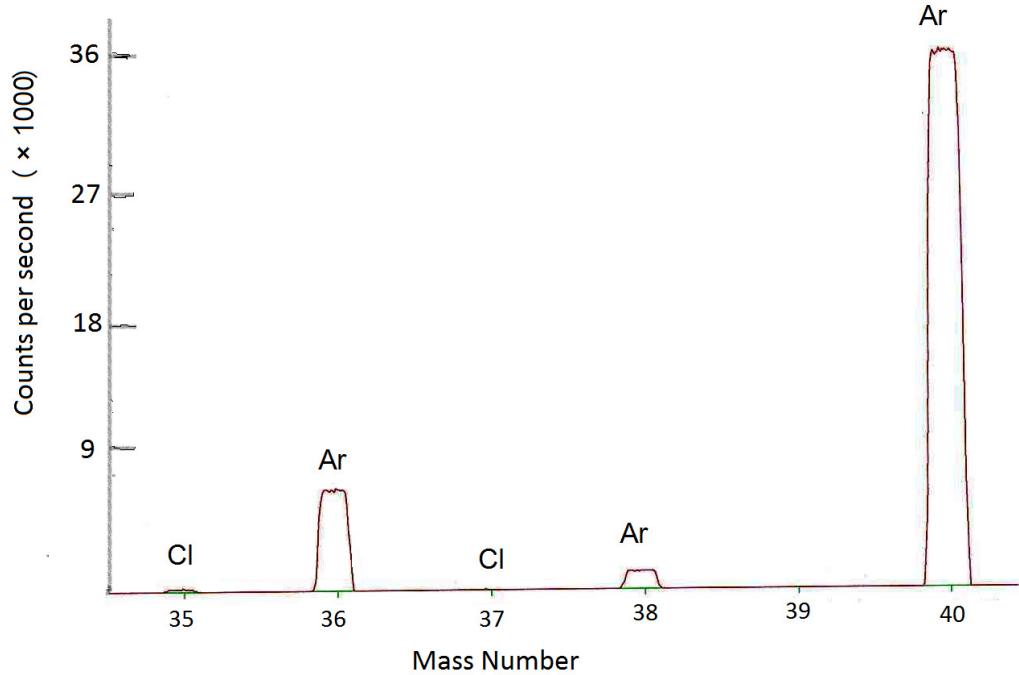
§ 3.2.3 Blanks

Procedural blanks were done frequently throughout the measurements. The amount of ^{40}Ar in all samples was the same or less than the amount measured in the associated blanks. Therefore, we can conclude that all of the ^{40}Ar is background and not from the sample. The atmospheric corrections at ^{36}Ar and ^{38}Ar was therefore made by subtracting off atmospheric argon based on the measured amount of ^{40}Ar , which ranged from 1% to 30% but was typically <5%. Neon blanks were subtracted from the raw data and were typically no more than 1% of the amount of ^{20}Ne .

Figure 3.5 shows a typical mass scan of the peaks from masses 35 to 40 done during SW Ar analysis. There is very little Cl, which appears at masses 35 and 37, so the HCl corrections at masses 36 and 38 were applied but were usually negligible. The $^{40}\text{Ar}/^{36}\text{Ar}$ is about 5 (compared to 295 in terrestrial atmosphere), demonstrating that in this measurement the Ar is 98% pure SW, with negligible and well-established corrections for atmospheric contributions at ^{36}Ar and ^{38}Ar . This means there is very little terrestrial contamination which could have come either from contamination of the sample by Utah mud during the crash landing, or it could come from the blank. These results demonstrate that the laser extraction technique we used (§ 3.2.1) keeps the extraction blank very low

and, because we carefully clean and electropolish all parts before adding them to the vacuum system, the system blank also very low.

Figure 3.5: Mass scan of the peaks at masses 35 to 40 during SW Ar measurements.



§ 3.2.4 Calibrations and Standards

During the measurements, frequent air calibrations were run using our standard air calibration bottle (am-air), and using a similar procedure as the real measurements. To calibrate the amount of Ar in the air standard, we also measured grains of LP-6 biotite, an international Ar standard which is commonly used in K-Ar chronology (Charbit et al. 1998). The LP-6 standard contains $(1.580 \pm 0.006) \times 10^{14}$ atoms $^{40}\text{Ar}/\text{g}$, and is homogeneous to the mg-level. Assuming that am-air has unfractionated terrestrial Ne/Ar ratio, this calibration provides the amounts of Ne and Ar to within ~5%. This air

standard is also used to determine the instrumental mass discrimination, which were typically 1.5% per amu for Ne and 0.5% per amu for Ar.

In addition to the usual air standard, a special calibration system was designed to correct for high pressure and hydride effects on the neon isotopes, described in detail in (Meshik et al. 2007). Essentially, this was done by adding amounts of pure ^4He and H, prepared in a separate pipette, to the regular neon calibration to match the specific amounts of those gases in a particular Genesis sample. This enabled corrections to be made for pressure-induced space charge effects which can change the Ne sensitivity by up to several percent, and the mass discrimination by up to 0.2% per amu. This was also used to correct for NeH^+ , as it was found that $^{20}\text{NeH}^+$ could increase the mass 21 signal by tens of percent. The NeH^+ effect, the sensitivity losses and the discrimination changes are all due to the space charge (pressure) effects of the GS-61 ion source and are limited to the light noble gases (He and Ne) since Ar is run at much lower pressures.

§ 3.2.5 Interferences

See § 2.3.2.1 for discussion of argon interferences and the values used for this data are the same as shown in Table 2.7. The neon interferences include those discussed in § 2.3.2.1 and the NeH^+ interferences discussed in § 3.2.4.

§ 3.3 Data

The measurements of SW regimes were done in several different sets over several months and years in some cases. The results for these neon measurements are shown in Table 3.2 below. Data are corrected for instrumental mass discrimination and procedural blanks. The numbers in italics represent the weighted average of the first set of the measurements when isobaric contributions of H^{20}Ne^+ to ^{21}Ne and HD^+ with H_3^+ to ^3He were poorly controlled. In one bulk SW analysis from the second series of measurements the $^{21}\text{Ne}/^{22}\text{Ne}$ ratio apparently has an interference problem; this crossed-out ratio is omitted. Rather than calculating the expected error from the standard deviation, which makes little sense for only a limited number of measurements, the errors on the average ratios are computed by compounding the errors on the individual sums of the numerator and the denominator. Scatter between replicate measurements which is much larger than these statistical uncertainties, indicates unquantified systematic errors, possibly because of problems with a specific target or inadequate corrections for space charge effects and/or interferences.

Argon isotopic ratios and SW fluxes from aluminum on sapphire (AlO₃) bulk and regime collectors are shown in Table 3.3. For the ratios, the data are shown from both before and after the subtraction of atmospheric Ar (see § 2.3.2.2 for full explanation). Averages for the bulk and regimes together are given for the $^{36}\text{Ar}/^{38}\text{Ar}$ ratios in the bottom. All data are corrected for mass discrimination, but the backscattering correction is negligible and so it is not applied.

Table 3.2: Neon isotopic regime results (Meshik et al. 2007). Backscatter corrections are applied to the averages. ^{20}Ne fluxes are determined with $\pm 9\%$ (1σ).

SW Regime	$^{20}\text{Ne}/^{22}\text{Ne}$	$^{21}\text{Ne}/^{20}\text{Ne} (\times 10^{-3})$	^{20}Ne $\times 10^8 / \text{m}^2 \cdot \text{s}$	Raster Area (mm^2)
Bulk SW	13.86 ± 0.06	<i>NeH</i>	2.43	1.1
	14.15 ± 0.07	2.49 ± 0.06	2.20	0.5
	14.04 ± 0.06	2.51 ± 0.04	1.98	1.1
	13.88 ± 0.07	2.77 ± 0.06 (<i>NeH?</i>)	2.23	1.0
	13.80 ± 0.05	2.44 ± 0.04	2.28	1.7
	13.94 ± 0.05	2.45 ± 0.04	2.24	1.1
	13.945 ± 0.025	2.473 ± 0.043	2.23	
High Speed (H)	13.93 ± 0.08	<i>NeH</i>	1.77	3.0
	13.95 ± 0.07	2.49 ± 0.04	1.79	3.2
	13.93 ± 0.06	2.47 ± 0.05	1.81	3.2
	13.937 ± 0.041	2.480 ± 0.044	1.79	
CME (E)	13.99 ± 0.04	<i>NeH</i>	2.13	5.1
	13.92 ± 0.06	2.41 ± 0.04	2.10	5.1
	13.93 ± 0.06	2.41 ± 0.04	2.23	5.1
	13.947 ± 0.031	2.41 ± 0.04	2.15	
Low speed (L)	13.89 ± 0.04	<i>NeH</i>	1.73	2.8
	13.97 ± 0.06	2.48 ± 0.04	1.56	3.2
	14.00 ± 0.06	2.39 ± 0.04	1.67	3.2
	13.953 ± 0.031	2.435 ± 0.037	1.65	
Total weighted average SW	13.945 ± 0.016	2.450 ± 0.021	1.96	

Table 3.3: Argon isotopic regime results (Meshik et al. 2007). Note: ^{36}Ar fluxes are determined with $\pm 9\%$ (1σ). This includes statistical error of $\pm 2\%$ and an overestimation of the rastered area due to scratches.

SW Regime	Measured Ar composition		All ^{40}Ar removed		Raster Area (mm^2)
	$^{40}\text{Ar}/^{36}\text{Ar}$	$^{36}\text{Ar}/^{38}\text{Ar}$	^{36}Ar flux ($10^6/\text{m}^2\cdot\text{s}$)	$^{36}\text{Ar}/^{38}\text{Ar}$	
Bulk SW	5.178 ± 0.007	5.480 ± 0.014	3.90	5.482 ± 0.014	10.5
	11.373 ± 0.019	5.461 ± 0.016	3.84	5.467 ± 0.017	4.77
	3.211 ± 0.003	5.499 ± 0.010	3.88	5.502 ± 0.010	16.9
	2.716 ± 0.002	5.508 ± 0.009	3.91	5.510 ± 0.008	21.9
	4.453 ± 0.006	5.514 ± 0.012	3.49	5.517 ± 0.012	9.61
	3.557 ± 0.009	5.503 ± 0.021	3.43	5.505 ± 0.021	8.32
Bulk Weighted Average		5.499 ± 0.005	3.81	5.501 ± 0.005	
High Speed (H)	6.645 ± 0.009	5.505 ± 0.013	1.94 (omitted)	5.509 ± 0.013	34.84
	12.126 ± 0.025	5.506 ± 0.019	2.82	5.514 ± 0.019	11.12
	8.124 ± 0.025	5.449 ± 0.034	2.56	5.453 ± 0.035	9.79
	9.852 ± 0.028	5.482 ± 0.025	2.85	5.488 ± 0.026	7.04
	15.283 ± 0.079	5.443 ± 0.040	2.86	5.450 ± 0.043	3.83
H Weighted Average		5.496 ± 0.009	2.82	5.499 ± 0.010	
CME (E)	17.459 ± 0.036	5.480 ± 0.019	4.57	5.491 ± 0.021	8.96
	27.051 ± 0.163	5.459 ± 0.126	3.50	5.47 ± 0.14	2.62
	112.715 ± 0.645	5.379 ± 0.057	2.51	5.416 ± 0.093	1.31
	102.106 ± 0.589	5.462 ± 0.082	2.88	5.54 ± 0.13	1.34
	14.786 ± 0.093	5.433 ± 0.045	2.73	5.439 ± 0.047	10.8
	13.767 ± 0.040	5.462 ± 0.038	2.50	5.470 ± 0.039	14.9
CME Weighted Average		5.464 ± 0.016	3.68	5.467 ± 0.017	
Low-speed (L)	8.879 ± 0.009	5.491 ± 0.013	4.01	5.496 ± 0.014	12.4
	16.817 ± 0.064	5.469 ± 0.085	2.94	5.478 ± 0.091	3.32
	5.414 ± 0.014	5.528 ± 0.020	3.12	5.532 ± 0.021	14.6
	11.009 ± 0.029	5.547 ± 0.027	3.15	5.557 ± 0.028	7.91
	3.750 ± 0.008	5.515 ± 0.023	3.58	5.518 ± 0.024	21.9
11.945 ± 0.033	5.449 ± 0.024	3.63	5.454 ± 0.025	8.19	
L Weighted Average		5.503 ± 0.009	3.63	5.508 ± 0.010	
Total SW Weighted Average		5.497 ± 0.004		5.500 ± 0.004	

Since neon and argon were not measured at the same time, elemental ratios shown below in Table 3.4 depend on the rastered areas as well as the air standard calibration, and therefore have a relatively high uncertainty of ~9%, based on the scatter between measurements. Because of residual systematic calibration uncertainties, error limits are quoted on the $^{20}\text{Ne}/^{36}\text{Ar}$ elemental ratios are estimated to be about 9% based on the scatter in replicate analyses of the ^{20}Ne and ^{36}Ar fluxes in the bulk sample.

Table 3.4: Regime elemental ratios, numbers in parenthesis represent 9% error (Meshik et al. 2007).

SW Regime	$^{20}\text{Ne}/^{36}\text{Ar}$
Bulk	59 (5)
H	66 (6)
CME	59 (5)
L	46 (4)

§ 3.4 Data Analysis

§ 3.4.1 Isotopic Regime Fractionation

The main purpose of collecting separate sample of the different solar wind regimes was to look for differences in their isotopic composition which may point towards isotopic fractionation of the SW relative to the photosphere. Specifically, the theory of inefficient Coulomb drag (Bodmer and Bochsler 1998) predicts that this fractionation relative to the photosphere will be different between the L- and H- SW regimes, an idea that was first developed by Geiss et al (1970). Coulomb drag occurs when protons, which are being accelerated out of the solar atmosphere, collide with and transfer

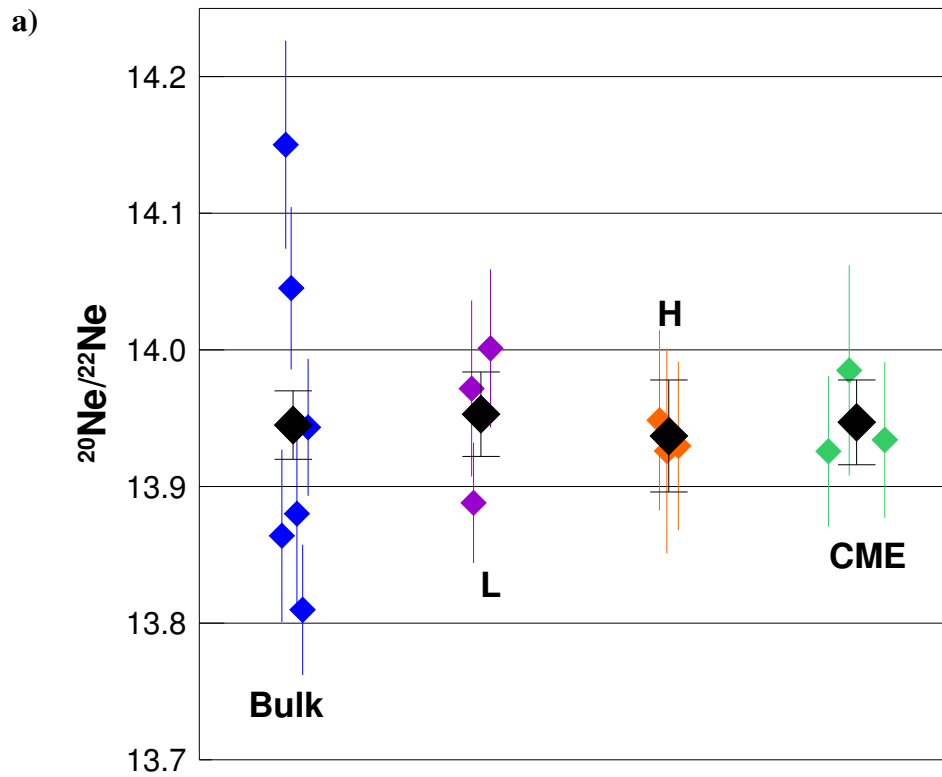
momentum to heavier ions. This process seems to be much less efficient in L-SW than H-SW leading to a predicted difference in the isotopic composition between the two regimes, which would serve as a measure of the overall fractionation of the SW relative to the photosphere. However the exact magnitude of this effect depends on many difficult to verify assumptions (e.g. charge state, Geiss et al (1970)). We know that some fractionation effects do exist in mechanisms leading to corpuscular acceleration from the sun, as large variations are observed in solar flares, but these may involve an entirely different mechanism. Thus, it is important to measure the relative fractionation that may exist between the regimes.

Qualitatively, a light isotope enrichment, in L-SW samples relative to H-SW, is predicted by Coulomb drag effects (Bodmer & Bochsler 2000). This fractionation also depends on mass, and so the largest effect is expected in $^3\text{He}/^4\text{He}$, because of the large relative mass difference. Although, small differences between the L- and H-SW $^{20}\text{Ne}/^{22}\text{Ne}$ have been reported (Heber et al. 2009) we do not find statistically meaningful effects in our own data, and we expect any Coulomb Drag effect to be very small indeed between the different solar wind regimes for $^{36}\text{Ar}/^{38}\text{Ar}$.

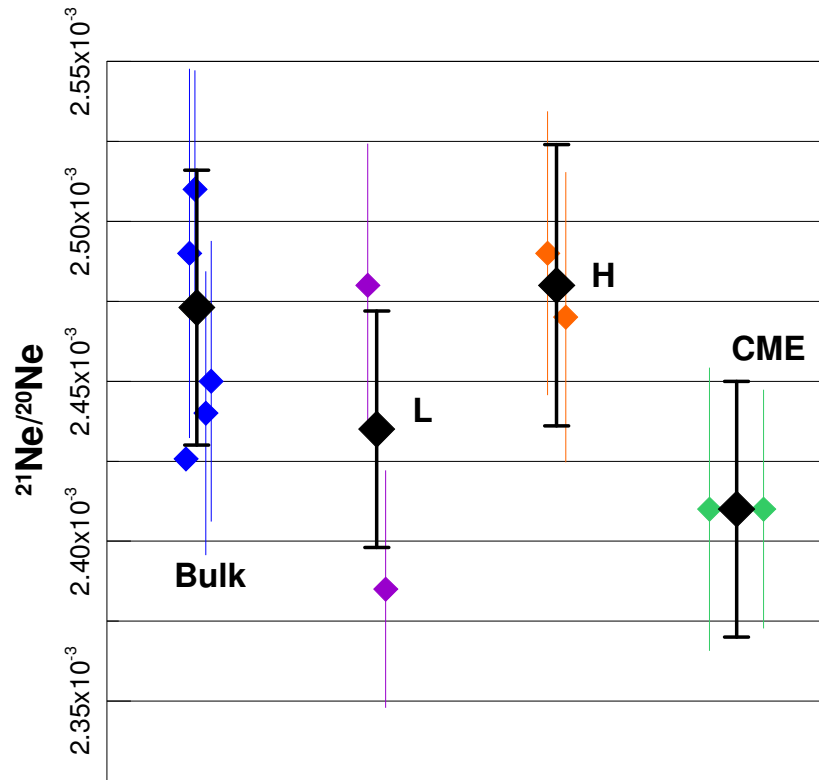
The neon and argon isotopic regime data are plotted in Figure 3.6. We find no statistically significant variations in the isotopic compositions of Ne or Ar at the 1σ level. For $^{20}\text{Ne}/^{22}\text{Ne}$, the L-H difference is $0.24 \pm 0.37\%$, corresponding to an upper limit of 0.98% at the two sigma level. And for $^{36}\text{Ar}/^{38}\text{Ar}$, the L-H difference is $0.11 \pm 0.26\%$ corresponding to a two sigma upper limit of 0.63% . These differences do go in the

direction expected by inefficient Coulomb drag theory, with L-SW lighter than H-SW in each case, but the differences are very slight and much less than the statistical uncertainty in each case.

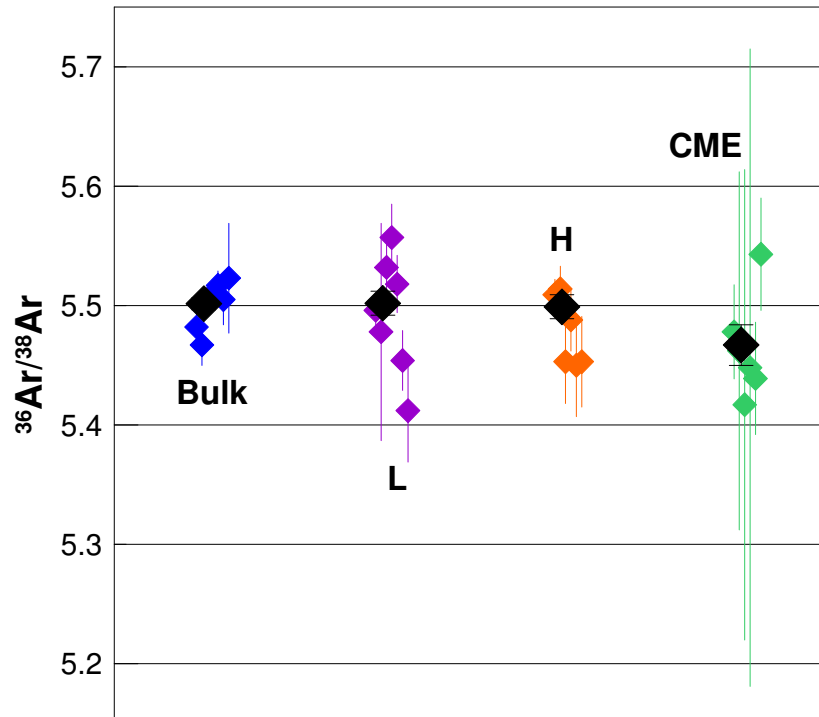
Figure 3.6: Isotopic ratios $^{20}\text{Ne}/^{22}\text{Ne}$ (a), $^{21}\text{Ne}/^{20}\text{Ne}$ (b), and $^{36}\text{Ar}/^{38}\text{Ar}$ (c) for the bulk SW and each of the three SW regimes. Colored points represent individual measurements and black points are the weighted averages (see explanation in § 3.3). All errors are 1σ statistical.



b)



c)

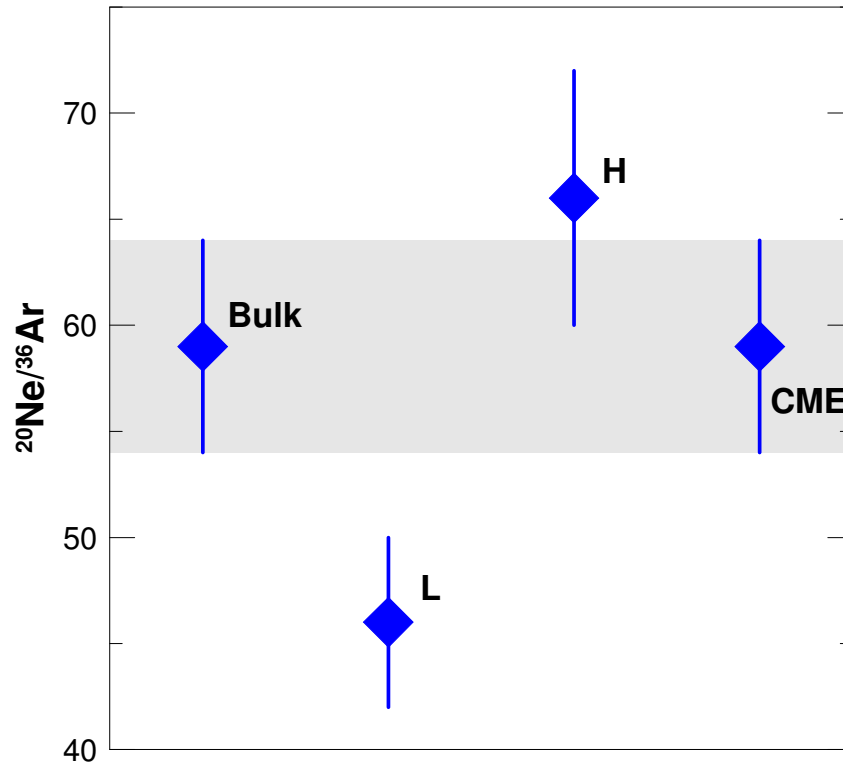


§ 3.4.2 Elemental Regime Fractionation

It is well established that the elemental composition of the SW is fractionated with respect to the photosphere and that this fractionation is correlated with the First Ionization Potential (FIP) of elements (Marsch et al. 1995). The SW is enriched in low-FIP elements compared to the photosphere, and additionally, the L-SW is enriched in low-FIP elements relative to the H-SW. Unlike isotopic fractionation, which requires high-precision measurements, the elemental fractionation between the SW regimes has long been confirmed by spacecraft data (von Steiger and Geiss 1989). Reisenfeld et al (2007) and have shown that the elemental fractionation between the L- and H-SW is not a discrete difference between the regimes, but is a continuous function of SW speed.

Our $^{20}\text{Ne}/^{36}\text{Ar}$ ratios (Figure 3.7) confirm this effect. In this case, the difference between the L- and H-SW is about 25%, with the L-SW enriched in Ar (Ne FIP = 21.56V, Ar FIP = 15.75V), the lower FIP element, compared to the H-SW. The H-SW ratio is also closer to the bulk SW value (within 1σ), indicating a greater amount of fractionation in the L-SW, in agreement with spacecraft measurements (Geiss et al. 1995).

Figure 3.7: $^{20}\text{Ne}/^{36}\text{Ar}$ of the bulk, H, L, and CME SW regimes. The L-SW is about 25% lower than H- SW. This difference is attributed to fractionation in the SW based on the first ionization potential of different elements.



§ 3.4.3 Precise Bulk SW Isotopic Ratios

From the earliest SW measurements, there has been no question that the neon isotopic composition of the terrestrial planets differs from that of the solar (Wieler 2002). Most of the pre-Genesis SW $^{20}\text{Ne}/^{22}\text{Ne}$ measurements have clustered around 13.7 to 13.8, and even with fairly large statistical uncertainties, this is well separated from other planetary reservoirs such as Earth's atmosphere, 9.80 (Eberhardt et al. 1965) or Mars' atmosphere, 10.1 ± 0.7 (Pepin 1991). However, with Genesis samples, obtaining a much more precise value is possible.

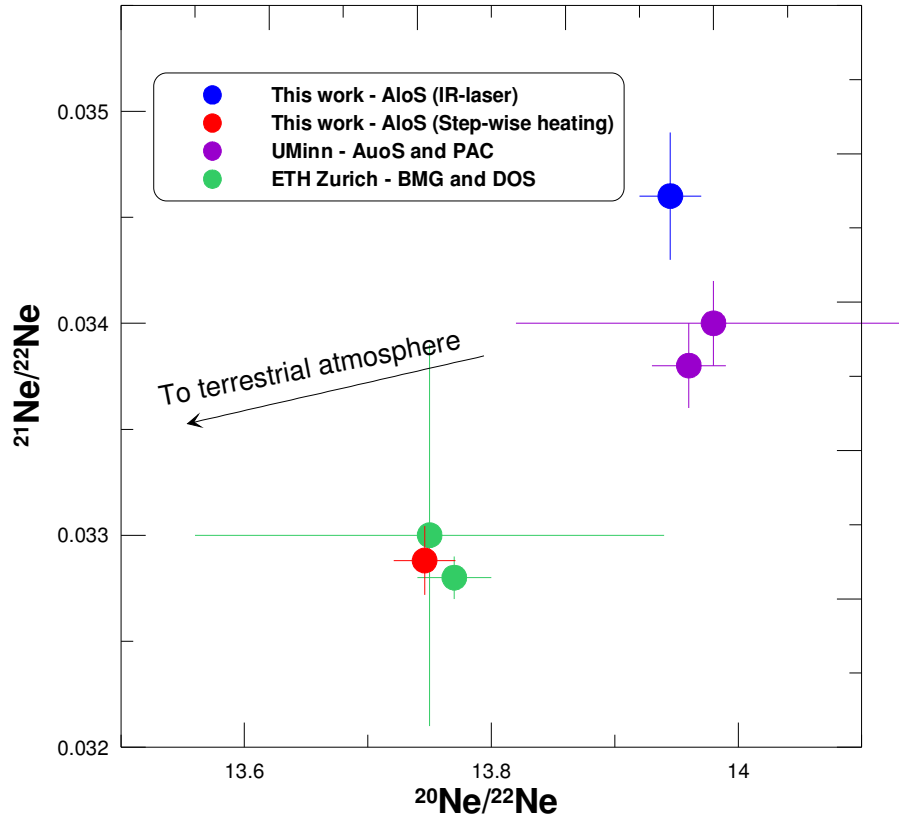
Several groups have measured SW Ne isotopes in Genesis samples using different techniques and different collector materials, employing four different mass spectrometers, none of which were originally designed to measure SW light noble gases. These are compared in a Figure 3.8. Heber et al. (2009a) and Grimberg et al. (2006) at ETH-Zurich measured SW Ne from the Genesis collector materials diamond-like-carbon on silicon (DOS) and bulk metallic glass (BMG) respectively. While Pepin (unpublished data) at the University of Minnesota used PAC and gold on sapphire (AuoS). Also compared are two results from this work: the bulk SW measurements discussed in this chapter made using the IR-laser extraction technique on AloS and the measurements from Chapter 2 made using the step-wise heating extraction technique also from AloS.

The $^{20}\text{Ne}/^{22}\text{Ne}$ bulk SW measurements seen in Figure 3.8 fall into two distinct groups: ~ 13.95 and ~ 13.75 , while the $^{21}\text{Ne}/^{22}\text{Ne}$ bulk SW measurements fall into three distinct groups: ~ 0.035 , ~ 0.034 , and ~ 0.033 . It is unclear at this time what is causing the disparities, but there are several possibilities. First, the ratios measured by the IR-laser ablation technique ($^{20}\text{Ne}/^{22}\text{Ne} = 13.945$ and $^{21}\text{Ne}/^{22}\text{Ne} = 0.0346$) were made in the presence of a large amount of hydrogen that required special corrections, it may be that the high-pressure and hydride corrections applied were not sufficiently accurate. Second, either incomplete degassing which would leave behind in the sample relatively heavy gas, or overheating of surrounding material during the laser raster which would release extra light gas, although there is no evidence for this.

Conversely, it is possible that the relatively lower $^{20}\text{Ne}/^{22}\text{Ne}$ and $^{21}\text{Ne}/^{22}\text{Ne}$ measurements (from this work by step-wise heating and ETH-Zurich) may be slightly under-corrected for atmospheric blank, as this would lower the measured isotopic ratios. This would require an addition of roughly 4% of atmospheric neon to lower $^{20}\text{Ne}/^{22}\text{Ne}$ from 13.95 to 13.75. However, as seen in Figure 3.8, none of the different groups of points lie on a SW-terrestrial atmospheric mixing line, implying that the difference between the different measured values is not under-correction or over-correction of atmospheric blanks.

Additionally, although they do not have the precision to be absolutely conclusive, other measurements of the SW before Genesis all agree with the heavier group of Ne from Genesis: SWC, $^{20}\text{Ne}/^{22}\text{Ne} = 13.7 \pm 0.3$ and $^{21}\text{Ne}/^{22}\text{Ne} = 0.033 \pm 0.004$ (Geiss et al. 2004); lunar regolith, $^{20}\text{Ne}/^{22}\text{Ne} = 13.8 \pm 0.1$ and $^{21}\text{Ne}/^{22}\text{Ne} = 0.0328 \pm 0.0005$ (Benkert et al. 1993); lunar regolith, $^{20}\text{Ne}/^{22}\text{Ne} = 13.85 \pm 0.04$ and $^{21}\text{Ne}/^{22}\text{Ne} = 0.0334 \pm 0.0003$ (Benkert et al. 1993; Palma et al. 2002); and SOHO, $^{20}\text{Ne}/^{22}\text{Ne} = 13.74 \pm 0.25$ and $^{21}\text{Ne}/^{22}\text{Ne} = 0.032 \pm 0.008$ (Kallenbach et al. 1997) and ACE (Leske et al. 2007). Therefore, taking all of the current evidence into consideration, I would suggest that the most likely values for the SW Ne ratios are: $^{20}\text{Ne}/^{22}\text{Ne} = 13.75 \pm 0.02$ and $^{21}\text{Ne}/^{22}\text{Ne} = 0.0329 \pm 0.0002$. However, the final answer will come when measurements are done on modern mass spectrometers designed to tolerate high pressure effects. We are still waiting for the new machine we developed in cooperation with several UK-based companies for this purpose to be built, and hope to be able provide a more definitive answer in the future.

Figure 3.8: Neon 3 isotope plot comparing Genesis measurements from multiple labs and collector materials (Grimberg et al. 2006; Meshik et al. 2007; Heber et al. 2009) along with the direction to the terrestrial atmosphere. The points are separated into 3 distinct groups, but not along a SW-terrestrial atmosphere mixing line. All errors are 1σ statistical.

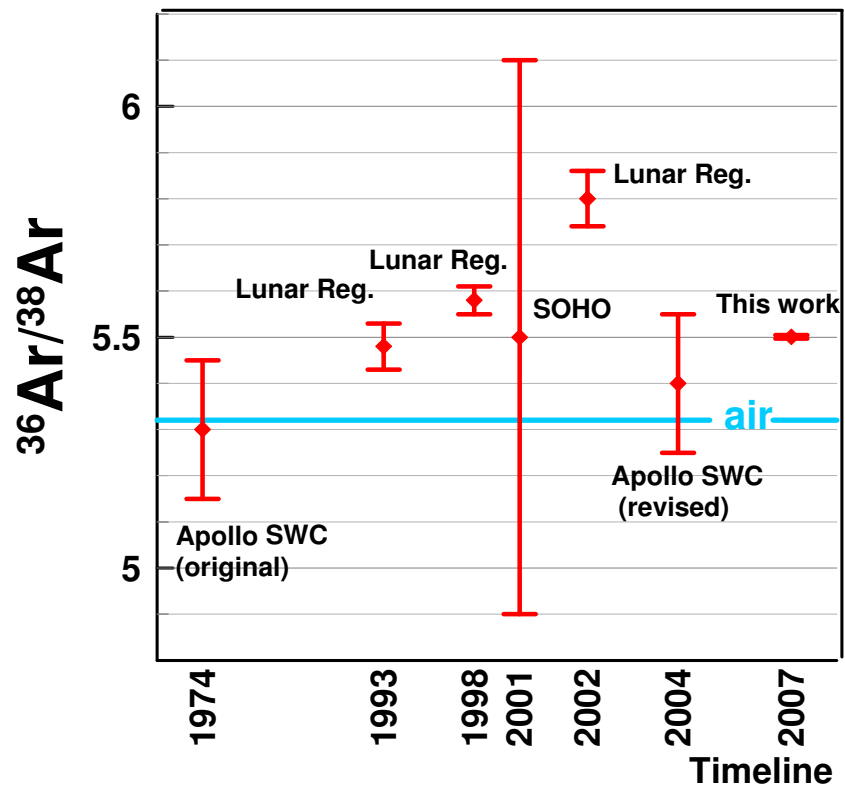


Several measurements of the SW $^{36}\text{Ar}/^{38}\text{Ar}$ ratio have been made over the past few decades, which are summarized in Figure 3.9 along with the terrestrial atmospheric value. Although it had become widely accepted that there was a variation in the Ar isotopic ratio among solar system reservoirs, e.g. a difference between solar wind and terrestrial $^{36}\text{Ar}/^{38}\text{Ar}$ in this case, the available data made it difficult to discern exactly how big the difference really is.

The precision of isotopic ratios from the present generation of spacecraft instruments, such the SOHO value (Weygand et al. 2001) is insufficient to address planetary science issues, with 1 sigma uncertainties that cover the entire range of possible SW and terrestrial values. The short exposure of the Apollo foils limited the precision of those data as well, again making it impossible to distinguish the solar and atmospheric $^{36}\text{Ar}/^{38}\text{Ar}$ ratios (Geiss et al. 2004; Cerutti 1974). Multiple measurements of $^{36}\text{Ar}/^{38}\text{Ar}$ from lunar soils using different stepped-release methods (Benkert et al. 1993; Becker et al. 1998; Palma et al. 2002) all suggested that the SW ratio was higher than terrestrial, with statistical variations beyond the differences between the lunar soil measurements themselves, it was difficult to conclude how much higher with any certainty. The relatively high ratio determined from several lunar regolith studies (Becker et al. 1998; Palma et al. 2002) likely can be at least partially explained by the fact that they separated out many of the isotopically heavier steps and attributed them to the “SEP” component (Grimberg et al. 2006). Reanalysis of that data should bring those values closer to 5.5.

The bulk SW $^{36}\text{Ar}/^{38}\text{Ar}$ presented in this work (5.501 ± 0.005) is the most precise measurement made to date. Our bulk solar wind $^{36}\text{Ar}/^{38}\text{Ar}$ is higher than the terrestrial atmosphere by $3.32 \pm 0.09 \%$. This should lead to improved constraints on models for the formation and evolution of the terrestrial atmosphere, in particular this difference may reflect atmospheric losses early in earth’s history.

Figure 3.9: Comparison of solar argon measurements: Apollo foils, 5.3 ± 0.3 (Cerutti 1974); Apollo foils revised, 5.4 ± 0.15 (Geiss et al. 2004); lunar regolith, 5.48 ± 0.05 (Benkert et al. 1993), 5.58 ± 0.03 (Becker et al. 1998), and 5.80 ± 0.06 (Palma et al. 2002); SOHO, 5.50 ± 0.6 (Weygand et al. 2001) and terrestrial air, 5.319 ± 0.008 (Ozima & Podosek 2001). In this work we are reporting a precise value of 5.501 ± 0.005 .



Chapter 4 Summary of results

The first goal of this work was to determine if the Genesis aluminum collectors AloS and PAC were retentive of the light noble gases helium, neon, and argon, under the conditions of SW collection. Specifically, whether or not diffusion could have caused large enough losses to significantly alter the measured isotopic ratios of these gases in either collector. This was tested by conducting a long-term diffusion experiment where flown pieces of these two collectors were baked for approximately 1 year, a comparable to the ~2.5 years of the Genesis mission.

The initial results of this experiment showed appreciable losses of helium and some amount of neon from both collectors. In all cases, the losses from PAC were either the same or higher than from AloS. These losses were large enough to significantly impact the $^3\text{He}/^4\text{He}$ ratio, but not the neon or argon isotopic ratios within current analytical precision. However, after using these data to approximate the losses under the real conditions of the Genesis mission during SW collection, which accounts for the fact that the SW gases are continuously being implanted simultaneously with diffusive losses, the significance of these losses was lessened substantially and in fact dropped below typical measurement uncertainties, at least in the AloS collector material. Therefore, I conclude that the AloS collector is suitable for all light noble gas measurements, but more caution should be used with the PAC for He and Ne measurements.

The other goals of this work were to make precise isotopic measurements of SW neon and argon from the AloS collector in order to 1) look for compositional differences

between the SW regimes (particularly the L- and H-SW regimes) and 2) to measure the most precise bulk SW values possible. The results of the regime measurements show less than 1σ difference in the isotopic composition between the different SW regimes. For $^{20}\text{Ne}/^{22}\text{Ne}$, the L-H difference is $0.24 \pm 0.37\%$, corresponding to an upper limit of 0.98% at the two sigma level. And for $^{36}\text{Ar}/^{38}\text{Ar}$, the L-H difference is $0.11 \pm 0.26\%$ corresponding to a two sigma upper limit of 0.63% . This is a very tight constraint on the possible isotopic fractionation between the SW regimes, and it might be used to constrain the fractionation of the SW composition relative to that of the photosphere. And finally, after making and surveying numerous measurements, I suggest that the best current estimate of the bulk SW is¹:

$$^{36}\text{Ar}/^{38}\text{Ar} = 5.501 \pm 0.005$$

$$^{20}\text{Ne}/^{22}\text{Ne} = 13.75 \pm 0.02$$

$$^{21}\text{Ne}/^{22}\text{Ne} = 0.0329 \pm 0.0002.$$

¹ It should be noted again that the He and Ne measurements require corrections for space charge effects because it required operation of the GS-61 ion source at pressure regimes it was not designed for. The Ar measurements were made in the low-pressure regime the GS-61 is best-suited for. Here there are no space-charge effects, all ions that are accelerated can be counted (if directed into the electron multiplier) and all ions spend approximately the same time in the ionization region so correction for double-charging and hydrides are both generally negligible and always constant. Thus the Ar data should be the best, and this is reflected in the resulting precision.

References

- Aellig MR, Lazarus AJ, Steinberg JT, 2001 The solar wind helium abundance: Variation with wind speed and the solar cycle. *Geophysical Research Letters* **28**: 2767-2770.
- Allton JH, Calaway MJ, Rodriguez MC, Hittle JD, Wentworth SJ, Stansbery EK, McNamara KM, 2006 Genesis Solar Wind Sample Curation: A Progress Report. *Proc. of the Lunar and Planetary Science Conference* **37**: 1611.
- Allton JH, Stansbery EK, McNamara KM, 2005 Size Distribution of Genesis Solar Wind Array Collector Fragments. *Proc. of the Lunar and Planetary Science Conference* **36**: 2083.
- Allton JH, Stansbery EK, McNamara KM, Meshik A, See TH, Bastien R, 2005 Initial Subdivision of Genesis Early Science Polished Aluminum Collector. *Proc. of the Lunar and Planetary Science Conference* **36**: 1806.
- Aluminum Standards and Data 2000*, The Aluminum Association, Washington DC.
- Anders, E, Grevesse N, 1989 Abundances of the elements: Meteoritic and solar. *Geochimica et Cosmochimica Acta* **53**: 197-214.
- Ashworth DG, Owen R, Munn B, 1990 Representation of ion implantation profiles by Pearson frequency distribution curves. *Journal of Physics D: Applied Physics* **23**: 870-876.
- Axford WI, 1985 The solar wind. *Solar Physics* **100**: 575-586.
- Barracough BL, Dors EE, Abeyta RA, Alexander JF, Ameduri FP, Baldonado JR, Bame SJ, Casey PJ, Dirks G, Everett DT, Gosling JT, Grace KM, Guerrero DR, Kolar JD, Kroesche JL, Lockhart WL, McComas DJ, Mietz DE, Roese J, Sanders J, Steinberg JT, Tokar RL, Urdiales C, Wiens RC, 2003 The Plasma Ion and Electron Instruments for the Genesis Mission. *Space Science Reviews* **105**: 627-660.
- Becker R, Schlutter DJ, Rider PE, Pepin RO, 1998 An acid-etch study of the Kapoeta achondrite: Implications for the argon-36/argon-38 ratio in the solar wind. *Meteoritics and Planetary Science* **33**: 109-113.
- Begemann F, Weber HW, Hintenberger H, 1976 On the primordial abundance of argon-40. *Astrophysical Journal* **203**: L155-L157.
- Benkert J, Baur H, Signer P, Wieler R, 1993 He, Ne, and Ar From the Solar Wind and

- Solar Energetic Particles in Lunar Ilmenites and Pyroxenes. *Journal of Geophysical Research* **98**: 13147.
- Bernatowicz TJ, Hohenberg CM, Podosek FA, 1979 Xenon component organization in 14301. *Proc. of the Lunar and Planetary Science Conference* **10**: 1587-1616.
- Bochsler P, 2000 Solar Wind Composition. In *Encyclopedia of Astronomy and Astrophysics*, Murdin P (ed), p. 2303.
- Bodmer R, Bochsler P, 1998 The helium isotopic ratio in the solar wind and ion fractionation in the corona by inefficient Coulomb drag. *Astronomy and Astrophysics* **337**: 921-927.
- Bodmer R, Bochsler P, 2000 Influence of Coulomb collisions on isotopic and elemental fractionation in the solar wind acceleration process. *Journal of Geophysical Research* **105**: 47-60.
- Borini G, Wilcox JM, Gosling JT, Bame SJ, Feldman WC, 1981 Solar wind helium and hydrogen structure near the heliospheric current sheet - A signal of coronal streamers at 1 AU. *Journal of Geophysical Research* **86**: 4565-4573.
- Boss AP, 2003 The Solar Nebula. *Treatise on Geochemistry* **1**: 63-82.
- Burnett D, Barraclough B, Bennett R, Neugebauer M, Oldham L, Sasaki C, Sevilla D, Smith N, Stansbery E, Sweetnam D, Wiens R, 2003 The Genesis Discovery Mission: Return of Solar Matter to Earth. *Space Science Reviews* **105**: 509-534.
- Cargill PJ, Klimchuk JA, 2004 Nanoflare Heating of the Corona Revisited. *Astrophysical Journal* **605**: 911-920.
- Carslaw HS, Jaeger JC, 1959 *Conduction of heat in solids*. Clarendon Press.
- Cerutti H, 1974 Die Bestimmung des Argons im Sonnenwind aus Messungen an den Apollo-SWC-Folien, *PhD thesis*, University of Bern.
- Charbit S, Guillou H, Turpin L, 1998 Cross calibration of K-Ar standard minerals using an unspiked Ar measurement technique. *Chemical Geology* **150**: 147-159.
- Crank J, 1979 *The mathematics of diffusion*. Oxford University Press.
- Cranmer SR, Field GB, Kohl JL, 1999 Spectroscopic Constraints on Models of Ion Cyclotron Resonance Heating in the Polar Solar Corona and High-Speed Solar Wind. *Astrophysical Journal* **518**: 937-947.

- Delaboudinière J, Artzner GE, Brunaud J, Gabriel AH, Hochedez JF, Millier F, Song XY, Au B, Dere KP, Howard RA, Kreplin R, Michels DJ, Moses JD, Defise JM, Jamar C, Rochus P, Chauvineau JP, Marioge JP, Catura RC, Lemen JR, Shing L, Stern RA, Gurman JB, Neupert WM, Maucherat A, Clette F, Cugnon P, van Dessel EL, 1995 EIT: Extreme-Ultraviolet Imaging Telescope for the SOHO Mission. *Solar Physics* **162**: 291-312.
- Domingo V, Fleck B, Poland AI, 1995 The SOHO Mission: an Overview. *Solar Physics* **162**: 1-2.
- Drozd RJ, 1974 Xenon in lunar and terrestrial samples. *PhD thesis*, Washington University in St. Louis.
- Eberhardt P, Eugster O, Marti K, 1965 A Redetermination of the Isotopic Composition of Atmospheric Neon A. *Z. Naturforsch* **20a**.
- Fechtig H, Kalbitzer S, 1966 The diffusion of argon in potassium-bearing solids. In: *Potassium argon dating*, Zaehring J, Schaeffer OA (eds), Springer-Verlag, pp. 68-106.
- Fisk LA, Schwadron NA, Zurbuchen TH, 1998 On the Slow Solar Wind. *Space Science Reviews* **86**: 51-60.
- Geiss J, Bochsler P, 1985 Ion composition in the solar wind in relation to solar abundances. In: *Isotopic Ratios in the Solar System*, pp. 213-228.
- Geiss J, Buehler F, Cerutti H, Eberhardt P, Filleux C, 1972 Solar Wind Composition Experiment. *NASA Special Publication* **315**: 141.
- Geiss J, Eberhardt P, Signer P, Buehler F, Meister J, 1969 The Solar-Wind Composition Experiment. *NASA Special Publication* **214**: 183.
- Geiss J, Gloeckler G, Steiger R, 1995 Origin of the solar wind from composition data. *Space Science Reviews* **72**: 49-60.
- Geiss J, Bühler F, Cerutti H, Eberhardt P, Filleux C, Meister J, Signer P, 2004 The Apollo SWC Experiment: Results, Conclusions, Consequences. *Space Science Reviews* **110**: 307-335.
- Geiss J, Hirt P, Leutwyler H, 1970 On Acceleration and Motion of Ions in Corona and Solar Wind. *Solar Physics* **12**: 458-483.
- Gloeckler G, Cain J, Ipavich FM, Tums EO, Bedini P, Fisk LA, Zurbuchen TH, Bochsler P, Fischer J, Wimmer-Schweingruber RF, Geiss J, Kallenbach R, 1998

- Investigation of the composition of solar and interstellar matter using solar wind and pickup ion measurements with SWICS and SWIMS on the ACE spacecraft. *Space Science Reviews* **86**: 497-539.
- Grimberg A, Baur H, Bochsler P, Buhler F, Burnett DS, Hays CC, Heber VS, Jurewicz AJG, Wieler R, 2006 Solar Wind Neon from Genesis: Implications for the Lunar Noble Gas Record. *Science* **314**: 1133-1135.
- Hall DNB, 1975 Spectroscopic detection of solar He-3. *Astrophysical Journal* **197**: 509-512.
- Hall DNB, Engvold O, 1975 A reduced upper limit to the solar boron abundance. *Astrophysical Journal* **197**: 513-515.
- Hall DNB, 1973 Detection of the 13C, 17O, and 16O Isotope Bands of CO in the Infrared Solar Spectrum. *Astrophysical Journal* **182**: 977-982.
- Heber VS, Wiens RC, Bochsler P, Wieler R, Burnett DS, 2009 Fractionation Processes in the Solar Wind Revealed by Noble Gases Collected by Genesis Regime Targets. *Proc. of the Lunar and Planetary Science Conference* **37**: 2503.
- Hofker WK, 1975 Implantation of boron in silicon. *PhD thesis*, Eindhoven Univ. Technol., Netherlands.
- Hohenberg CM, 1980 High sensitivity pulse-counting mass spectrometer system for noble gas analysis. *Review of Scientific Instruments* **51**: 1075-1082.
- Hohenberg CM, Davis PK, Kaiser WA, Lewis RS, Reynolds JH, 1970 Trapped and cosmogenic rare gases from stepwise heating of Apollo 11 samples. *Geochimica et Cosmochimica Acta Supplement* **1**: 1283.
- Hovestadt D, Hilchenbach M, Bürgi A, Klecker B, Laeverenz P, Scholer M, Grünwaldt H, Axford WI, Livi S, Marsch E, Wilken B, Winterhoff HP, Ipavich FM, Bedini P, Coplan MA, Galvin AB, Gloeckler G, Bochsler P, Balsiger H, Fischer J, Geiss J, Kallenbach R, Wurz P, Reiche K, Gliem F, Judge DL, Ogawa HS, Hsieh KC, Möbius E, Lee MA, Managadze GG, Verigin MI, Neugebauer M, 1995 CELIAS - Charge, Element and Isotope Analysis System for SOHO. *Solar Physics* **162**: 441-481.
- Hudson GB, 1981 Noble Gas Retention Chronologies for the St. Severin Meteorite. *PhD thesis*, Washington University in St. Louis.
- Hudson H, Bougeret J, Burkepile J, 2006 Coronal Mass Ejections: Overview of Observations. *Space Science Reviews* **123**: 13-30.

- Jain SC, 1958 Simple Solutions of the Partial Differential Equation for Diffusion (or Heat Conduction). *Proceedings of the Royal Society of London. Series A, Mathematical and Physical Sciences* **243**: 359-374.
- Jost W, 1960 *Diffusion in Solids, Liquids, Gases*. Academic Press, New York.
- Jurewicz A, Burnett D, Wiens R, Friedmann T, Hays C, Hohlfelder R, Nishiizumi K, Stone J, Woolum D, Becker R, Butterworth A, Campbell A, Ebihara M, Franchi I, Heber V, Hohenberg C, Humayun M, McKeegan K, McNamara K, Meshik A, Pepin R, Schlutter D, Wieler R, 2003 The Genesis Solar-Wind Collector Materials. *Space Science Reviews* **105**: 535-560.
- Kallenbach R, Ipavich FM, Bochsler P, Hefti S, Hovestadt D, Grünwaldt H, Hilchenbach M, Axford WI, Balsiger H, Bürgi A, Coplan MA, Galvin AB, Geiss J, Gliem F, Gloeckler G, Hsieh KC, Klecker B, Lee MA, Livi S, Managadze GG, Marsch E, Möbius E, Neugebauer M, Reiche K, Scholer M, Verigin MI, Wilken B, Wurz P, 1997 Isotopic composition of solar wind neon measured by CELIAS/MTOF on board SOHO. **102**: 26,895-26,904.
- Kehm K, 2000 Laser Probe Noble Gas Studies of Individual Interplanetary Dust Particles Collected in the Earth's Stratosphere. *PhD thesis*, Washington University in St. Louis.
- Lee J, Marti K, Severinghaus JP, Kawamura K, Yoo H, Lee JB, Kim JS, 2006 A redetermination of the isotopic abundances of atmospheric Ar. *Geochimica et Cosmochimica Acta* **70**: 4507-4512.
- Leske RA, Mewaldt RA, Cohen CMS, Cummings AC, Stone EC, Wiedenbeck ME, von Rosenfing TT, 2007 Solar Isotopic Composition as Determined Using Solar Energetic Particles. *Space Science Reviews* **130**: 195-205.
- Lodders K, 2003 Solar System Abundances and Condensation Temperatures of the Elements. *The Astrophysical Journal* **591**: 1220-1247.
- Mabry JC, Meshik AP, Hohenberg CM, Burnett DS, Allton JH, 2008 Light Noble Gas Diffusion in Genesis Samples. *Proc. of the Lunar and Planetary Science Conference* **36**: 2255.
- Mamyrin BA, Anufriev GS, Kamenskii IL, Tolstikhin IN, 1970 Determination of isotopic composition of atmospheric helium. *Geochemistry International* **7**: 498-505.
- Marsch E, von Steiger R, Bochsler P, 1995 Element fractionation by diffusion in the solar chromosphere. *Astronomy and Astrophysics* **301**: 261.

- Mason GM, Gold RE, Krimigis SM, Mazur JE, Andrews GB, Daley KA, Dwyer JR, Heuerman KF, James TL, Kennedy MJ, Lefevre T, Malcolm H, Tossman B, Walpole PH, 1998 The Ultra-Low-Energy Isotope Spectrometer (ULEIS) for the ACE spacecraft. *Space Science Reviews* **86**: 409-448.
- McComas D, Bame S, Barker P, Feldman W, Phillips J, Riley P, Griffee J, 1998 Solar Wind Electron Proton Alpha Monitor (SWEPAM) for the Advanced Composition Explorer. *Space Science Reviews* **86**: 563-612.
- McDougall I, Harrison TM, 1999 *Geochronology and Thermochronology by the $^{40}\text{Ar}/^{39}\text{Ar}$ Method*. Oxford University Press, USA.
- Meshik A, Marrocchi Y, Hohenberg C, Pravdivtseva O, Mabry J, Allton J, Bastien R, McNamara K, Stabsbery E, Burnett D, 2006 Solar Neon Released from Genesis Aluminum Collector During Stepped UV-Laser Extraction and Step-wise Pyrolysis. *Meteoritics and Planetary Science Supplement* **41**: 5083.
- Meshik AP, Hohenberg CM, Burnett DS, Woolum DS, Jurewicz AJG, 2000 Release Profile as an Indicator of Solar Wind Neon Loss from Genesis Collectors. *Meteoritics and Planetary Science Supplement* **35**: 109.
- Meshik AP, Marrocchi Y, Hohenberg CM, Pravdivtseva OV, Mabry JC, Olinger C, Burnett DS, Allton JH, Bastien R, McNamara KM, Stansbery EK, 2006 Measurements of Light Noble Gases in the Genesis Polished Aluminum Collector. *Proc. of the Lunar and Planetary Science Conference* **37**: 2433.
- Meshik A, Mabry J, Hohenberg C, Marrocchi Y, Pravdivtseva O, Burnett D, Olinger C, Wiens R, Reisenfeld D, Allton J, McNamara K, Stansbery E, Jurewicz AJG, 2007 Constraints on Neon and Argon Isotopic Fractionation in Solar Wind. *Science* **318**: 433.
- Meyer-Vernet N, 2007 *Basics of the solar wind*. Cambridge University Press.
- Moore RL, Suess ST, Musielak ZE, An C, 1991 Alfvén wave trapping, network microflaring, and heating in solar coronal holes. *Astrophysical Journal* **378**: 347-359.
- Neugebauer M, 1991 The Quasi-Stationary and Transient States of the Solar Wind. *Science* **252**: 404-409.
- Neugebauer M, Steinberg J, Tokar R, Barraclough B, Dors E, Wiens R, Gingerich D, Luckey D, Whiteaker D, 2003 Genesis on-board determination of the solar wind flow regime. *Space Science Reviews* **105**: 661-679.

- Neugebauer M, Snyder CW, 1962 Solar Plasma Experiment. *Science* **138**: 1095-1097.
- Nichols RH, 1992 The Origin of Neon-E: Neon-E in Single Interstellar Silicon Carbide and Graphite Grains. *PhD thesis*, Washington University in St. Louis.
- Ozima M, Wieler R, Marty B, Podosek FA, 1998 Comparative Studies of Solar, Q-Gases and Terrestrial Noble Gases, and Implications on the Evolution of the Solar Nebula. *Geochimica et Cosmochimica Acta* **62**: 301-314.
- Ozima M, Podosek FA, 2001 *Noble Gas Geochemistry*. Cambridge University Press.
- Palma RL, Becker RH, Pepin RO, Schlutter DJ, 2002 Irradiation records in regolith materials, II: Solar wind and solar energetic particle components in helium, neon, and argon extracted from single lunar mineral grains and from the Kapoeta howardite by stepwise pulse heating. *Geochimica et Cosmochimica Acta* **66**: 2929-2958.
- Parker EN, 1958 Dynamics of the Interplanetary Gas and Magnetic Fields. *Astrophysical Journal* **128**: 664.
- Parker EN, 1960 The Hydrodynamic Theory of Solar Corpuscular Radiation and Stellar Winds. *Astrophysical Journal* **132**: 821.
- Parker EN, 1987 Magnetic reorientation and spontaneous formation of tangential discontinuities in deformed magnetic fields. *Astrophysical Journal* **318**: 876-887.
- Pepin RO, 1991 On the origin and early evolution of terrestrial planet atmospheres and meteoritic volatiles. *Icarus* **92**: 2-79.
- Pepin RO, Becker RH, Schlutter DJ, 1999 Irradiation records in regolith materials. I: isotopic compositions of solar-wind neon and argon in single lunar mineral grains. *Geochimica et Cosmochimica Acta* **63**: 2145-2162.
- Pepin RO, Nyquist LE, Phinney D, Black DC, 1970 Rare gases in Apollo 11 lunar material. *Geochimica et Cosmochimica Acta Supplement* **1**: 1435.
- Pepin RO, Nyquist LE, Phinney D, Black DC, 1970 Isotopic Composition of Rare Gases in Lunar Samples. *Science* **167**: 550-553.
- Pepin RO, 2006 Atmospheres on the terrestrial planets: Clues to origin and evolution. *Earth and Planetary Science Letters* **252**: 1-14.
- Reisenfeld D, Burnett D, Becker R, Grimberg A, Heber V, Hohenberg C, Jurewicz A,

- Meshik A, Pepin R, Raines J, Schlutter D, Wieler R, Wiens R, Zurbuchen T, 2007 Elemental Abundances of the Bulk Solar Wind: Analyses from Genesis and ACE. *Space Science Reviews* **130**: 79-86.
- Reisenfeld DB, Wiens RC, Barraclough BL, Steinberg JE, Dekoning C, Zurbuchen TH, Burnett DS, 2005 The GENESIS Mission Solar Wind Samples: Collection Times, Estimated Fluences, and Solar-Wind Conditions. *Proc. of the Lunar and Planetary Science Conference* **33**: 1278.
- Signer P, Eberhardt P, Geiss J, 1965 Possible Determination of the Solar Wind Composition. *Journal of Geophysical Research* **70**: 2243-2244.
- Smith CW, L'Heureux J, Ness NF, Acuña MH, Burlaga LF, Scheifele J, 1998 The ACE Magnetic Fields Experiment. *Space Science Reviews* **86**: 613-632.
- Stansbery EK, The Genesis Recovery Processing Team, 2005 Genesis Recovery Processing. *Proc. of the Lunar and Planetary Science Conference* **33**: 2179.
- von Steiger R, 1998 Composition Aspects of the Upper Solar Atmosphere Rapporteur Paper III. *Space Science Reviews* **85**: 407-418.
- von Steiger R, Geiss J, 1989 Supply of fractionated gases to the corona. *Astronomy and Astrophysics* **225**: 222-238.
- von Steiger R, Vial J, Bochsler P, Chaussidon M, Cohen CMS, Fleck B, Heber VS, Holweger H, Issautier K, Lazarus AJ, Ogilvie KW, Paquette JA, Reisenfeld DB, Teriaca L, Wilhelm K, Yusainee S, Laming JM, Wiens RC, 2001 Measuring Solar Abundances. *Joint SOHO/ACE workshop "Solar and Galactic Composition"*, **598**:13-22.
- Swindle TD, 1986 Iodine-xenon and other noble gas studies of individual chondrules from the Chainpur meteorite. *PhD thesis*, Washington University in St. Louis.
- Tasch AF, Shin H, Park C, Alvis J, Novak S, 1989 An Improved Approach to Accurately Model Shallow B and BF₂ Implants in Silicon. *Journal of The Electrochemical Society* **136**: 810-814.
- Tomczyk S, McIntosh SW, 2009 Time-Distance Seismology of the Solar Corona with CoMP. *Astrophysical Journal* **697**: 1384-1391.
- Verniani F, 1966 The Total Mass of the Earth's Atmosphere. *Journal of Geophysical Research* **71**: 385.
- Weygand JM, Ipavich FM, Wurz P, Paquette JA, Bochsler P, 2001 Determination of the

$^{36}\text{Ar}/^{38}\text{Ar}$ isotopic abundance ratio of the solar wind using SOHO/CELIAS/MTOF. *Geochimica et Cosmochimica Acta* **65**: 4589-4596.

Wieler R, 2002 Noble Gases in the Solar System. *Reviews in Mineralogy and Geochemistry* **47**: 21-70.

Wiens RC, Bochsler P, Burnett DS, Wimmer-Schweingruber RF, 2004 Solar and solar wind isotopic compositions. *Earth and Planetary Science Letters* **226**: 549-565.

Woolfson M, 2000 The origin and evolution of the solar system. *Astronomy & Geophysics* **41**: 1.12-1.19.

Ziegler JF, 2004 SRIM-2003. *Nuclear Instruments and Methods in Physics Research Section B: Beam Interactions with Materials and Atoms* **219-220**: 1027-1036.

Zurbuchen TH, Fisk LA, Gloeckler G, von Steiger R, 2002 The solar wind composition throughout the solar cycle: A continuum of dynamic states. *Geophysical Research Letters* **29**: 66-1.

Appendix A: Data Tables

Helium, neon, and argon step-wise heating data from the long term diffusion experiment. The raw helium data is included on the left side of the helium table; the right side has the data corrected for high-pressure effects, corrected data are shown in italics, and the final row has the backscatter corrected $^3\text{He}/^4\text{He}$. The argon data is shown before and after subtraction of atmospheric argon based on the amount of ^{40}Ar . Data which are crossed out are attributed to blank and not included in the total. All data are corrected for mass discrimination and isobaric interferences. All errors are 1σ statistical uncertainties.

1. A70 – unbaked AloS, 12.22 mm²

Temp (°C)	Helium – uncorrected		Corrected	
	^4He ($\times 10^{-7} \text{ cm}^3\text{STP}$)	$^3\text{He}/^4\text{He}$ ($\times 10^{-4}$)	^4He ($\times 10^{-7} \text{ cm}^3\text{STP}$)	$^3\text{He}/^4\text{He}$ ($\times 10^{-4}$)
200	0.2032 ± 0.0001	6.7835 ± 0.0007	0.2032 ± 0.0001	6.214 ± 0.091
300	1.8216 ± 0.0012	6.7098 ± 0.0007	<i>1.806 ± 0.010</i>	<i>6.200 ± 0.111</i>
350	2.2378 ± 0.0019	6.4550 ± 0.0007	<i>2.205 ± 0.013</i>	<i>6.001 ± 0.108</i>
400	2.5191 ± 0.0019	5.9021 ± 0.0006	<i>2.470 ± 0.014</i>	<i>5.514 ± 0.099</i>
450	2.4020 ± 0.0020	5.4849 ± 0.0006	<i>2.355 ± 0.014</i>	<i>5.124 ± 0.092</i>
475	1.7504 ± 0.0015	5.2276 ± 0.0005	<i>1.733 ± 0.010</i>	<i>4.836 ± 0.088</i>
500	1.8125 ± 0.0022	4.8264 ± 0.0005	<i>1.791 ± 0.011</i>	<i>4.474 ± 0.081</i>
525	1.8970 ± 0.0011	4.6099 ± 0.0005	<i>1.870 ± 0.010</i>	<i>4.283 ± 0.077</i>
550	1.3334 ± 0.0004	4.4989 ± 0.0005	<i>1.333 ± 0.007</i>	<i>4.123 ± 0.075</i>
600	3.6657 ± 0.0046	4.2890 ± 0.0004	<i>3.514 ± 0.022</i>	<i>4.098 ± 0.073</i>
650	14.386 ± 0.034	3.7256 ± 0.0004	<i>13.043 ± 0.099</i>	<i>3.764 ± 0.065</i>
700	0.3514 ± 0.0003	3.8092 ± 0.0004	0.3514 ± 0.0003	3.489 ± 0.052
750	0.0666 ± 0.00004	3.9128 ± 0.0005	0.0666 ± 0.00004	3.584 ± 0.060
800	0.0813 ± 0.0001	3.9151 ± 0.0006	0.0813 ± 0.0001	3.586 ± 0.068
850	0.08082 ± 0.00005	3.9073 ± 0.0007	0.08082 ± 0.00005	3.579 ± 0.073
Total	34.6091 ± 0.0344	4.6313 ± 0.0002	32.905 ± 0.199	4.462 ± 0.048
			Backscatter corrected	4.524 ± 0.048

Temp (°C)	Neon		
	^{20}Ne ($\times 10^{-11} \text{ cm}^3\text{STP}$)	$^{20}\text{Ne}/^{22}\text{Ne}$	$^{21}\text{Ne}/^{20}\text{Ne}$ ($\times 10^{-3}$)
200	1.12 ± 0.02	15.325 ± 1.805	2.82 ± 0.37
300	1.82 ± 0.02	15.903 ± 1.528	2.68 ± 0.22
350	1.89 ± 0.02	15.729 ± 1.528	2.78 ± 0.22
400	3.23 ± 0.03	14.817 ± 0.816	2.68 ± 0.14
450	6.07 ± 0.04	14.420 ± 0.427	2.31 ± 0.08
475	5.52 ± 0.05	14.234 ± 0.438	2.52 ± 0.11
500	7.55 ± 0.04	14.239 ± 0.302	2.40 ± 0.11
525	13.62 ± 0.06	14.281 ± 0.190	2.19 ± 0.08
550	22.95 ± 0.06	14.366 ± 0.124	2.38 ± 0.06
600	135.5 ± 0.3	14.219 ± 0.034	2.35 ± 0.02
650	357.4 ± 0.6	13.459 ± 0.020	2.402 ± 0.014
700	18.59 ± 0.07	13.697 ± 0.114	2.43 ± 0.05
750	2.73 ± 0.03	13.978 ± 0.676	2.94 ± 0.18
800	3.56 ± 0.03	13.960 ± 0.516	2.62 ± 0.14
850	4.43 ± 0.03	13.252 ± 0.374	2.62 ± 0.14
Total	585.9 ± 0.7	13.742 ± 0.019	2.394 ± 0.011

Temp (°C)	Measured Argon		^{40}Ar subtracted	
	$^{40}\text{Ar}/^{36}\text{Ar}$	$^{36}\text{Ar}/^{38}\text{Ar}$	^{36}Ar ($\times 10^{-13} \text{ cm}^3\text{STP}$)	$^{36}\text{Ar}/^{38}\text{Ar}$
200	273.6 ± 2.9	5.36 ± 0.18	0.98 ± 0.13	3.82 ± 0.65
300	264.8 ± 2.7	5.19 ± 0.18	1.39 ± 0.13	4.01 ± 0.53
350	259.5 ± 3.1	5.47 ± 0.22	1.34 ± 0.10	4.70 ± 0.75
400	253.3 ± 2.3	5.44 ± 0.25	1.34 ± 0.08	5.78 ± 0.92
450	246.9 ± 2.6	5.91 ± 0.20	1.96 ± 0.10	4.60 ± 0.55
475	245.3 ± 2.0	5.47 ± 0.22	1.90 ± 0.08	5.44 ± 0.60
500	223.4 ± 1.6	5.64 ± 0.25	3.11 ± 0.08	5.85 ± 0.50
525	195.7 ± 1.7	5.64 ± 0.18	5.33 ± 0.10	5.30 ± 0.26
550	188.7 ± 1.9	5.46 ± 0.16	5.64 ± 0.13	5.52 ± 0.26
600	81.8 ± 0.4	5.50 ± 0.11	26.7 ± 0.2	5.57 ± 0.08
650	4.325 ± 0.004	5.511 ± 0.023	806.1 ± 1.4	5.514 ± 0.011
700	69.3 ± 0.3	5.40 ± 0.10	47.9 ± 0.2	5.33 ± 0.06
750	197.0 ± 1.1	5.41 ± 0.16	6.25 ± 0.10	5.21 ± 0.22
800	216.0 ± 1.4	5.47 ± 0.16	6.46 ± 0.13	5.34 ± 0.29
850	239.9 ± 1.4	5.25 ± 0.05	7.46 ± 0.18	4.97 ± 0.26
Total	50.18 ± 0.14	5.491 ± 0.020	909.9 ± 1.5	5.496 ± 0.012

2. A63 – AloS unbaked, 8.55 mm²

Temp (°C)	Helium – uncorrected		Corrected	
	⁴ He (× 10 ⁻⁸ cm ³ STP)	³ He/ ⁴ He (× 10 ⁻⁴)	⁴ He (× 10 ⁻⁸ cm ³ STP)	³ He/ ⁴ He (× 10 ⁻⁴)
200	0.2253 ± 0.0004	6.777 ± 0.110	0.2253 ± 0.0004	6.208 ± 0.118
300	2.298 ± 0.001	6.236 ± 0.074	2.298 ± 0.001	5.712 ± 0.088
350	1.324 ± 0.002	5.193 ± 0.069	1.324 ± 0.002	4.757 ± 0.078
400	2.144 ± 0.001	5.013 ± 0.057	2.144 ± 0.001	4.592 ± 0.069
450	7.72 ± 0.01	5.431 ± 0.057	7.718 ± 0.007	4.975 ± 0.072
475	14.231 ± 0.004	5.318 ± 0.055	14.21 ± 0.08	4.877 ± 0.089
500	15.88 ± 0.01	4.885 ± 0.051	15.79 ± 0.09	4.499 ± 0.082
525	17.68 ± 0.02	4.533 ± 0.047	17.51 ± 0.11	4.194 ± 0.076
550	17.05 ± 0.01	4.337 ± 0.045	16.89 ± 0.10	4.008 ± 0.073
600	95.12 ± 0.12	3.850 ± 0.039	88.21 ± 0.57	3.803 ± 0.066
700	11.643 ± 0.003	3.728 ± 0.040	11.643 ± 0.003	3.415 ± 0.049
800	0.6095 ± 0.0005	3.453 ± 0.064	0.6095 ± 0.0005	3.163 ± 0.066
Total	185.9 ± 0.1	4.273 ± 0.022	166.3 ± 1.0	4.075 ± 0.051
Backscatter corrected				4.131 ± 0.051

Temp (°C)	Neon		
	²⁰ Ne (× 10 ⁻¹¹ cm ³ STP)	²⁰ Ne/ ²² Ne	²¹ Ne/ ²⁰ Ne (× 10 ⁻³)
200	0.39 ± 0.02	22.4 ± 8.3	3.598 ± 0.402
300	1.73 ± 0.02	14.993 ± 1.745	2.644 ± 0.230
350	1.88 ± 0.02	14.986 ± 1.633	2.632 ± 0.149
400	3.47 ± 0.03	14.756 ± 0.886	2.586 ± 0.147
450	5.99 ± 0.04	14.790 ± 0.601	2.535 ± 0.144
475	5.70 ± 0.04	14.306 ± 0.567	2.562 ± 0.135
500	7.14 ± 0.05	14.147 ± 0.450	2.389 ± 0.102
525	13.35 ± 0.08	14.288 ± 0.271	2.439 ± 0.074
550	25.83 ± 0.09	14.098 ± 0.155	2.312 ± 0.033
600	144.3 ± 0.4	13.763 ± 0.056	2.397 ± 0.038
700	180.2 ± 0.5	13.519 ± 0.035	2.422 ± 0.022
800	15.32 ± 0.07	13.213 ± 0.186	2.537 ± 0.071
Total	405.3 ± 0.6	13.720 ± 0.034	2.418 ± 0.018

Temp (°C)	Measured Argon		⁴⁰ Ar subtracted	
	⁴⁰ Ar/ ³⁶ Ar	³⁶ Ar/ ³⁸ Ar	³⁶ Ar (× 10 ⁻¹³ cm ³ STP)	³⁶ Ar/ ³⁸ Ar
200	286.8 ± 3.6	5.271 ± 0.119	0.31 ± 0.11	4.1 ± 2.4
300	283.4 ± 2.3	5.243 ± 0.072	0.90 ± 0.17	3.96 ± 1.00
350	283.6 ± 3.1	5.248 ± 0.094	0.76 ± 0.20	4.02 ± 1.35
400	277.6 ± 2.5	5.356 ± 0.085	1.15 ± 0.17	5.96 ± 1.70
450	273.6 ± 2.4	5.228 ± 0.082	1.35 ± 0.14	4.320 ± 0.752
475	269.9 ± 2.3	5.216 ± 0.084	1.66 ± 0.14	4.337 ± 0.668
500	261.7 ± 2.5	5.464 ± 0.093	1.71 ± 0.11	6.89 ± 1.30
525	247.2 ± 2.8	5.431 ± 0.115	2.61 ± 0.14	6.075 ± 0.877
550	226.0 ± 1.7	5.404 ± 0.085	3.99 ± 0.11	5.694 ± 0.401
600	23.6 ± 0.1	5.511 ± 0.027	161.7 ± 0.4	5.528 ± 0.029
700	49.5 ± 0.1	5.490 ± 0.017	425.9 ± 0.6	5.526 ± 0.021
800	154.4 ± 0.6	5.268 ± 0.058	31.50 ± 0.20	5.212 ± 0.119
Total	88.7 ± 0.2	5.447 ± 0.013	602.0 ± 0.9	5.503 ± 0.019

3. A67 – AloS baked 240°C, 10.33 mm²

Temp (°C)	Helium – uncorrected		Corrected	
	⁴ He (× 10 ⁻⁸ cm ³ STP)	³ He/ ⁴ He (× 10 ⁻⁴)	⁴ He (× 10 ⁻⁸ cm ³ STP)	³ He/ ⁴ He (× 10 ⁻⁴)
200	0.0513 ± 0.0002	7.996 ± 0.272	0.0513 ± 0.0002	7.325 ± 0.259
300	0.2752 ± 0.0003	5.615 ± 0.118	0.2752 ± 0.0003	5.143 ± 0.143
350	0.4860 ± 0.0004	5.674 ± 0.091	0.4860 ± 0.0004	5.197 ± 0.121
400	1.917 ± 0.002	5.549 ± 0.061	1.917 ± 0.002	5.083 ± 0.096
450	12.87 ± 0.01	5.686 ± 0.058	12.87 ± 0.01	5.208 ± 0.095
475	18.09 ± 0.01	5.343 ± 0.055	17.92 ± 0.10	4.942 ± 0.089
500	19.81 ± 0.02	4.785 ± 0.049	19.53 ± 0.12	4.446 ± 0.080
525	17.99 ± 0.02	4.440 ± 0.045	17.78 ± 0.11	4.114 ± 0.074
550	12.71 ± 0.01	4.314 ± 0.045	12.711 ± 0.011	3.951 ± 0.072
600	25.40 ± 0.03	4.188 ± 0.043	24.73 ± 0.15	3.940 ± 0.070
700	106.3 ± 0.6	3.744 ± 0.038	97.8 ± 1.1	3.726 ± 0.065
800	0.2861 ± 0.0002	4.013 ± 0.103	0.2861 ± 0.0002	3.676 ± 0.101
Total	216.2 ± 0.6	4.256 ± 0.021	206.4 ± 1.6	4.084 ± 0.057
			Backscatter corrected	4.140 ± 0.057

Temp (°C)	Neon		
	^{20}Ne ($\times 10^{-11} \text{ cm}^3\text{STP}$)	$^{20}\text{Ne}/^{22}\text{Ne}$	$^{21}\text{Ne}/^{20}\text{Ne}$ ($\times 10^{-3}$)
200	0.22 ± 0.01	25.4 ± 12.6	5.42 ± 0.63
300	0.37 ± 0.02	30.3 ± 12.1	2.91 ± 0.47
350	0.47 ± 0.02	20.5 ± 6.5	2.48 ± 0.36
400	1.81 ± 0.03	14.81 ± 1.49	2.61 ± 0.18
450	4.70 ± 0.04	14.83 ± 0.70	2.59 ± 0.14
475	6.39 ± 0.03	14.59 ± 0.51	2.28 ± 0.10
500	11.92 ± 0.07	14.47 ± 0.29	2.39 ± 0.08
525	23.69 ± 0.08	14.525 ± 0.157	2.36 ± 0.06
550	45.2 ± 0.1	14.444 ± 0.091	2.35 ± 0.04
600	122.3 ± 0.4	14.277 ± 0.047	2.34 ± 0.02
700	251.6 ± 0.6	13.307 ± 0.033	2.40 ± 0.01
800	6.34 ± 0.04	13.309 ± 0.39	2.52 ± 0.10
Total	475.03 ± 0.74	13.786 ± 0.028	2.383 ± 0.012

Temp (°C)	Measured Argon		^{40}Ar subtracted	
	$^{40}\text{Ar}/^{36}\text{Ar}$	$^{36}\text{Ar}/^{38}\text{Ar}$	^{36}Ar ($\times 10^{-13} \text{ cm}^3\text{STP}$)	$^{36}\text{Ar}/^{38}\text{Ar}$
200	290.5 ± 2.2	5.24 ± 0.08	0.40 ± 0.17	2.89 ± 1.38
300	291.9 ± 2.2	5.19 ± 0.07	0.23 ± 0.11	1.90 ± 0.93
350	289.8 ± 3.6	5.13 ± 0.12	0.23 ± 0.14	1.92 ± 1.08
400	287.4 ± 2.5	5.17 ± 0.09	0.31 ± 0.08	2.66 ± 0.94
450	268.4 ± 3.7	5.45 ± 0.13	1.16 ± 0.14	7.21 ± 2.38
475	248.3 ± 2.1	5.36 ± 0.09	1.87 ± 0.08	5.56 ± 0.63
500	234.8 ± 2.6	5.16 ± 0.12	2.69 ± 0.11	4.64 ± 0.48
525	219.9 ± 2.5	5.26 ± 0.10	3.37 ± 0.11	5.09 ± 0.35
550	197.8 ± 1.6	5.31 ± 0.10	4.36 ± 0.08	5.29 ± 0.30
600	110.9 ± 0.5	5.35 ± 0.06	16.66 ± 0.08	5.36 ± 0.09
700	8.19 ± 0.02	5.534 ± 0.014	691.8 ± 1.5	5.540 ± 0.015
800	145.6 ± 0.7	5.30 ± 0.05	25.60 ± 0.17	5.27 ± 0.10
Total	52.84 ± 0.17	5.474 ± 0.012	723.0 ± 1.5	5.509 ± 0.016

4. A66 – AloS baked 280 °C, 13.43 mm²

Temp (°C)	Helium – uncorrected		Corrected	
	⁴ He (× 10 ⁻⁸ cm ³ STP)	³ He/ ⁴ He (× 10 ⁻⁴)	⁴ He (× 10 ⁻⁸ cm ³ STP)	³ He/ ⁴ He (× 10 ⁻⁴)
200	0.3299 ± 0.0003	4.986 ± 0.088	0.3299 ± 0.0003	4.567 ± 0.092
300	1.108 ± 0.001	5.116 ± 0.072	1.1083 ± 0.0008	4.686 ± 0.080
350	1.399 ± 0.001	5.553 ± 0.073	1.3991 ± 0.0006	5.086 ± 0.083
400	3.995 ± 0.001	5.478 ± 0.058	3.9953 ± 0.0009	5.018 ± 0.073
450	21.30 ± 0.03	5.410 ± 0.055	21.30 ± 0.03	4.956 ± 0.070
475	25.14 ± 0.02	5.053 ± 0.052	24.56 ± 0.14	4.737 ± 0.085
500	31.25 ± 0.06	4.626 ± 0.047	30.22 ± 0.22	4.382 ± 0.078
525	43.63 ± 0.06	4.200 ± 0.043	41.92 ± 0.27	4.003 ± 0.071
550	48.40 ± 0.20	3.963 ± 0.040	46.20 ± 0.43	3.803 ± 0.067
600	97.16 ± 0.14	3.555 ± 0.036	89.26 ± 0.59	3.545 ± 0.061
650	5.252 ± 0.003	3.685 ± 0.041	5.252 ± 0.003	3.375 ± 0.050
700	1.678 ± 0.001	3.644 ± 0.050	1.678 ± 0.001	3.338 ± 0.056
750	0.3177 ± 0.0003	4.030 ± 0.081	0.3177 ± 0.0003	3.691 ± 0.083
800	0.4724 ± 0.0003	4.018 ± 0.069	0.4724 ± 0.0003	3.681 ± 0.073
850	0.7483 ± 0.0003	3.863 ± 0.063	0.7483 ± 0.0003	3.538 ± 0.067
Total	282.2 ± 0.3	4.167 ± 0.018	268.8 ± 1.6	4.007 ± 0.049
			Backscatter corrected	4.063 ± 0.049

Temp (°C)	Neon		
	²⁰ Ne (× 10 ⁻¹¹ cm ³ STP)	²⁰ Ne/ ²² Ne	²¹ Ne/ ²⁰ Ne (× 10 ⁻³)
200	0.197 ± 0.009	27.3 ± 11.7	4.82 ± 0.60
300	0.362 ± 0.013	21.8 ± 6.1	4.04 ± 0.47
350	0.484 ± 0.012	19.48 ± 4.68	1.85 ± 0.41
400	1.27 ± 0.02	15.15 ± 1.46	2.55 ± 0.24
450	3.94 ± 0.03	14.458 ± 0.635	2.50 ± 0.14
475	6.01 ± 0.02	13.883 ± 0.393	2.61 ± 0.12
500	16.83 ± 0.04	14.001 ± 0.152	2.45 ± 0.06
525	193.17 ± 0.13	13.944 ± 0.035	2.37 ± 0.02
550	116.56 ± 0.19	13.480 ± 0.038	2.38 ± 0.02
600	225.31 ± 0.16	13.304 ± 0.027	2.41 ± 0.02
650	58.59 ± 0.05	13.997 ± 0.055	2.31 ± 0.04
700	23.31 ± 0.04	14.227 ± 0.110	2.38 ± 0.06
750	5.42 ± 0.04	14.373 ± 0.400	2.47 ± 0.13
800	6.30 ± 0.04	14.329 ± 0.324	2.53 ± 0.09
850	13.66 ± 0.05	14.212 ± 0.168	2.34 ± 0.07
Total	671.4 ± 0.3	13.681 ± 0.019	2.39 ± 0.01

Temp (°C)	Measured Argon		⁴⁰ Ar subtracted	
	⁴⁰ Ar/ ³⁶ Ar	³⁶ Ar/ ³⁸ Ar	³⁶ Ar (× 10 ⁻¹³ cm ³ STP)	³⁶ Ar/ ³⁸ Ar
200	293.4 ± 1.8	5.25 ± 0.07	0.10 ± 0.05	2.08 ± 1.6
300	292.8 ± 2.6	5.25 ± 0.10	0.05 ± 0.05	2.37 ± 2.2
350	289.0 ± 3.5	5.30 ± 0.13	0.04 ± 0.05	4.71 ± 4.5
400	288.7 ± 2.4	5.44 ± 0.13	0.004 ± 0.05	72.1 ± 1003.9
450	270.3 ± 3.2	5.42 ± 0.13	0.11 ± 0.05	6.69 ± 2.4
475	252.9 ± 3.0	5.36 ± 0.10	0.29 ± 0.05	5.63 ± 0.8
500	183.1 ± 1.8	5.39 ± 0.09	0.98 ± 0.05	5.52 ± 0.2
525	51.06 ± 0.19	5.55 ± 0.05	8.44 ± 0.08	5.601 ± 0.060
550	16.74 ± 0.03	5.56 ± 0.02	34.27 ± 0.13	5.572 ± 0.022
600	4.91 ± 0.01	5.475 ± 0.018	111.4 ± 0.4	5.478 ± 0.018
650	20.90 ± 0.06	5.48 ± 0.03	28.15 ± 0.15	5.493 ± 0.032
700	89.42 ± 0.42	5.46 ± 0.04	7.35 ± 0.08	5.52 ± 0.06
750	179.8 ± 1.3	5.37 ± 0.08	1.47 ± 0.05	5.46 ± 0.22
800	156.5 ± 1.0	5.30 ± 0.07	2.42 ± 0.05	5.28 ± 0.14
850	120.6 ± 0.5	5.42 ± 0.04	6.74 ± 0.08	5.49 ± 0.08
Total	43.60 ± 0.11	5.473 ± 0.010	191.24 ± 0.46	5.503 ± 0.013

5. A68 – AloS baked 320 °C, 7.27 mm²

Temp (°C)	Helium – uncorrected		Corrected	
	⁴ He (× 10 ⁻⁸ cm ³ STP)	³ He/ ⁴ He (× 10 ⁻⁴)	⁴ He (× 10 ⁻⁸ cm ³ STP)	³ He/ ⁴ He (× 10 ⁻⁴)
200	0.0219 ± 0.0001	11.31 ± 0.46	0.0219 ± 0.0001	10.4 ± 0.4
300	0.0954 ± 0.0003	6.18 ± 0.20	0.0954 ± 0.0003	5.7 ± 0.2
350	0.2904 ± 0.0002	5.560 ± 0.092	0.2904 ± 0.0002	5.1 ± 0.1
400	0.994 ± 0.001	5.185 ± 0.063	0.994 ± 0.001	4.75 ± 0.07
450	4.043 ± 0.002	5.317 ± 0.060	4.043 ± 0.002	4.87 ± 0.07
475	6.153 ± 0.003	5.200 ± 0.055	6.153 ± 0.003	4.763 ± 0.088
500	7.286 ± 0.042	4.886 ± 0.050	7.286 ± 0.042	4.476 ± 0.081
525	9.016 ± 0.004	4.644 ± 0.048	9.016 ± 0.004	4.254 ± 0.078
550	7.843 ± 0.003	4.535 ± 0.048	7.843 ± 0.003	4.154 ± 0.077
600	20.05 ± 0.01	4.335 ± 0.044	19.72 ± 0.11	4.039 ± 0.073
650	78.27 ± 0.38	3.757 ± 0.038	72.98 ± 0.75	3.691 ± 0.064
700	2.599 ± 0.001	3.690 ± 0.045	2.599 ± 0.001	3.380 ± 0.053
750	0.4605 ± 0.0003	4.035 ± 0.061	0.4605 ± 0.0003	3.696 ± 0.066
800	0.3340 ± 0.0002	4.115 ± 0.084	0.3340 ± 0.0002	3.769 ± 0.085
Total	137.5 ± 0.4	4.132 ± 0.023	131.8 ± 1.0	3.946 ± 0.055
			Backscatter corrected	4.001 ± 0.055

Temp (°C)	Neon		
	²⁰ Ne (× 10 ⁻¹¹ cm ³ STP)	²⁰ Ne/ ²² Ne	²¹ Ne/ ²⁰ Ne (× 10 ⁻³)
200	0.050 ± 0.008	33 ± 26	5.57 ± 0.99
300	0.098 ± 0.010	54 ± 63	4.37 ± 0.74
350	0.099 ± 0.011	23 ± 16	3.65 ± 0.59
400	0.296 ± 0.012	25 ± 10	1.82 ± 0.53
450	1.00 ± 0.02	14.9 ± 2.2	3.03 ± 0.33
475	1.59 ± 0.03	14.5 ± 1.4	2.63 ± 0.17
500	2.98 ± 0.03	14.3 ± 0.7	2.29 ± 0.14
525	6.52 ± 0.04	14.23 ± 0.38	2.33 ± 0.12
550	16.94 ± 0.03	14.06 ± 0.15	2.310 ± 0.066
600	103.9 ± 0.1	14.020 ± 0.050	2.314 ± 0.027
650	171.0 ± 0.4	13.386 ± 0.032	2.420 ± 0.017
700	12.42 ± 0.03	13.66 ± 0.17	2.453 ± 0.088
750	2.21 ± 0.03	13.91 ± 0.83	2.69 ± 0.21
800	1.89 ± 0.02	14.03 ± 0.97	3.10 ± 0.23
Total	321.0 ± 0.4	13.684 ± 0.030	2.387 ± 0.014

Temp (°C)	Measured Argon		⁴⁰ Ar subtracted	
	⁴⁰ Ar/ ³⁶ Ar	³⁶ Ar/ ³⁸ Ar	³⁶ Ar (× 10 ⁻¹³ cm ³ STP)	³⁶ Ar/ ³⁸ Ar
200	290.7 ± 3.7	5.24 ± 0.11	0.18 ± 0.13	2.82 ± 1.96
300	289.1 ± 2.2	5.30 ± 0.08	0.36 ± 0.13	4.45 ± 2.50
350	295.2 ± 3.4	5.24 ± 0.11	0.03 ± 0.08	0.85 ± ***
400	289.3 ± 3.8	5.20 ± 0.14	0.21 ± 0.10	2.67 ± 1.74
450	278.1 ± 2.7	5.31 ± 0.13	0.54 ± 0.08	5.18 ± 2.10
475	273.7 ± 3.1	5.28 ± 0.13	0.67 ± 0.10	4.87 ± 1.48
500	268.5 ± 3.3	5.16 ± 0.10	1.11 ± 0.13	3.97 ± 0.69
525	218.9 ± 2.9	5.54 ± 0.13	2.89 ± 0.10	6.27 ± 0.63
550	181.7 ± 1.5	5.68 ± 0.10	5.34 ± 0.08	6.36 ± 0.32
600	55.92 ± 0.19	5.54 ± 0.04	61.38 ± 0.23	5.60 ± 0.05
650	13.31 ± 0.02	5.516 ± 0.016	459.7 ± 0.9	5.526 ± 0.017
700	140.53 ± 0.62	5.30 ± 0.04	28.28 ± 0.18	5.28 ± 0.08
750	237.7 ± 1.6	5.30 ± 0.06	5.86 ± 0.15	5.21 ± 0.32
800	233.9 ± 1.4	5.21 ± 0.06	5.50 ± 0.13	4.83 ± 0.26
Total	74.30 ± 0.20	5.460 ± 0.013	560.6 ± 1.0	5.519 ± 0.018

6. A71 – AloS baked 360 °C, 4.77 mm²

Temp (°C)	Helium – uncorrected		Corrected	
	⁴ He (× 10 ⁻⁸ cm ³ STP)	³ He/ ⁴ He (× 10 ⁻⁴)	⁴ He (× 10 ⁻⁸ cm ³ STP)	³ He/ ⁴ He (× 10 ⁻⁴)
200	0.0271 ± 0.0001	8.098 ± 0.397	0.0271 ± 0.0001	7.418 ± 0.371
300	0.0665 ± 0.0001	6.231 ± 0.235	0.0665 ± 0.0001	5.707 ± 0.222
350	0.1597 ± 0.0002	5.182 ± 0.119	0.1597 ± 0.0002	4.746 ± 0.119
400	1.108 ± 0.001	4.872 ± 0.065	1.108 ± 0.001	4.463 ± 0.074
475	5.294 ± 0.002	4.825 ± 0.053	5.294 ± 0.002	4.420 ± 0.065
500	4.657 ± 0.003	4.633 ± 0.050	4.657 ± 0.003	4.244 ± 0.062
525	6.558 ± 0.002	4.486 ± 0.049	6.558 ± 0.002	4.109 ± 0.060
550	9.960 ± 0.007	4.340 ± 0.046	9.960 ± 0.007	3.975 ± 0.058
600	56.99 ± 0.24	3.867 ± 0.039	54.04 ± 0.52	3.735 ± 0.066
650	2.145 ± 0.002	3.781 ± 0.047	2.145 ± 0.002	3.464 ± 0.055
700	0.3786 ± 0.0005	4.273 ± 0.085	0.3786 ± 0.0005	3.914 ± 0.087
750	0.3848 ± 0.0002	4.178 ± 0.080	0.3848 ± 0.0002	3.827 ± 0.082
800	0.8555 ± 0.0012	3.724 ± 0.053	0.8555 ± 0.0012	3.411 ± 0.059
Total	88.58 ± 0.24	4.081 ± 0.026	84.40 ± 0.67	3.867 ± 0.045
			Backscatter corrected	3.920 ± 0.045

Temp (°C)	Neon		
	²⁰ Ne (× 10 ⁻¹¹ cm ³ STP)	²⁰ Ne/ ²² Ne	²¹ Ne/ ²⁰ Ne (× 10 ⁻³)
200	0.09 ± 0.01	23 ± 13	2.61 ± 0.78
300	0.10 ± 0.01	94 ± 138	6.52 ± 1.02
350	0.12 ± 0.01	47 ± 36	5.59 ± 0.93
400	0.34 ± 0.02	18 ± 6	3.17 ± 0.45
475	1.45 ± 0.02	14.5 ± 1.5	2.82 ± 0.24
500	2.38 ± 0.03	14.2 ± 0.9	2.63 ± 0.20
525	8.81 ± 0.06	13.9 ± 0.3	2.42 ± 0.09
550	32.28 ± 0.05	13.91 ± 0.09	2.37 ± 0.05
600	159.3 ± 0.2	13.485 ± 0.035	2.394 ± 0.023
650	21.56 ± 0.08	13.65 ± 0.11	2.38 ± 0.06
700	3.53 ± 0.03	13.60 ± 0.63	2.56 ± 0.10
750	2.25 ± 0.03	12.94 ± 0.75	2.61 ± 0.18
800	5.92 ± 0.05	12.69 ± 0.32	2.62 ± 0.11
850	5.64 ± 0.03	12.95 ± 0.38	2.69 ± 0.11
Total	232.2 ± 0.3	13.561 ± 0.036	2.417 ± 0.018

Temp (°C)	Measured Argon		⁴⁰ Ar subtracted	
	⁴⁰ Ar/ ³⁶ Ar	³⁶ Ar/ ³⁸ Ar	³⁶ Ar (× 10 ⁻¹⁴ cm ³ STP)	³⁶ Ar/ ³⁸ Ar
200	292.1 ± 3.3	5.38 ± 0.09	2.1 ± 1.8	26.9 ± 198.2
300	291.4 ± 3.4	5.09 ± 0.11	1.6 ± 1.0	1.4 ± 0.9
350	289.5 ± 3.2	5.27 ± 0.11	2.3 ± 1.3	3.8 ± 0.8
400	290.4 ± 2.8	5.38 ± 0.10	2.1 ± 1.0	12.8 ± 32.3
475	281.0 ± 2.6	5.33 ± 0.10	5.7 ± 1.0	5.6 ± 2.2
500	264.1 ± 3.8	5.33 ± 0.12	9.6 ± 1.0	5.5 ± 1.2
525	224.1 ± 2.5	5.31 ± 0.11	28.4 ± 1.0	5.29 ± 0.44
550	136.7 ± 1.1	5.34 ± 0.07	108.1 ± 1.0	5.35 ± 0.14
600	15.67 ± 0.04	5.501 ± 0.025	3032 ± 9	5.512 ± 0.026
650	91.31 ± 0.30	5.419 ± 0.033	599.9 ± 2.3	5.464 ± 0.049
700	243.1 ± 1.4	5.20 ± 0.06	69.7 ± 1.8	4.71 ± 0.27
750	263.5 ± 1.3	5.20 ± 0.04	74.3 ± 3.1	4.37 ± 0.27
800	282.6 ± 0.6	5.17 ± 0.02	149.6 ± 7.0	3.29 ± 0.24
Total	167.7 ± 0.3	5.321 ± 0.013	3791.6 ± 12.1	5.493 ± 0.036

7. PSE – unbaked PAC, 8.3 mm²

Temp (°C)	Helium – uncorrected		Corrected	
	⁴ He (× 10 ⁻⁸ cm ³ STP)	³ He/ ⁴ He (× 10 ⁻⁴)	⁴ He (× 10 ⁻⁸ cm ³ STP)	³ He/ ⁴ He (× 10 ⁻⁴)
200	0.834 ± 0.001	6.696 ± 0.084	0.834 ± 0.001	6.133 ± 0.097
300	16.07 ± 0.02	6.042 ± 0.062	15.98 ± 0.10	5.565 ± 0.101
350	17.89 ± 0.01	5.595 ± 0.057	17.72 ± 0.10	5.174 ± 0.093
400	24.47 ± 0.01	5.059 ± 0.051	23.95 ± 0.13	4.735 ± 0.085
450	40.22 ± 0.03	4.552 ± 0.046	38.92 ± 0.23	4.309 ± 0.077
475	47.42 ± 0.04	4.107 ± 0.042	45.42 ± 0.27	3.928 ± 0.069
500	46.80 ± 0.04	3.745 ± 0.038	44.67 ± 0.26	3.594 ± 0.063
525	1.898 ± 0.001	3.892 ± 0.055	1.898 ± 0.001	3.565 ± 0.062
550	0.9299 ± 0.0006	4.444 ± 0.065	0.9299 ± 0.0006	4.071 ± 0.072
600	2.471 ± 0.004	4.262 ± 0.052	2.471 ± 0.004	3.904 ± 0.061
700	13.16 ± 0.01	3.590 ± 0.038	13.16 ± 0.01	3.289 ± 0.047
800	0.991 ± 0.001	3.603 ± 0.053	0.991 ± 0.001	3.301 ± 0.058
Total	213.2 ± 0.1	4.469 ± 0.018	206.9 ± 1.1	4.216 ± 0.050
			Backscatter corrected	4.275 ± 0.050

Temp (°C)	Neon		
	^{20}Ne ($\times 10^{-11} \text{ cm}^3\text{STP}$)	$^{20}\text{Ne}/^{22}\text{Ne}$	$^{21}\text{Ne}/^{20}\text{Ne}$ ($\times 10^{-3}$)
200	0.21 ± 0.01	83.4 ± 72.7	2.807 ± 0.459
300	1.55 ± 0.03	20.1 ± 3.4	2.637 ± 0.271
350	3.46 ± 0.03	15.7 ± 1.3	2.294 ± 0.166
400	11.74 ± 0.07	14.697 ± 0.363	2.544 ± 0.082
450	41.50 ± 0.12	14.051 ± 0.113	2.410 ± 0.039
475	43.71 ± 0.15	13.695 ± 0.103	2.407 ± 0.037
500	52.85 ± 0.14	13.454 ± 0.082	2.400 ± 0.035
525	44.52 ± 0.13	13.589 ± 0.086	2.305 ± 0.047
550	39.40 ± 0.13	13.569 ± 0.094	2.399 ± 0.034
600	78.26 ± 0.26	13.627 ± 0.054	2.372 ± 0.032
700	75.17 ± 0.17	13.385 ± 0.050	2.428 ± 0.038
800	3.90 ± 0.04	13.944 ± 0.793	2.256 ± 0.152
Total	396.3 ± 0.4	13.669 ± 0.032	2.394 ± 0.014

Temp (°C)	Measured Argon		^{40}Ar subtracted	
	$^{40}\text{Ar}/^{36}\text{Ar}$	$^{36}\text{Ar}/^{38}\text{Ar}$	^{36}Ar ($\times 10^{-13} \text{ cm}^3\text{STP}$)	$^{36}\text{Ar}/^{38}\text{Ar}$
200	286.7 ± 4.7	5.13 ± 0.13	0.23 ± 0.12	2.42 ± 1.14
300	275.9 ± 3.1	5.38 ± 0.16	0.55 ± 0.09	6.42 ± 3.29
350	278.6 ± 3.6	5.28 ± 0.13	0.49 ± 0.09	4.76 ± 1.82
400	266.2 ± 3.4	5.42 ± 0.15	0.81 ± 0.09	6.46 ± 2.10
450	197.2 ± 1.7	5.22 ± 0.11	4.24 ± 0.09	5.025 ± 0.313
475	147.3 ± 1.3	5.50 ± 0.09	8.44 ± 0.12	5.686 ± 0.192
500	63.4 ± 0.30	5.37 ± 0.05	27.86 ± 0.14	5.378 ± 0.070
525	37.5 ± 0.2	5.51 ± 0.06	51.72 ± 0.32	5.544 ± 0.065
550	29.4 ± 0.1	5.47 ± 0.04	67.69 ± 0.35	5.489 ± 0.050
600	11.2 ± 0.1	5.48 ± 0.03	205.7 ± 0.7	5.481 ± 0.032
700	152.3 ± 0.3	5.32 ± 0.01	320.7 ± 0.8	5.317 ± 0.033
800	269.6 ± 0.8	5.23 ± 0.03	10.86 ± 0.32	4.457 ± 0.240
Total	127.4 ± 0.2	5.357 ± 0.011	688.4 ± 1.3	5.403 ± 0.021

8. PNE – unbaked PAC, 4.5 mm²

Temp (°C)	Helium – uncorrected		Corrected	
	⁴ He (× 10 ⁻⁸ cm ³ STP)	³ He/ ⁴ He (× 10 ⁻⁴)	⁴ He (× 10 ⁻⁸ cm ³ STP)	³ He/ ⁴ He (× 10 ⁻⁴)
200	0.704 ± 0.001	6.240 ± 0.090	0.704 ± 0.001	5.716 ± 0.100
300	10.832 ± 0.008	5.804 ± 0.060	10.832 ± 0.008	5.317 ± 0.076
350	11.081 ± 0.007	5.397 ± 0.056	11.081 ± 0.007	4.944 ± 0.071
400	13.43 ± 0.01	5.100 ± 0.052	13.43 ± 0.01	4.672 ± 0.066
450	24.03 ± 0.01	4.588 ± 0.047	23.52 ± 0.13	4.294 ± 0.077
475	23.19 ± 0.01	4.182 ± 0.044	22.68 ± 0.13	3.917 ± 0.071
500	28.57 ± 0.01	3.846 ± 0.039	27.62 ± 0.15	3.644 ± 0.065
525	2.963 ± 0.005	3.816 ± 0.044	2.963 ± 0.005	3.496 ± 0.053
550	0.668 ± 0.001	4.421 ± 0.065	0.668 ± 0.001	4.050 ± 0.072
600	1.641 ± 0.003	4.296 ± 0.057	1.641 ± 0.003	3.935 ± 0.065
650	5.262 ± 0.003	3.792 ± 0.042	5.262 ± 0.003	3.474 ± 0.052
700	3.997 ± 0.001	3.734 ± 0.043	3.997 ± 0.001	3.420 ± 0.052
750	0.6900 ± 0.0005	3.806 ± 0.077	0.6900 ± 0.0005	3.487 ± 0.078
800	0.4823 ± 0.0004	3.803 ± 0.069	0.4823 ± 0.0004	3.484 ± 0.072
Total	127.54 ± 0.03	4.495 ± 0.017	124.4 ± 0.7	4.189 ± 0.049
			Backscatter corrected	4.247 ± 0.049

Temp (°C)	Neon		
	²⁰ Ne (× 10 ⁻¹¹ cm ³ STP)	²⁰ Ne/ ²² Ne	²¹ Ne/ ²⁰ Ne (× 10 ⁻³)
200	0.23 ± 0.02	78 ± 60	4.241 ± 0.501
300	1.43 ± 0.03	18.97 ± 3.51	2.326 ± 0.181
350	2.82 ± 0.03	15.36 ± 1.60	2.578 ± 0.189
400	8.52 ± 0.05	14.64 ± 0.56	2.455 ± 0.117
450	25.68 ± 0.08	14.065 ± 0.181	2.382 ± 0.048
475	24.20 ± 0.10	13.730 ± 0.178	2.416 ± 0.057
500	34.74 ± 0.10	13.408 ± 0.126	2.391 ± 0.032
525	30.61 ± 0.18	13.496 ± 0.126	2.524 ± 0.068
550	16.96 ± 0.08	13.767 ± 0.221	2.540 ± 0.057
600	32.48 ± 0.14	13.613 ± 0.123	2.402 ± 0.045
650	47.95 ± 0.12	13.424 ± 0.082	2.429 ± 0.043
700	8.06 ± 0.05	12.906 ± 0.376	2.491 ± 0.115
750	2.21 ± 0.03	13.697 ± 1.374	2.982 ± 0.193
800	3.85 ± 0.05	13.220 ± 0.759	2.472 ± 0.147
Total	239.8 ± 0.3	13.654 ± 0.057	2.445 ± 0.018

Temp (°C)	Measured Argon		⁴⁰ Ar subtracted	
	⁴⁰ Ar/ ³⁶ Ar	³⁶ Ar/ ³⁸ Ar	³⁶ Ar (× 10 ⁻¹³ cm ³ STP)	³⁶ Ar/ ³⁸ Ar
200	283.7 ± 2.0	5.43 ± 0.08	0.88 ± 0.15	10.3 ± 6.9
300	285.0 ± 2.7	5.23 ± 0.10	0.64 ± 0.15	3.70 ± 1.39
350	286.3 ± 2.5	5.30 ± 0.10	0.55 ± 0.15	4.84 ± 2.48
400	281.5 ± 2.6	5.40 ± 0.12	0.79 ± 0.15	7.78 ± 5.05
450	246.3 ± 1.8	5.23 ± 0.08	3.53 ± 0.15	4.808 ± 0.409
475	208.3 ± 1.3	5.17 ± 0.08	6.45 ± 0.09	4.853 ± 0.253
500	110.0 ± 0.7	5.26 ± 0.06	22.96 ± 0.18	5.226 ± 0.094
525	53.7 ± 0.2	5.40 ± 0.05	54.71 ± 0.26	5.423 ± 0.060
550	90.9 ± 0.4	5.42 ± 0.06	28.25 ± 0.15	5.470 ± 0.083
600	49.2 ± 0.2	5.46 ± 0.03	84.18 ± 0.38	5.494 ± 0.042
650	46.5 ± 0.1	5.43 ± 0.02	185.44 ± 0.50	5.457 ± 0.029
700	256.4 ± 0.7	5.22 ± 0.03	19.93 ± 0.35	4.680 ± 0.201
750	266.6 ± 1.2	5.19 ± 0.05	6.27 ± 0.26	4.276 ± 0.324
800	251.0 ± 0.7	5.20 ± 0.03	15.76 ± 0.26	4.609 ± 0.160
Total	153.6 ± 0.2	5.328 ± 0.012	408.3 ± 0.9	5.390 ± 0.027

9. P7a – PAC baked 240 °C, 8.6 mm²

Temp (°C)	Helium – uncorrected		Corrected	
	⁴ He (× 10 ⁻⁸ cm ³ STP)	³ He/ ⁴ He (× 10 ⁻⁴)	⁴ He (× 10 ⁻⁸ cm ³ STP)	³ He/ ⁴ He (× 10 ⁻⁴)
200	0.4026 ± 0.0002	4.737 ± 0.097	0.4026 ± 0.0002	4.339 ± 0.098
300	1.754 ± 0.001	4.294 ± 0.057	1.754 ± 0.001	3.934 ± 0.065
350	4.593 ± 0.002	4.619 ± 0.051	4.593 ± 0.002	4.231 ± 0.063
400	15.87 ± 0.01	4.628 ± 0.048	15.76 ± 0.01	4.270 ± 0.077
450	39.77 ± 0.05	4.239 ± 0.043	38.40 ± 0.25	4.022 ± 0.072
475	60.40 ± 0.22	3.703 ± 0.037	56.91 ± 0.51	3.600 ± 0.063
500	11.06 ± 0.01	3.460 ± 0.036	11.06 ± 0.01	3.170 ± 0.046
525	2.805 ± 0.002	3.598 ± 0.042	2.805 ± 0.002	3.296 ± 0.050
550	1.355 ± 0.001	4.155 ± 0.060	1.355 ± 0.001	3.806 ± 0.067
600	2.068 ± 0.001	4.013 ± 0.049	2.068 ± 0.001	3.676 ± 0.058
650	4.880 ± 0.002	3.660 ± 0.042	4.880 ± 0.002	3.352 ± 0.051
700	4.065 ± 0.002	3.718 ± 0.044	4.065 ± 0.002	3.405 ± 0.052
750	0.7394 ± 0.0005	3.965 ± 0.073	0.7394 ± 0.0005	3.632 ± 0.075
800	0.5497 ± 0.0004	3.833 ± 0.062	0.5497 ± 0.0004	3.511 ± 0.067
Total	150.3 ± 0.2	3.969 ± 0.020	145.3 ± 1.0	3.760 ± 0.049
			Backscatter corrected	3.812 ± 0.049

Neon			
Temp (°C)	^{20}Ne ($\times 10^{-11} \text{ cm}^3 \text{ STP}$)	$^{20}\text{Ne}/^{22}\text{Ne}$	$^{21}\text{Ne}/^{20}\text{Ne}$ ($\times 10^{-3}$)
200	0.89 ± 0.02	17.94 ± 3.77	2.818 ± 0.368
300	1.37 ± 0.02	17.18 ± 2.21	2.657 ± 0.188
350	1.87 ± 0.02	14.11 ± 1.20	2.585 ± 0.153
400	6.36 ± 0.03	14.166 ± 0.468	2.351 ± 0.116
450	30.61 ± 0.05	13.895 ± 0.122	2.372 ± 0.047
475	44.29 ± 0.07	13.408 ± 0.081	2.435 ± 0.036
500	40.04 ± 0.06	13.386 ± 0.087	2.360 ± 0.041
525	51.49 ± 0.13	13.660 ± 0.073	2.400 ± 0.032
550	87.03 ± 0.09	13.700 ± 0.050	2.370 ± 0.026
600	52.28 ± 0.07	13.622 ± 0.064	2.366 ± 0.041
650	11.75 ± 0.06	12.971 ± 0.205	2.528 ± 0.073
700	8.72 ± 0.05	12.551 ± 0.261	2.486 ± 0.091
750	3.00 ± 0.03	13.118 ± 0.716	2.748 ± 0.133
800	3.34 ± 0.04	13.018 ± 0.651	2.829 ± 0.137
Total	343.0 ± 0.2	13.584 ± 0.033	2.401 ± 0.014

Temp (°C)	Measured Argon		^{40}Ar subtracted	
	$^{40}\text{Ar}/^{36}\text{Ar}$	$^{36}\text{Ar}/^{38}\text{Ar}$	^{36}Ar ($\times 10^{-13}$ $\text{ cm}^3 \text{ STP}$)	$^{36}\text{Ar}/^{38}\text{Ar}$
200	263.5 ± 2.5	5.31 ± 0.09	1.59 ± 0.13	5.23 ± 0.83
300	271.2 ± 2.8	5.34 ± 0.10	1.02 ± 0.10	5.63 ± 1.29
350	278.5 ± 4.6	5.28 ± 0.14	0.50 ± 0.13	4.69 ± 1.86
400	266.8 ± 3.2	5.47 ± 0.14	0.81 ± 0.08	7.43 ± 2.58
450	189.0 ± 2.2	5.41 ± 0.09	4.72 ± 0.10	5.566 ± 0.277
475	104.2 ± 0.7	5.44 ± 0.07	17.43 ± 0.13	5.509 ± 0.117
500	61.2 ± 0.3	5.52 ± 0.06	31.58 ± 0.18	5.571 ± 0.077
525	31.0 ± 0.1	5.52 ± 0.04	94.38 ± 0.34	5.547 ± 0.040
550	9.7 ± 0.0	5.56 ± 0.02	249.8 ± 0.8	5.567 ± 0.021
600	15.1 ± 0.0	5.53 ± 0.03	156.1 ± 0.6	5.538 ± 0.033
650	239.8 ± 0.7	5.28 ± 0.03	27.90 ± 0.34	5.133 ± 0.147
700	269.5 ± 0.5	5.27 ± 0.02	21.43 ± 0.44	4.817 ± 0.229
750	269.2 ± 1.0	5.26 ± 0.04	6.94 ± 0.26	4.728 ± 0.410
800	245.0 ± 1.1	5.26 ± 0.04	10.88 ± 0.23	4.986 ± 0.239
Total	138.7 ± 0.2	5.406 ± 0.010	607.3 ± 1.3	5.504 ± 0.021

10. P7b - PAC baked 240 °C, 9.4 mm²

Temp (°C)	Helium – uncorrected		Corrected	
	⁴ He (× 10 ⁻⁸ cm ³ STP)	³ He/ ⁴ He (× 10 ⁻⁴)	⁴ He (× 10 ⁻⁸ cm ³ STP)	³ He/ ⁴ He (× 10 ⁻⁴)
200	0.1543 ± 0.0002	5.487 ± 0.151	0.1543 ± 0.0002	5.026 ± 0.147
300	0.7029 ± 0.0006	4.786 ± 0.077	0.7029 ± 0.0006	4.384 ± 0.082
350	3.505 ± 0.002	4.737 ± 0.052	3.505 ± 0.002	4.339 ± 0.064
400	16.36 ± 0.02	4.689 ± 0.048	16.26 ± 0.02	4.324 ± 0.078
450	42.64 ± 0.11	4.338 ± 0.044	41.15 ± 0.32	4.117 ± 0.073
475	56.30 ± 0.11	3.902 ± 0.039	53.46 ± 0.38	3.764 ± 0.066
500	15.26 ± 0.01	3.669 ± 0.038	15.18 ± 0.09	3.378 ± 0.062
525	2.835 ± 0.001	3.783 ± 0.045	2.835 ± 0.001	3.465 ± 0.053
550	3.435 ± 0.002	3.851 ± 0.045	3.435 ± 0.002	3.528 ± 0.054
600	8.619 ± 0.006	3.751 ± 0.040	8.619 ± 0.006	3.436 ± 0.050
700	31.30 ± 0.03	3.421 ± 0.035	30.00 ± 0.03	3.270 ± 0.058
800	0.6429 ± 0.0004	3.748 ± 0.055	0.6429 ± 0.0004	3.433 ± 0.061
Total	181.8 ± 0.2	3.983 ± 0.018	175.9 ± 1.0	3.769 ± 0.047
Backscatter corrected				3.821 ± 0.047

Temp (°C)	Neon		
	²⁰ Ne (× 10 ⁻¹¹ cm ³ STP)	²⁰ Ne/ ²² Ne	²¹ Ne/ ²⁰ Ne (× 10 ⁻³)
200	0.37 ± 0.01	16.6 ± 6.1	3.037 ± 0.391
300	0.59 ± 0.02	15.8 ± 4.0	3.363 ± 0.355
350	1.04 ± 0.02	16.6 ± 2.8	2.784 ± 0.252
400	4.51 ± 0.03	14.40 ± 0.69	2.443 ± 0.146
450	27.26 ± 0.10	13.98 ± 0.14	2.362 ± 0.051
475	43.28 ± 0.12	13.54 ± 0.09	2.447 ± 0.040
500	36.73 ± 0.12	13.51 ± 0.09	2.415 ± 0.035
525	35.85 ± 0.11	13.59 ± 0.10	2.383 ± 0.054
550	73.18 ± 0.19	13.810 ± 0.064	2.328 ± 0.043
600	105.1 ± 0.2	13.698 ± 0.045	2.368 ± 0.027
700	64.30 ± 0.17	12.968 ± 0.063	2.437 ± 0.028
800	5.27 ± 0.04	13.042 ± 0.455	2.775 ± 0.143
Total	397.5 ± 0.4	13.578 ± 0.029	2.395 ± 0.014

Temp (°C)	Measured Argon		⁴⁰ Ar subtracted	
	⁴⁰ Ar/ ³⁶ Ar	³⁶ Ar/ ³⁸ Ar	³⁶ Ar (× 10 ⁻¹³ cm ³ STP)	³⁶ Ar/ ³⁸ Ar
200	283.8 ± 3.4	5.23 ± 0.09	0.55 ± 0.14	3.70 ± 1.18
300	283.8 ± 3.2	5.21 ± 0.11	0.47 ± 0.11	3.58 ± 1.34
350	283.2 ± 3.1	5.21 ± 0.12	0.44 ± 0.11	3.62 ± 1.33
400	284.2 ± 3.5	5.07 ± 0.11	0.38 ± 0.11	2.402 ± 0.725
450	226.1 ± 2.9	5.33 ± 0.13	2.82 ± 0.14	5.355 ± 0.540
475	166.4 ± 1.3	5.31 ± 0.08	10.66 ± 0.14	5.291 ± 0.173
500	99.3 ± 0.4	5.48 ± 0.06	17.84 ± 0.08	5.569 ± 0.087
525	52.4 ± 0.2	5.58 ± 0.05	42.69 ± 0.19	5.639 ± 0.068
550	18.08 ± 0.05	5.57 ± 0.03	172.6 ± 0.5	5.582 ± 0.030
600	10.76 ± 0.01	5.56 ± 0.02	324.0 ± 0.6	5.566 ± 0.021
700	217.9 ± 0.3	5.27 ± 0.02	147.9 ± 0.6	5.129 ± 0.067
800	250.8 ± 1.0	5.23 ± 0.03	14.28 ± 0.33	4.810 ± 0.196
Total	132.9 ± 0.2	5.391 ± 0.010	720.3 ± 1.2	5.464 ± 0.021

11. P04 – PAC baked 320 °C, 24.6 mm²

Temp (°C)	Helium – uncorrected		Corrected	
	⁴ He (× 10 ⁻⁸ cm ³ STP)	³ He/ ⁴ He (× 10 ⁻⁴)	⁴ He (× 10 ⁻⁸ cm ³ STP)	³ He/ ⁴ He (× 10 ⁻⁴)
200	0.0305 ± 0.0001	8.111 ± 0.337	0.0305 ± 0.0001	7.430 ± 0.317
300	0.0855 ± 0.0002	5.736 ± 0.152	0.0855 ± 0.0002	5.254 ± 0.149
350	0.3543 ± 0.0002	4.765 ± 0.104	0.3543 ± 0.0002	4.364 ± 0.104
400	8.038 ± 0.003	4.369 ± 0.048	8.038 ± 0.003	4.002 ± 0.059
450	81.53 ± 0.28	4.090 ± 0.041	<i>76.38 ± 0.66</i>	<i>3.999 ± 0.070</i>
475	105.86 ± 0.39	3.789 ± 0.038	<i>97.54 ± 0.87</i>	<i>3.766 ± 0.065</i>
500	55.22 ± 0.17	3.633 ± 0.037	<i>52.26 ± 0.43</i>	<i>3.516 ± 0.062</i>
525	5.335 ± 0.001	3.868 ± 0.042	5.335 ± 0.001	3.543 ± 0.052
550	2.877 ± 0.001	4.243 ± 0.049	2.877 ± 0.001	3.887 ± 0.059
600	5.824 ± 0.001	4.292 ± 0.046	5.824 ± 0.001	3.932 ± 0.057
700	27.26 ± 0.02	3.688 ± 0.038	<i>26.36 ± 0.02</i>	<i>3.494 ± 0.049</i>
800	1.433 ± 0.001	3.842 ± 0.044	1.433 ± 0.001	3.519 ± 0.053
Total	293.8 ± 0.5	3.868 ± 0.020	276.5 ± 1.9	3.765 ± 0.049
			Backscatter corrected	3.817 ± 0.049

Neon			
Temp (°C)	^{20}Ne ($\times 10^{-11} \text{ cm}^3\text{STP}$)	$^{20}\text{Ne}/^{22}\text{Ne}$	$^{21}\text{Ne}/^{20}\text{Ne} (\times 10^{-3})$
200	0.41 ± 0.02	16.3 ± 5.2	3.217 ± 0.454
300	0.51 ± 0.02	18.4 ± 5.6	2.460 ± 0.371
350	0.52 ± 0.02	19.3 ± 5.8	3.178 ± 0.474
400	2.07 ± 0.03	15.9 ± 1.5	2.783 ± 0.166
450	43.3 ± 0.1	13.68 ± 0.09	2.389 ± 0.041
475	76.6 ± 0.1	13.52 ± 0.06	2.430 ± 0.028
500	113.4 ± 0.1	13.45 ± 0.04	2.409 ± 0.023
525	132.0 ± 0.1	13.65 ± 0.04	2.376 ± 0.027
550	235.0 ± 0.2	13.64 ± 0.03	2.380 ± 0.019
600	217.9 ± 0.2	13.65 ± 0.03	2.394 ± 0.017
700	111.7 ± 0.1	13.19 ± 0.04	2.458 ± 0.032
800	10.0 ± 0.1	13.32 ± 0.26	2.557 ± 0.085
Total	943.5 ± 0.4	13.564 ± 0.016	2.403 ± 0.009

Temp (°C)	Measured Argon		^{40}Ar subtracted	
	$^{40}\text{Ar}/^{36}\text{Ar}$	$^{36}\text{Ar}/^{38}\text{Ar}$	^{36}Ar ($\times 10^{-13} \text{ cmSTP}$)	$^{36}\text{Ar}/^{38}\text{Ar}$
200	286.7 ± 2.1	5.39 ± 0.08	0.65 ± 0.16	9.3 ± 7.8
300	284.6 ± 3.1	5.38 ± 0.13	0.47 ± 0.13	7.7 ± 6.8
350	291.1 ± 3.1	5.24 ± 0.12	0.16 ± 0.10	2.76 ± 2.15
400	284.2 ± 3.0	5.22 ± 0.11	0.47 ± 0.13	3.64 ± 1.35
450	137.4 ± 1.0	5.34 ± 0.06	13.54 ± 0.13	5.352 ± 0.108
475	97.4 ± 0.4	5.34 ± 0.06	23.39 ± 0.13	5.345 ± 0.087
500	49.2 ± 0.1	5.49 ± 0.05	60.71 ± 0.21	5.522 ± 0.060
525	14.14 ± 0.04	5.45 ± 0.03	182.71 ± 0.62	5.456 ± 0.030
550	4.28 ± 0.01	5.51 ± 0.01	581.7 ± 1.5	5.516 ± 0.015
600	5.88 ± 0.01	5.51 ± 0.02	618.0 ± 1.4	5.510 ± 0.018
700	225.4 ± 0.2	5.24 ± 0.01	305.5 ± 1.2	4.982 ± 0.057
800	265.1 ± 0.5	5.26 ± 0.02	27.47 ± 0.44	4.802 ± 0.190
Total	125.1 ± 0.2	5.363 ± 0.007	1787.3 ± 2.5	5.405 ± 0.015

For the following three samples, all of the gas was extracted in one high-temperature step of 850 °C. The He and Ne gas was then repeatedly divided into smaller and smaller fractions in order to determine the effects of high-pressure on the measured data.

12. P16 – unbaked PAC (full melt), 9.7 mm²

Fraction	Helium – uncorrected		Corrected	
	⁴ He (× 10 ⁻⁸ cm ³ STP)	³ He/ ⁴ He (× 10 ⁻⁴)	⁴ He (× 10 ⁻⁸ cm ³ STP)	³ He/ ⁴ He (× 10 ⁻⁴)
Small portion admitted	52.89 ± 0.13	4.306 ± 0.008	<i>50.55 ± 0.13</i>	<i>4.127 ± 0.049</i>
All gas admitted	227.2 ± 0.3	4.247 ± 0.043	211.7 ± 0.3	4.175 ± 0.059
			Backscatter corrected	4.224 ± 0.059
Split 1	99.50 ± 0.27	4.243 ± 0.009	<i>92.66 ± 0.27</i>	<i>4.173 ± 0.050</i>
Split 2	41.49 ± 0.15	4.396 ± 0.010	<i>40.07 ± 0.15</i>	<i>4.170 ± 0.051</i>
Split 3	17.59 ± 0.02	4.500 ± 0.026	<i>17.40 ± 0.11</i>	<i>4.166 ± 0.060</i>
Split 4	7.534 ± 0.004	4.571 ± 0.032	7.534 ± 0.004	4.187 ± 0.065

Fraction	Neon		
	²⁰ Ne (× 10 ⁻¹¹ cm ³ STP)	²⁰ Ne/ ²² Ne	²¹ Ne/ ²⁰ Ne (× 10 ⁻³)
Small portion admitted	157.3 ± 0.4	13.580 ± 0.060	2.357 ± 0.030
All gas admitted	403.0 ± 0.4	13.653 ± 0.033	2.360 ± 0.015
Split 1	186.6 ± 0.2	13.675 ± 0.056	2.380 ± 0.029
Split 2	84.23 ± 0.14	13.597 ± 0.065	2.372 ± 0.042
Split 3	38.04 ± 0.07	13.646 ± 0.089	2.540 ± 0.065
Split 4	17.15 ± 0.06	13.560 ± 0.166	2.555 ± 0.098

Fraction	Measured Argon		⁴⁰ Ar subtracted	
	⁴⁰ Ar/ ³⁶ Ar	³⁶ Ar/ ³⁸ Ar	³⁶ Ar (× 10 ⁻¹³ cm ³ STP)	³⁶ Ar/ ³⁸ Ar
All gas admitted	106.3 ± 0.1	5.376 ± 0.010	774.7 ± 0.9	5.408 ± 0.018

13. P8b – PAC baked 240 °C (full melt), 7.4 mm²

Fraction	Helium – uncorrected		Corrected	
	⁴ He (× 10 ⁻⁸ cm ³ STP)	³ He/ ⁴ He (× 10 ⁻⁴)	⁴ He (× 10 ⁻⁸ cm ³ STP)	³ He/ ⁴ He (× 10 ⁻⁴)
Small portion admitted	31.50 ± 0.04	4.122 ± 0.018	30.37 ± 0.04	3.916 ± 0.053
All gas admitted	139.9 ± 0.5	3.891 ± 0.040	127.6 ± 1.1	3.907 ± 0.067
			Backscatter corrected	3.961 ± 0.067
Split 1	58.28 ± 0.16	4.045 ± 0.006	55.31 ± 0.16	3.904 ± 0.046
Split 2	24.23 ± 0.03	4.154 ± 0.018	23.62 ± 0.03	3.902 ± 0.053
Split 3	10.37 ± 0.01	4.272 ± 0.018	10.37 ± 0.01	3.913 ± 0.053

Fraction	Neon		
	²⁰ Ne (× 10 ⁻¹¹ cm ³ STP)	²⁰ Ne/ ²² Ne	²¹ Ne/ ²⁰ Ne (× 10 ⁻³)
Small portion admitted	120.9 ± 0.3	13.659 ± 0.053	2.385 ± 0.026
All gas admitted	307.2 ± 0.6	13.580 ± 0.039	2.385 ± 0.019
Split 1	140.2 ± 0.2	13.619 ± 0.050	2.352 ± 0.039
Split 2	62.92 ± 0.32	13.582 ± 0.088	2.434 ± 0.072
Split 3	28.26 ± 0.08	13.467 ± 0.125	2.508 ± 0.078

Fraction	Measured Argon		⁴⁰ Ar subtracted	
	⁴⁰ Ar/ ³⁶ Ar	³⁶ Ar/ ³⁸ Ar	³⁶ Ar (× 10 ⁻¹³ cm ³ STP)	³⁶ Ar/ ³⁸ Ar
All gas admitted	112.2 ± 0.2	5.392 ± 0.014	586.6 ± 1.0	5.437 ± 0.024

14. P02 – PAC baked 360 °C (full melt), 15.4 mm²

Fraction	Helium – uncorrected		Corrected	
	⁴ He (× 10 ⁻⁸ cm ³ STP)	³ He/ ⁴ He (× 10 ⁻⁴)	⁴ He (× 10 ⁻⁸ cm ³ STP)	³ He/ ⁴ He (× 10 ⁻⁴)
Small portion admitted	13.99 ± 0.02	3.724 ± 0.014	13.79 ± 0.02	3.461 ± 0.045
All gas admitted	49.37 ± 0.34	3.617 ± 0.037	47.00 ± 0.57	3.480 ± 0.069
			Backscatter corrected	3.528 ± 0.069
Split 1	21.53 ± 0.01	3.714 ± 0.015	21.08 ± 0.01	3.475 ± 0.046
Split 2	9.135 ± 0.004	3.831 ± 0.029	9.135 ± 0.004	3.509 ± 0.056
Split 3	4.005 ± 0.004	3.812 ± 0.043	4.005 ± 0.024	3.492 ± 0.066

Fraction	Neon		
	²⁰ Ne (× 10 ⁻¹¹ cm ³ STP)	²⁰ Ne/ ²² Ne	²¹ Ne/ ²⁰ Ne (× 10 ⁻³)
Small portion admitted	214.2 ± 0.3	13.512 ± 0.051	2.445 ± 0.030
All gas admitted	499.9 ± 1.8	13.498 ± 0.036	2.386 ± 0.014
Split 1	232.9 ± 0.2	13.569 ± 0.045	2.407 ± 0.021
Split 2	104.6 ± 0.1	13.455 ± 0.063	2.426 ± 0.077
Split 3	47.08 ± 0.12	13.414 ± 0.094	2.442 ± 0.059

Fraction	Measured Argon		⁴⁰ Ar subtracted	
	⁴⁰ Ar/ ³⁶ Ar	³⁶ Ar/ ³⁸ Ar	³⁶ Ar (× 10 ⁻¹³ cm ³ STP)	³⁶ Ar/ ³⁸ Ar
All gas admitted	118.8 ± 0.1	5.356 ± 0.007	1189.9 ± 1.3	5.381 ± 0.015

Only interference corrections are applied to the step-wise heating blank data in the following tables. Crossed-out values had too little gas to measure accurately or negative values.

Step-wise heating blank

Temp (°C)	Helium	
	⁴ He (× 10 ⁻¹⁰ cm ³ STP)	³ He/ ⁴ He (× 10 ⁻⁴)
200	0.43 ± 0.01	23.1 ± 1.7
300	0.91 ± 0.01	13.1 ± 1.0
350	0.65 ± 0.01	16.7 ± 0.9
450	2.11 ± 0.01	7.76 ± 0.50
475	1.51 ± 0.01	8.07 ± 0.62
500	1.84 ± 0.01	8.44 ± 0.56
525	1.81 ± 0.01	7.29 ± 0.41
550	2.00 ± 0.01	14.0 ± 0.6
600	3.54 ± 0.01	6.15 ± 0.30
700	11.97 ± 0.03	4.62 ± 0.19
800	36.12 ± 0.03	4.05 ± 0.08
Total	62.90 ± 0.05	5.43 ± 0.07

Temp (°C)	Neon		
	²⁰ Ne (× 10 ⁻¹¹ cm ³ STP)	²⁰ Ne/ ²² Ne	²¹ Ne/ ²⁰ Ne (× 10 ⁻³)
200	0.032 ± 0.011	25.2 ± 33.8	43 ± 13
300	0.003 ± 0.011	21.4 ± 33.4	-5 ± 22
350	-0.008 ± 0.010	26.3 ± 35.9	59 ± 14
450	0.014 ± 0.009	26.1 ± 48.2	50 ± 12
475	-0.008 ± 0.010	25.0 ± 41.1	-41 ± 23
500	0.006 ± 0.009	17.3 ± 21.7	10 ± 12
525	0.013 ± 0.007	20.2 ± 27.3	25 ± 11
550	0.030 ± 0.010	39.2 ± 51.4	19 ± 8
600	0.084 ± 0.010	20.7 ± 18.1	46 ± 12
700	0.909 ± 0.023	15.1 ± 2.9	27 ± 3
800	3.091 ± 0.028	14.1 ± 0.8	28 ± 2
Total	4.181 ± 0.043	14.5 ± 1.0	28 ± 2

Temp (°C)	Measured Argon		⁴⁰ Ar subtracted	
	⁴⁰ Ar/ ³⁶ Ar	³⁶ Ar/ ³⁸ Ar	³⁶ Ar (× 10 ⁻¹³ cm ³ STP)	³⁶ Ar/ ³⁸ Ar
200	286.7 ± 3.3	5.33 ± 0.10	0.39 ± 0.13	5.7 ± 3.7
300	292.3 ± 3.4	5.44 ± 0.14	0.13 ± 0.13	7.8 ± 28.5
350	296.5 ± 4.2	5.57 ± 0.17	0.03 ± 0.13	0.2 ± **
450	294.2 ± 4.1	5.44 ± 0.13	0.08 ± 0.16	2.2 ± **
475	289.1 ± 3.6	5.41 ± 0.10	0.26 ± 0.13	19.2 ± 62.4
500	299.6 ± 3.8	5.40 ± 0.12	0.10 ± 0.10	2.4 ± 2.5
525	294.9 ± 2.8	5.31 ± 0.13	0.05 ± 0.10	3.4 ± **
550	294.6 ± 3.2	5.27 ± 0.12	0.05 ± 0.10	1.7 ± **
600	287.9 ± 2.2	5.27 ± 0.11	0.39 ± 0.10	4.0 ± 2.4
700	289.0 ± 0.9	5.19 ± 0.04	2.13 ± 0.26	2.6 ± 0.5
800	250.6 ± 1.1	5.24 ± 0.04	13.8 ± 0.3	4.8 ± 0.2
Total	277.7 ± 0.6	5.27 ± 0.02	17.2 ± 0.5	4.6 ± 1.2

Appendix B: Step-wise heating diffusion coefficients

Diffusion coefficients calculated from step-wise heating data assuming a uniform gas distribution in the sample.

1. A70 – unbaked AloS

Temp (°C)	$^4\text{He} - D/\ell^2 (\text{s}^{-1})$	$^{20}\text{Ne} - D/\ell^2 (\text{s}^{-1})$	$^{36}\text{Ar} - D/\ell^2 (\text{s}^{-1})$
200	2.8×10^{-9}	2.6×10^{-10}	8.2×10^{-11}
300	2.7×10^{-7}	1.6×10^{-9}	4.0×10^{-10}
350	9.2×10^{-7}	3.1×10^{-9}	6.9×10^{-10}
400	1.8×10^{-6}	8.8×10^{-9}	1.0×10^{-9}
450	2.5×10^{-6}	2.9×10^{-8}	2.0×10^{-9}
475	2.3×10^{-6}	3.9×10^{-8}	2.6×10^{-9}
500	2.8×10^{-6}	7.5×10^{-8}	5.6×10^{-9}
525	3.4×10^{-6}	2.0×10^{-7}	1.3×10^{-8}
550	2.7×10^{-6}	5.1×10^{-7}	1.9×10^{-8}
600	8.3×10^{-6}	7.5×10^{-6}	1.7×10^{-7}
650	1.2×10^{-4}	9.7×10^{-5}	9.6×10^{-5}
700	3.5×10^{-5}	3.8×10^{-5}	4.6×10^{-5}
750	1.3×10^{-5}	1.1×10^{-5}	1.4×10^{-5}
800	2.6×10^{-5}	2.2×10^{-5}	2.3×10^{-5}

2. A63 – unbaked AloS

Temp (°C)	$^4\text{He} - D/\ell^2 (\text{s}^{-1})$	$^{20}\text{Ne} - D/\ell^2 (\text{s}^{-1})$	$^{36}\text{Ar} - D/\ell^2 (\text{s}^{-1})$
200	1.2×10^{-10}	6.8×10^{-11}	1.7×10^{-11}
300	1.4×10^{-8}	1.9×10^{-9}	2.5×10^{-10}
350	1.9×10^{-8}	5.1×10^{-9}	4.4×10^{-10}
400	4.8×10^{-8}	1.8×10^{-8}	1.1×10^{-9}
450	3.5×10^{-7}	5.5×10^{-8}	1.9×10^{-9}
475	1.3×10^{-6}	8.2×10^{-8}	3.2×10^{-9}
500	2.6×10^{-6}	1.4×10^{-7}	4.3×10^{-9}
525	4.2×10^{-6}	3.9×10^{-7}	8.7×10^{-9}
550	5.4×10^{-6}	1.2×10^{-6}	1.8×10^{-8}
600	7.9×10^{-5}	1.8×10^{-5}	5.6×10^{-6}
700	1.1×10^{-4}	9.6×10^{-5}	1.0×10^{-4}

3. A67 – 240

Temp (°C)	$^4\text{He} - \text{D}/\ell^2 (\text{s}^{-1})$	$^{20}\text{Ne} - \text{D}/\ell^2 (\text{s}^{-1})$	$^{36}\text{Ar} - \text{D}/\ell^2 (\text{s}^{-1})$
200	4.5×10^{-12}	1.5×10^{-11}	2.0×10^{-11}
300	1.8×10^{-10}	9.5×10^{-11}	3.0×10^{-11}
350	9.5×10^{-10}	2.5×10^{-10}	4.3×10^{-11}
400	1.2×10^{-8}	2.3×10^{-9}	8.1×10^{-11}
450	4.0×10^{-7}	1.6×10^{-8}	5.2×10^{-10}
475	1.5×10^{-6}	4.4×10^{-8}	1.6×10^{-9}
500	2.9×10^{-6}	1.5×10^{-7}	3.9×10^{-9}
525	3.8×10^{-6}	5.8×10^{-7}	7.5×10^{-9}
550	3.4×10^{-6}	2.1×10^{-6}	1.4×10^{-8}
600	8.1×10^{-6}	1.2×10^{-5}	9.9×10^{-8}
700	2.2×10^{-4}	1.4×10^{-4}	1.3×10^{-4}

4. A66 – 280

Temp (°C)	$^4\text{He} - \text{D}/\ell^2 (\text{s}^{-1})$	$^{20}\text{Ne} - \text{D}/\ell^2 (\text{s}^{-1})$	$^{36}\text{Ar} - \text{D}/\ell^2 (\text{s}^{-1})$
200	1.1×10^{-10}	6.2×10^{-12}	2.5×10^{-12}
300	2.0×10^{-9}	4.4×10^{-11}	4.1×10^{-12}
350	6.0×10^{-9}	1.3×10^{-10}	1.1×10^{-11}
400	3.9×10^{-8}	6.9×10^{-10}	2.0×10^{-11}
450	7.5×10^{-7}	5.4×10^{-9}	1.0×10^{-10}
475	2.0×10^{-6}	1.8×10^{-8}	4.5×10^{-10}
500	4.1×10^{-6}	1.1×10^{-7}	3.8×10^{-9}
525	8.8×10^{-6}	7.8×10^{-6}	1.8×10^{-7}
550	1.5×10^{-5}	1.1×10^{-5}	3.4×10^{-6}
600	9.2×10^{-5}	4.2×10^{-5}	4.6×10^{-5}
650	3.6×10^{-5}	3.0×10^{-5}	3.5×10^{-5}
700	2.8×10^{-5}	2.4×10^{-5}	2.0×10^{-5}
750	8.7×10^{-6}	9.0×10^{-6}	5.6×10^{-6}
800	1.8×10^{-5}	1.4×10^{-5}	1.1×10^{-5}

5. A68 – 320

Temp (°C)	⁴ He - D/ ℓ ² (s ⁻¹)	²⁰ Ne - D/ ℓ ² (s ⁻¹)	³⁶ Ar - D/ ℓ ² (s ⁻¹)
200	2.0×10 ⁻¹²	1.8×10 ⁻¹²	7.2×10 ⁻¹²
300	5.6×10 ⁻¹¹	1.4×10 ⁻¹¹	5.8×10 ⁻¹¹
350	6.4×10 ⁻¹⁰	2.8×10 ⁻¹¹	6.4×10 ⁻¹²
400	7.5×10 ⁻⁹	1.6×10 ⁻¹⁰	6.2×10 ⁻¹¹
450	1.2×10 ⁻⁷	1.5×10 ⁻⁹	2.5×10 ⁻¹⁰
475	4.4×10 ⁻⁷	5.2×10 ⁻⁹	4.9×10 ⁻¹⁰
500	9.3×10 ⁻⁷	1.9×10 ⁻⁸	1.3×10 ⁻⁹
525	1.8×10 ⁻⁶	8.6×10 ⁻⁸	5.8×10 ⁻⁹
550	2.1×10 ⁻⁶	5.0×10 ⁻⁷	2.1×10 ⁻⁸
600	7.5×10 ⁻⁶	1.2×10 ⁻⁵	1.1×10 ⁻⁶
650	1.2×10 ⁻⁴	9.1×10 ⁻⁵	9.5×10 ⁻⁵
700	5.4×10 ⁻⁵	5.2×10 ⁻⁵	4.7×10 ⁻⁵
750	3.3×10 ⁻⁵	2.9×10 ⁻⁵	2.7×10 ⁻⁵

6. A71 – 360

Temp (°C)	⁴ He - D/ ℓ ² (s ⁻¹)	²⁰ Ne - D/ ℓ ² (s ⁻¹)	³⁶ Ar - D/ ℓ ² (s ⁻¹)
200	7.3×10 ⁻¹²	1.1×10 ⁻¹¹	1.9×10 ⁻¹¹
300	8.0×10 ⁻¹¹	3.4×10 ⁻¹¹	3.8×10 ⁻¹¹
350	5.5×10 ⁻¹⁰	7.7×10 ⁻¹¹	9.7×10 ⁻¹¹
400	1.8×10 ⁻⁸	4.0×10 ⁻¹⁰	1.3×10 ⁻¹⁰
475	4.2×10 ⁻⁷	4.9×10 ⁻⁰⁹	5.4×10 ⁻¹⁰
500	8.3×10 ⁻⁷	1.9×10 ⁻⁰⁸	1.5×10 ⁻⁹
525	1.9×10 ⁻⁶	1.9×10 ⁻⁰⁷	9.3×10 ⁻⁹
550	4.5×10 ⁻⁶	2.3×10 ⁻⁰⁶	1.0×10 ⁻⁷
600	1.0×10 ⁻⁴	6.1×10 ⁻⁰⁵	5.6×10 ⁻⁵
650	3.2×10 ⁻⁵	3.0×10 ⁻⁰⁵	4.2×10 ⁻⁵
700	1.0×10 ⁻⁵	8.5×10 ⁻⁰⁶	1.0×10 ⁻⁵
750	1.4×10 ⁻⁵	6.7×10 ⁻⁰⁶	1.5×10 ⁻⁵

7. PSE – unbaked PAC

Temp (°C)	⁴ He - D/ ℓ ² (s ⁻¹)	²⁰ Ne - D/ ℓ ² (s ⁻¹)	³⁶ Ar - D/ ℓ ² (s ⁻¹)
200	1.1×10 ⁻⁹	1.9×10 ⁻¹¹	7.9×10 ⁻¹²
300	4.6×10 ⁻⁷	1.4×10 ⁻⁹	8.2×10 ⁻¹¹
350	1.5×10 ⁻⁶	1.1×10 ⁻⁸	1.5×10 ⁻¹⁰
400	3.7×10 ⁻⁶	1.2×10 ⁻⁷	4.0×10 ⁻¹⁰
450	1.0×10 ⁻⁵	1.4×10 ⁻⁶	5.3×10 ⁻⁹
475	2.0×10 ⁻⁵	3.3×10 ⁻⁶	2.6×10 ⁻⁸
500	4.6×10 ⁻⁵	6.3×10 ⁻⁶	2.4×10 ⁻⁷
525	3.9×10 ⁻⁶	7.3×10 ⁻⁶	1.1×10 ⁻⁶
550	2.0×10 ⁻⁶	8.4×10 ⁻⁶	2.6×10 ⁻⁶
600	6.0×10 ⁻⁶	2.6×10 ⁻⁵	1.6×10 ⁻⁵
700	1.0×10 ⁻⁴	1.1×10 ⁻⁴	1.3×10 ⁻⁴

8. PNE – unbaked PAC

Temp (°C)	⁴ He - D/ ℓ ² (s ⁻¹)	²⁰ Ne - D/ ℓ ² (s ⁻¹)	³⁶ Ar - D/ ℓ ² (s ⁻¹)
200	2.2×10 ⁻⁹	6.8×10 ⁻¹¹	3.0×10 ⁻¹⁰
300	5.9×10 ⁻⁷	3.4×10 ⁻⁹	6.0×10 ⁻¹⁰
350	1.7×10 ⁻⁶	2.2×10 ⁻⁸	7.8×10 ⁻¹⁰
400	3.5×10 ⁻⁶	1.9×10 ⁻⁷	1.5×10 ⁻⁹
450	1.0×10 ⁻⁵	1.7×10 ⁻⁶	1.3×10 ⁻⁸
475	1.6×10 ⁻⁵	3.1×10 ⁻⁶	4.9×10 ⁻⁸
500	3.9×10 ⁻⁵	7.1×10 ⁻⁶	4.4×10 ⁻⁷
525	7.8×10 ⁻⁶	8.7×10 ⁻⁶	2.7×10 ⁻⁶
550	2.0×10 ⁻⁶	6.2×10 ⁻⁶	2.3×10 ⁻⁶
600	5.5×10 ⁻⁶	1.6×10 ⁻⁵	1.1×10 ⁻⁵
650	2.6×10 ⁻⁵	5.6×10 ⁻⁵	6.3×10 ⁻⁵
700	5.6×10 ⁻⁵	3.2×10 ⁻⁵	2.4×10 ⁻⁵
750	3.3×10 ⁻⁵	1.7×10 ⁻⁵	1.3×10 ⁻⁵

9. P7a – 240 PAC

Temp (°C)	$^4\text{He} - \text{D}/\ell^2 (\text{s}^{-1})$	$^{20}\text{Ne} - \text{D}/\ell^2 (\text{s}^{-1})$	$^{36}\text{Ar} - \text{D}/\ell^2 (\text{s}^{-1})$
200	5.6×10^{-10}	4.9×10^{-10}	4.7×10^{-10}
300	1.5×10^{-8}	2.7×10^{-9}	8.0×10^{-10}
350	1.4×10^{-7}	7.4×10^{-9}	5.3×10^{-10}
400	1.6×10^{-6}	5.8×10^{-8}	1.1×10^{-9}
450	1.1×10^{-5}	9.8×10^{-7}	1.1×10^{-8}
475	4.2×10^{-5}	3.5×10^{-6}	1.1×10^{-7}
500	1.9×10^{-5}	5.2×10^{-6}	4.9×10^{-7}
525	7.0×10^{-6}	9.6×10^{-6}	3.7×10^{-6}
550	3.9×10^{-6}	2.8×10^{-5}	2.8×10^{-5}
600	6.9×10^{-6}	4.1×10^{-5}	4.5×10^{-5}
650	2.4×10^{-5}	2.2×10^{-5}	2.0×10^{-5}
700	5.3×10^{-5}	3.2×10^{-5}	3.0×10^{-5}
750	3.2×10^{-5}	2.4×10^{-5}	1.9×10^{-5}

10. P7b – 240 PAC

Temp (°C)	$^4\text{He} - \text{D}/\ell^2 (\text{s}^{-1})$	$^{20}\text{Ne} - \text{D}/\ell^2 (\text{s}^{-1})$	$^{36}\text{Ar} - \text{D}/\ell^2 (\text{s}^{-1})$
200	5.6×10^{-11}	6.4×10^{-11}	4.0×10^{-11}
300	1.7×10^{-9}	3.7×10^{-10}	9.8×10^{-11}
350	4.3×10^{-8}	1.4×10^{-9}	1.5×10^{-10}
400	9.5×10^{-7}	1.8×10^{-8}	1.7×10^{-10}
450	8.0×10^{-6}	5.1×10^{-7}	2.5×10^{-9}
475	2.4×10^{-5}	2.2×10^{-6}	2.9×10^{-8}
500	1.1×10^{-5}	3.2×10^{-6}	1.2×10^{-7}
525	2.4×10^{-6}	4.3×10^{-6}	6.3×10^{-7}
550	3.1×10^{-6}	1.3×10^{-5}	7.5×10^{-6}
600	9.3×10^{-6}	3.5×10^{-5}	4.1×10^{-5}
700	1.5×10^{-4}	9.7×10^{-5}	9.1×10^{-5}

11. P04 – 320 PAC

Temp (°C)	${}^4\text{He} - \text{D}/\ell^2 (\text{s}^{-1})$	${}^{20}\text{Ne} - \text{D}/\ell^2 (\text{s}^{-1})$	${}^{36}\text{Ar} - \text{D}/\ell^2 (\text{s}^{-1})$
200	8.9×10^{-13}	1.4×10^{-11}	9.3×10^{-12}
300	1.2×10^{-11}	5.5×10^{-11}	1.8×10^{-11}
350	2.0×10^{-10}	1.0×10^{-10}	8.2×10^{-12}
400	6.9×10^{-8}	8.4×10^{-10}	3.1×10^{-11}
450	6.8×10^{-6}	1.8×10^{-7}	5.1×10^{-9}
475	2.7×10^{-5}	1.1×10^{-6}	2.8×10^{-8}
500	3.0×10^{-5}	3.3×10^{-6}	1.9×10^{-7}
525	5.1×10^{-6}	6.5×10^{-6}	1.5×10^{-6}
550	3.1×10^{-6}	2.0×10^{-5}	1.5×10^{-5}
600	7.1×10^{-6}	3.9×10^{-5}	3.9×10^{-5}
700	1.1×10^{-4}	9.4×10^{-5}	9.4×10^{-5}

Appendix C: Mathematica Files for Diffusion Calculations

Calculating the diffusion coefficient from fractional loss:

```
Clear[A,B,CC,l,DtI2,n]
l=3000;
A=8.250640146;
B=3.469694876*10^(-3);
CC=-3.70023042*10^(-6);
F = 5.7583013*10^(-10);
n ∈ Integers;
ICx=Exp[A+B*x+CC*x^2 +F*x^3];
DtI2=3.181*10^-4;
IC0=NIntegrate[ICx,{x,0,l}];
flossSum =
Sum[(4/((2*n+1)*Pi))*
Exp[-((2*n+1)*Pi)^2*DtI2]*NIntegrate[ICx*Sin[(2*n+1)*Pi*x/l],{x,0,l}],{n,0,10^3}];
flossX=1-flossSum/IC0
```

Profile Evolution:

```
Clear[A,B,CC,l,DtI2,n]
l=3000;
A=8.250640146;
B=3.469694876*10^(-3);
CC=-3.70023042*10^(-6);
F = 5.7583013*10^(-10);
n ∈ Integers;
DtI2=6.285*10^-3;
IC=Exp[A+B*xdummy+CC*xdummy^2+F*xdummy^3];
ICn[x_]:=Sum[(2/l)*Exp[-
(n*Pi)^2*DtI2]*Sin[(n)*Pi*x/l]*Re[NIntegrate[IC*Sin[(n)*Pi*xdummy/l],{xdummy,0,l}],{
n,0,500}]
IC3 = Quiet[Table[{x,Re[ICn[x]]},{x,0,3000,10}]];
Export["C:\\Users\\Argon\\Documents\\1 Work \\Sync\\Diffusion\\Diffusion
Calcs\\June2009\\4He AloS\\TRIM fits\\4He \\AloS bin profiles.xls", IC3]
```

Appendix D: LabVIEW Laser Rastering Program

